# A Measurement of the Rate of Formation of Pi-Mu Atoms in $K_L^0$ Decay

by

David Hedin

A thesis submitted in partial fulfillment of the requirements for the degree of

Doctor of Philosophy
(Physics)

at the

University of Wisconsin-Madison

1980

## Acknowledgment

I first would like to thank Sam Aronson for his support and direction over the course of the last four and one half years. I only regret the circumstances that limited his direct participation.

In doing the experiment which this paper describes, there were many high points and low points. Overall though, it was a truly enjoyable and satisfying experience. Part of this was due to my colleagues from Chicago, Stanford and Wisconsin with whom I had the privilege of working. Mel Schwartz proposed that this experiment should be done. Bob Cousins and John Greenhalgh shared with me the major tasks and responsibilities of the experiment. Bob Bernstein, Greg Bock, Gordon Thomson and Bruce Winstein all contributed many midnight shifts and provided important insights. Tom Shea and Adrian Alexander provided their standard excellent technical support.

I would also like to thank the many other people who contributed to the large technical effort needed to mount an experiment of this size. The Physical Science Laboratory did a superb job in providing us a beam line at a reasonable cost. The overworked personnel in Fermilab's Meson department always seemed to squeeze in enough time to satisfy our needs.

I would also like to thank Ching Cheng-rui, Ho Tso-hsiu and Chang Chao-hsi for sending me early results of their calculations.

Bindu Bambah also helped in sorting out possible corrections to the theoretical calculation.

Finally, I would like to thank Don Reeder and the rest of the High Energy Group at Wisconsin for their continued support of this experiment.

# Table of Contents


| | Page |
|---|---|
| ACKNOWLEDGMENTS . . . . . | i |
| LIST OF TABLES . . . . . | vi |
| LIST OF ILLUSTRATIONS . . . . . | vii |
| ABSTRACT . . . . . | xii |
| Chapter | |
| I. INTRODUCTION. . . . . | 1 |
| II. THEORY. . . . . | 2 |
| III. EXPERIMENTAL TECHNIQUE . . . . . | 9 |
| IV. EXPERIMENTAL SETUP. . . . . | 13 |
| A. Beam and Decay Region | |
| B. Vacuum Window | |
| C. Spectrometer Magnets | |
| D. Ionizing Foil | |
| E. Counters and Trigger Logic | |
| F. Wire Chambers | |
| G. Data Acquisition System | |
| V. DATA COLLECTION. . . . . | 26 |
| A. Main Data | |
| B. Calibration Data Sets | |

Table of Contents (con.)

Page

Chapter

VI. MONTE CARLO CALCULATION . . . 29

A. $K_L^o$ Decays

B. Tracking through the Spectrometer

VII. REDUCTION OF DATA . . . . . 36

A. Track Definition

B. Particle Identification

C. Magnet Tuning

D. Event Selection

1. General Classes

2. Pi-Mu Atoms

3. $K_{\mu 3}$'s

4. Gamma Events

5. $K_{e3}$'s

VIII. $K_{\mu 3}$ Background . . . . . 80

IX. COMPARISON OF DATA TO MONTE CARLO 92

A. Single Muons

B. $K_{\mu 3}$'s

C. Monte Carlo Studies

Table of Contents (con.)

Page

Chapter

X. TRIGGER CORRECTIONS . . . . . 111

IX. RESULTS AND CONCLUSIONS. . . . 117

A. Determination of the Pi-Mu Atom Rate of Formation

B. Determination of $\xi$

C. Determination of the Pi-Mu Atom Lifetime

D. Conclusions

Appendix

A. $K_{\mu\beta}$ FORM FACTORS . . . . . 125

B. IONIZATION OF PI-MU ATOMS . . . 127

C. CHAMBER AND COUNTER EFFICIENCY MEASUREMENTS . . . . . 129

D. APPARATUS LOCATION MEASUREMENTS . 134

REFERENCES . . . . . 137

## List of Tables


| Table | | Page |
|---|---|---|
| 1. | Properties of Pi-Mu Atoms . . . . . | 3 |
| 2. | Properties of the Fermilab M3 Neutral Beam | 16 |
| 3. | Chamber Efficiencies. . . . . | 40 |
| 4. | Comparison of $K_{\mu 3}$ Topology Classes . . . | 42 |
| 5. | Shower Counter Requirements . . . . . | 47 |
| 6. | Requirements for General Classes. . . . | 57 |
| 7. | $K_{\mu 3}$ Non-Beam Background Classes . . . . | 82 |
| 8. | Sources of $K_{\mu 3}$ Background . . . . . | 91 |
| 9. | Chamber Resolution Fit Results . . . . | 94 |
| 10. | Single Muon H and W Counter Bank Distributions. . . . . | 112 |
| 11. | Sources of Errors. . . . . | 118 |
| 12. | Determination of $\xi(0)$ . . . . . | 121 |
| 13. | Counter Efficiencies. . . . . | 133 |

## List of Illustrations


| Figure | | Page |
|---|---|---|
| 1. | R, the ratio of the pi-mu atom and $K_{\mu 3}$ branching ratios, as a function of $\xi$ for three values of $\lambda_+$. | 8 |
| 2. | A schematic of the experimental apparatus . . . | 10 |
| 3. | The M3 beam line. . . . . | 14 |
| 4. | The spectrometer layout . . . . . | 20 |
| 5. | The $K_L^o$ momentum spectrum at the production target. | 30 |
| 6. | The relative retrieval efficiency for foil and beam events as a function of an identical efficiency for all ten wire planes . . . . . | 39 |
| 7. | Four $K_{\mu 3}$ topologies. . . . . | 41 |
| 8. | The distribution in $FRAC_n$ for identified pions and electrons . . . . . | 45 |
| 9. | The $M_{p\pi^-}$ distribution for the target-in calibration data . . . . . | 49 |
| 10. | The distribution of the longitudinal intersection of single particles with the beam for target-in calibration data. . . . . | 51 |
| 11. | The distributions of the transverse locations of single particles projected to the target for target-in calibration data . . . . . | 52 |

List of Illustrations (con.)

Figure Page

12. Two particle vertex distributions for raw triggers. . 54

13. The maximum separation in the side view distributions for raw triggers . . . . . 55

14. The distribution in the distance of closest approach the tracks for EE triggers. . . . . 56

15. The technique used to track single particles to a decay point within the beam . . . . . 59

16. The distribution of the horizontal distance of projected tracks from the beam center for gamma events . . 60

17. The longitudinal vertex distribution for $K_{\mu 3}$ triggers. 61

18. The SIZE distribution for $K_{\mu 3}$ triggers. . . . . 62

19. The $FRAC_{total}$ distribution for pi-mu atom candidates . 65

20. The distribution in $\alpha$ for pi-mu atom candidates. . . 66

21. The $p_t$ distributions for pi-mu atom candidates and the simulated background. . . . . 68

22. Comparison of data to the Monte Carlo prediction for the $p_t$ distribution of pi-mu atoms . . . . . 70

23. Comparison of data to the Monte Carlo prediction for the longitudinal vertex distribution of atoms . . 71

24. Comparison of data to the Monte Carlo prediction for the momentum distribution of pi-mu atoms . . . . . 72

List of Illustrations (con.)

Figure Page

25. Comparison of data to the Monte Carlo prediction for the proper time distribution of pi-mu atoms . . . 73

26. The distribution of the horizontal distance of the vertex from the beam center for $K_{\mu 3}$ events . . . . . 75

27. The longitudinal vertex distribution for $K_{\mu 3}$ events . . 76

28. The $K_L^o$ momentum distribution for $K_{\mu 3}$ events. . . . . 77

29. The $p_t$ distribution for gamma events . . . . . 79

30. The longitudinal vertex for Class 1 events before and after imposing vertex requirements plus that for the simulated background . . . . . 83

31. As in figure 30 for Class 2 events. . . . . 84

32. As in figure 30 for Class 3 events. . . . . 85

33. As in figure 30 for Class 4 events. . . . . 86

34. The $p_t$ distributions for like and opposite charge beam events . . . . . 87

35. The distributions in the horizontal distance of the vertex from the beam center for Class 1 and Class 2 events. 89

36. The square of the momentum versus the momentum squared times the position resolution squared for wire plane 6 . 93

## List of Illustrations (con.)

Figure Page

37. Comparison of data to the Monte Carlo prediction for the ARG distribution of $K_{\mu 3}$ events . . . . . 96

38. The vertical target sweep for Monte Carlo generated $K_{\mu 3}$ events . . . . . 97

39. The vertical target sweep for data and Monte Carlo $K_{\mu 3}$ events . . . . . 98

40. The horizontal target sweep for data and Monte Carlo $K_{\mu 3}$ events . . . . . 99

41. Comparison of data to the Monte Carlo prediction for the SIZE distribution of $K_{\mu 3}$ events. . . . . .101

42. Comparison of data to the Monte Carlo prediction for the $K_L^o$ momentum distribution of $K_{\mu 3}$ events . . . . .102

43. Comparison of data to the Monte Carlo prediction for the momentum distribution of gamma events. . . . . .103

44. Comparison of data to the Monte Carlo prediction for the $p_t$ distribution of $K_{\mu 3}$ events . . . . . .104

45. Comparison of data to the Monte Carlo prediction for the longitudinal vertex distribution of $K_{\mu 3}$ events. . .105

46. Comparisons of data to the Monte Carlo predictions for the pion and muon energy distributions in the kaon center-of-mass for $K_{\mu 3}$ events. . . . . .107

List of Illustrations (con.)

Figure Page

47. The variation in the relative pi-mu atom to $K_{\mu 3}$ acceptances as a function of the fraction of $K_L^o$'s produced with momentum less than 60 GeV/c. . . . . 109

48. The distributions in the separation between the two struck counters in the W and H counter banks for single muons. . . . . 114

49. The probability of an extra struck counter in the W and H counter banks as a function of the rate per pulse in the W bank for $K_{\mu 3}$ events . . . . . 116

50. Comparison of data to the Monte Carlo prediction for the proper time distribution of pi-mu atoms . . . . . 122

51. A pi-mu atom passing a nucleus of charge Ze . . . . . 128

52. The error on the relative foil to beam retrieval rate as a function of an identical error on the efficiencies of all ten wire planes . . . . . 131

## Abstract

Pi-mu atoms consisting of a charged pion and an oppositely charged muon in a Coulomb-bound state can be formed in $K_L^o$ decay. A sample of 216 pi-mu atoms collected during an experiment performed at Fermilab provide the first measurement of the rate of formation of these atoms. Using a subset of 140 atoms, the ratio of pi-mu atom decays to $K_L^o \rightarrow \pi\mu\nu$ decays has been measured to be $(3.73 \pm 0.40) \times 10^{-7}$. This is to be compared to the theoretical prediction of $(4.40 \pm 0.16) \times 10^{-7}$.

## I. Introduction

Pi-mu atoms consisting of a charged pion and an oppositely charged muon in a Coulomb-bound state can be formed in either $K_L^o$ decay or $\mu$-p interactions.[1] These atoms were initially predicted by Nemenov[2] and were first detected experimentally by Coombes et al[3] in an experiment performed at Brookhaven National Laboratory. The properties of these atoms depend upon the nature of the $\pi$-$\mu$ interaction. Specifically, the rate of formation is predicted to be about $10^{-7}$ of all $K_L^o$ decays and depends upon the value of the pi-mu atom wave function at the origin; i.e. at the point of formation. A measurement of this formation rate can be used as a probe of the short range interactions between pions and muons. Any deviations from the expected rate could indicate anomalous $\pi$-$\mu$ interactions.[4] Also, if the standard electro-weak interaction between the pion and the muon is assumed, the rate of formation can be used to determine $\xi$, the ratio of $K_L^o \to \pi\mu\nu (K_{\mu 3})$ form factors $f_-$ and $f_+$.

This paper describes in detail an experiment performed at Fermilab in which the first measurement of the rate of formation of pi-mu atoms has been made by detecting two body $K_L^o \to (\pi\mu)_{atom}\nu$ decays while simultaneously measuring the $K_L^o$ flux through the decay $K_L^o \to \pi\mu\nu$. The measurement of this rate is then compared to the current theoretical prediction for its value.

## II. Theory

Pi-mu atoms are an electromagnetically bound state of a charged pion and a muon, and can be described using the same formalism as the hydrogen atom. The properties of these atoms have been discussed elsewhere[5-7] with some of them being given in Table 1. As the binding energy of the 1S state is 1.6 keV, these atoms are a good approximation of a non-relativistic system.

The partial width $\Gamma_{nA}$ for $K_L^o$ decay into the pi-mu atom state of principal quantam number n, $(\pi\mu)_n$, is given by[8]

$$\Gamma_{nA}=\frac{1}{2m_K}\ (2\pi)^4|M|^2\delta^4(P_K-P_{ATOM}-P_\nu)\,d\omega_{ATOM}d\omega_\nu$$

where

$$M=\langle(\pi\mu)_n\nu|H|K_L^o\rangle$$

and $P_i=(\vec{p}_i,p_i^o)$ is the 4-momentum of particle i with $d\omega = d^3p_i/(2\pi)2p_i^o$. The matrix element M has been calculated in two ways. The first, initially described by Nemenov[9], consists of first integrating over a complete set of states in the variable q', the relative momentum between the pion and muon. This gives

$$M = \int d^3q'\langle(\pi\mu)_n\nu|\pi\mu(q')\rangle\langle\pi\mu\ (q')\nu|H|K_L^o\rangle.$$

Table 1. Properties of Pi-Mu Atoms

| | |
|---|---|
| Reduced mass | 60.13 $MeV/c^2$ |
| Radius | $4.5 \times 10^{-11}$ cm |
| Binding energy | $(1.6\ keV)/n^2$ |
| Lifetime | $2.6 \times 10^{-8}$ sec ($\tau_\pi$) |

But $<(\pi\mu)_n\nu|\pi\mu(q')\nu> = \psi_n^*(q')$ so that

$$M = \int d^3q'\psi_n^*(q')<\pi\mu(q')\nu|H|K_L^o> .$$

The wave function $\psi_n^*(q')$ is only non-zero over a small range in q' (<q'> is about 400 keV/c). If it is assumed that the term involving the interaction Hamiltonian varies slowly over this range, then it can be taken outside the integral giving:

$$M = <\pi\mu(q'\sim 0)\nu|H|K_L^o>\int d^3q'\psi_n^*(q') .$$

The last factor is the Fourier transform of $\psi_n^*(r=0)$. This yields

$$|M|^2 = |<\pi\mu(q'\sim 0)\nu|H|K_L^o>|^2|\psi_n(r=0)|^2 .$$

The square of the wave function evaluated at the origin is due to the point-like nature of the decay and has as its consequence that all atoms are formed in S states (with P states contributing less than 1%).Using the $K_{\mu 3}$ Lagrangian

$$L \sim \{(P_K + P_\pi)_\alpha f_+ + (P_K - P_\pi)_\alpha f_-\}\bar{u}_\nu\gamma_\alpha\tfrac{1}{2}(1-i\gamma_5)v_\mu$$

and integrating over phase space, the partial width becomes

$$\Gamma_A = \sum_n \Gamma_{nA} = BB \times (2m_\pi + m_\mu + \xi(q^2)m_\mu)^2$$

with

$$BB = \frac{G_F^2 \sin^2\theta_C (m_K - m_{ATOM})^2}{16\pi^2 m_K^3 m_\pi} \sum_n |\psi_n(r=0)|^2 |f_+(q^2)|^2$$

and

$$\sum_n |\psi_n(r=0)|^2 = 1.2\left(\frac{\alpha m_\pi m_\mu}{m_{ATOM}}\right)^3$$

The $K_{\mu 3}$ form factors have the standard definitions:

$$f_\pm(q^2) = f_\pm(0)(1 + \lambda_\pm q^2/m_\pi 2)$$
$$\xi(q^2) = \frac{f_-(q^2)}{f_+(q^2)}$$

with $q^2 = (P_K - P_\pi)^2 = 0.091\ (\mathrm{GeV/c})^2$ for atom formation.

Recently, Ching, Ho and Chang have used the approximate solution of the Bethe-Saltpeter equation for the pi-mu atom wave function to calculate M to the next order in $\alpha$.[10] They calculate M directly, without inserting a complete set of states in q'. Their results for $\Gamma_A$ are:

$$\Gamma_A = BB \times A^2 \times \{2m_\pi + m_\mu + \xi(q^2)m_\mu - \frac{m_\pi(a_R - b_R)}{(1 - D_1 - \frac{G_1 m_{ATOM}}{2m_\mu})}\}^2$$

with

$$A = 1 - \frac{\alpha}{\pi}(1 - \ln\alpha - \ln\mu_a - (\mu_b + \frac{\mu_a}{2})\ln\frac{m_\pi}{m_\mu})$$
$$a_R = (1 + \mu_b \ln\frac{\mu_a}{\mu_b})(1-\xi) - \tfrac{1}{2}\ln\lambda_+ + \tfrac{1}{2}\ln\lambda_-$$

$$b_R = \mu_b(1-\xi)\ln\frac{\mu_a}{\mu_b}$$

$$D_1 = \frac{\alpha}{\pi}(1-\ln\alpha-\ln\mu_a-\mu_b\ln\frac{\mu_a}{\mu_b})$$

$$G_1 = \frac{\alpha\mu_a}{\pi m_{ATOM}}\ln(\frac{\mu_a}{\mu_b})$$

$$\mu_a = \frac{m_\pi}{m_{ATOM}} \qquad \mu_b = \frac{m_\mu}{m_{ATOM}}$$

Using this second more exact calculation and normalizing to the partial width for $K_L^o \to \pi\mu\nu$ decays[11]

$$\Gamma(K_L^o\to\pi\mu\nu)=4\Gamma_o\sin^2\theta_C f_+^2(0)\{0.7728+4.2474\lambda_+ + 0.0223\xi^2(0) + 0.1828\xi^2(0)\lambda_- + 0.1492\xi(0) + 0.5234\xi(0)(\lambda_+ + \lambda_-)\} \times 10^{-2}$$

with

$$\Gamma_o = \frac{G_F^2(m_{K^o}+m_{K^-})^5}{64\pi^3}$$

the ratio

$$R \equiv \frac{(K_L^o \to (\pi\mu)_{ATOM}\nu\ )}{(K_L^o \to \pi\mu\nu\ )}$$

is obtained. Three small corrections to the value of R have been calculated. The effects of the finite size of the pion and vacuum polarization lower R by 0.37% and 0.19% respectively.[12] Radiative corrections to the $K_L^o\to\pi\mu\nu$ width lower R by 2.1%.[13] Including these, the ratio R is plotted in figure 1 as a function of $\xi(0)$ and $\lambda_+$. Using the current world averages of

$\xi(0) = -0.14 \pm 0.11$ and $\lambda_+ = 0.034 \pm 0.005$,[14] the predicted value of R is

$$R = (4.40 \pm 0.16) \times 10^{-7} .$$

The error is completely determined by those on the form factors and is discussed in Appendix A. This value of R is 1% lower than that found using Nemenov's technique.

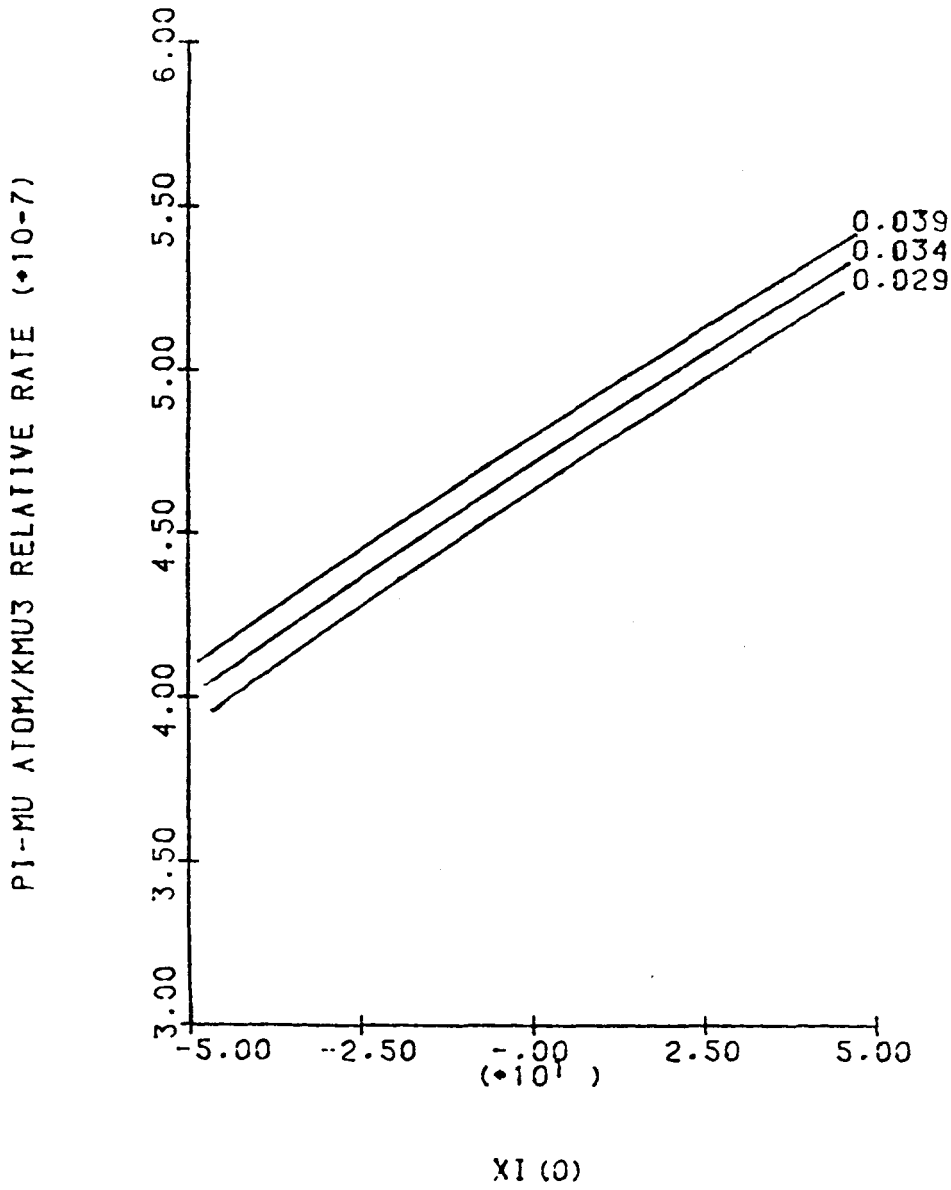


Figure 1. R, the ratio of the pi-mu atom and $K_{\mu 3}$ branching ratios, as a function of $\xi(0)$ for three values of $\lambda_+$.

## III. Experimental Technique

Any experiment which measures the branching ratio R is dominated in its design by the size of R, $10^{-7}$. A technique is needed which can detect atoms at a reasonable rate and simultaneously collect normalizing events from other $K_L^o$ decays.

The technique utilized in the present experiment consisted of forming a hot "beam" of pi-mu atoms by constructing an intense $K_L^o$ beam followed by a long decay region. In order to maximize the kaon production, this beam was produced by protons. The primary component of the beam was neutrons and, in order to reduce secondary particles from beam interactions, the beam travelled in uninterrupted vacuum outside the detection apparatus. The pi-mu atoms were then formed in $K_L^o$ decays and those with sufficient transverse momentum with respect to the $K_L^o$ direction emerged from the beam and were detected.

The detection apparatus (figure 2) consisted of a magnet which deflected charged particles vertically (MAGV), followed by a horizontally deflecting magnet (MAGH), a thin aluminum foil between these magnets and a magnetic spectrometer which measured the properties of charged particles. In order to identify the atomic constituents, the atoms were ionized in the foil. Calculations show that 0.32 mm of aluminum will ionize all atoms (see Appendix B). After this, the pion and muon remain spatially close to one another; the average multiple scattering in the foil

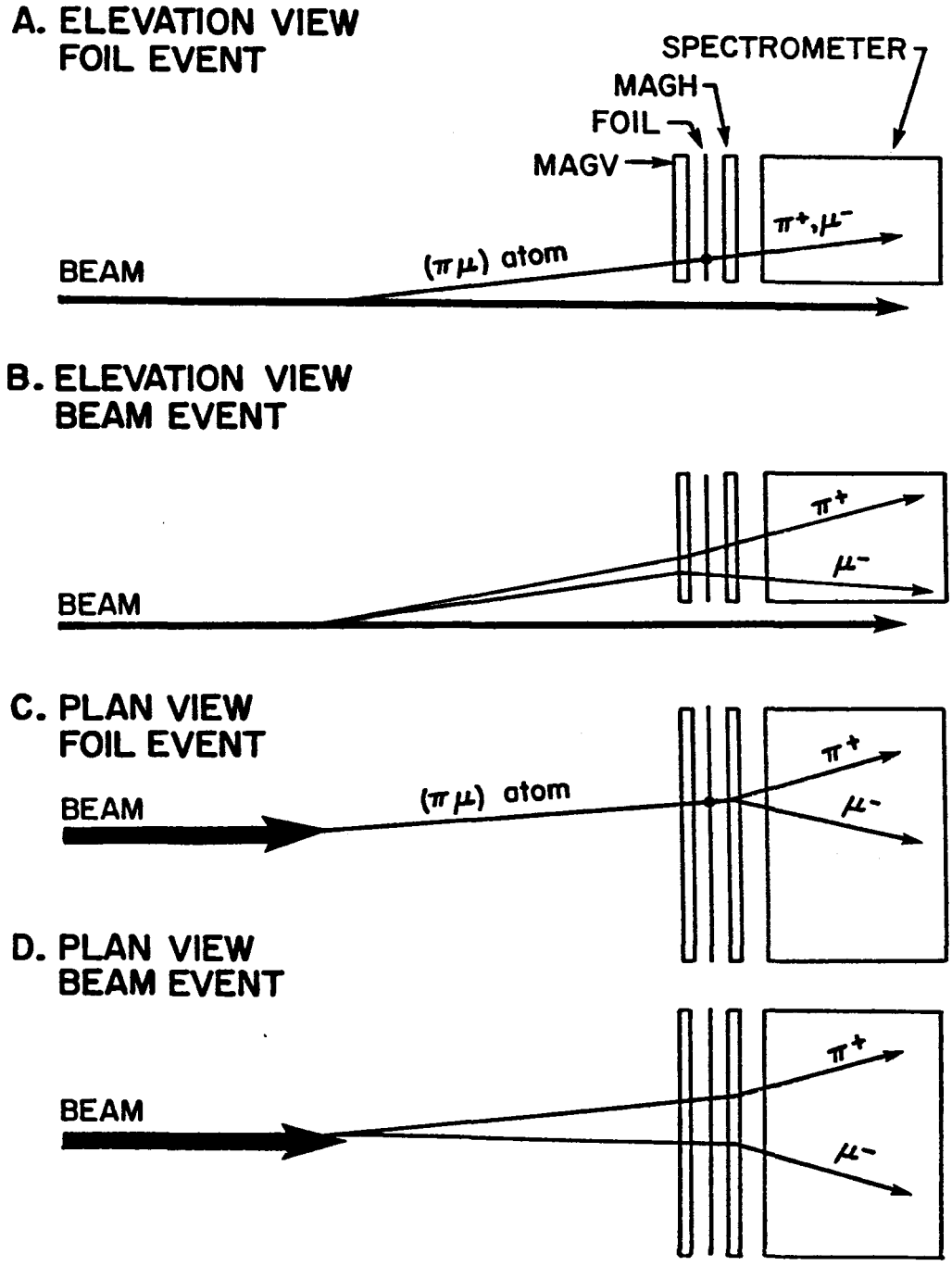


Figure 2. A schematic of the experimental apparatus used to detect pi-mu atoms and $K_{\mu 3}$ events (with examples of the foil and beam topologies).

being less than $10^{-4}$ radians. These particles were then passed through MAGH which separated the particles. This arrangement of foil and magnets produced two distinct classes of event topology (Refer to figure 2; Section VII-D-1 also discusses these two classes in greater detail). States which were neutral when they passed through MAGV and then ionized (pi-mu atoms) or converted ($\gamma$ rays) in the foil produced tracks in the spectrometer which, due to the effects of MAGH, lay in a plane whose normal was perpendicular to the transverse horizontal axis of the beam. This yielded two track projections in the top view with an apparent vertex in MAGH but only one in the side elevation view. Events with this topology were called "foil events". States consisting of separate charged particles (such as ordinary $K_L^o$ decays upstream of MAGV) were separated in both projections by the combined effects of MAGV and MAGH. Such events, with two or more projections in each view, were called "beam events".

Hodoscopes of horizontal counters were able to separate the two classes by requiring only one struck counter for a foil event while allowing more for beam events. Also, MAGV served to sweep unwanted charged particles out of the apparatus and to lower the acceptance for $K_{\mu 3}$ decays. These effects combined to allow triggering on both atoms and $K_{\mu 3}$'s at an acceptable rate (described in Section IV-D).

The experimental technique then consisted of simultaneously collecting foil and beam events and then identifying pi-mu atoms and $K_{\mu 3}$'s from these. A Monte Carlo calculation was then used to determine R.

While following the prodedure just described, it was also possible to identify $e^+e^-$ pairs arising from $K_L^0 \to \gamma\gamma$ where one of the gammas converted in the foil. These events were topologically similar to pi-mu atoms. A measurement of the ratio $(K_L^0 \to \gamma\gamma)/(K_L^0 \to \pi\mu\nu)$ provided an overall check on the experiment. Also, as the branching ratio for $K_L^0 \to \gamma\gamma$ is 1000 times that expected for pi-mu atoms, this mode served as a monitor of the quality of data over the course of the experiment.

# IV. Experimental Setup

## A. Beam and Decay Region

The M3 neutral beam, located in the Meson area at FNAL, is depicted in figure 3. The beam was formed by 400 GeV/c protons incident on a 30 cm beryllium target. The angle at which the protons were incident on the target (targeting angle) varied from 0.75 milliradians to 1.25 milliradians. The beam was defined by a fixed hole 1.8 cm wide by 1.2 cm high in a primary steel collimator located 15.4 m from the target.[15] Variable horizontal and vertical collimating stations were located at 117 m and 200 m from the target. These could be used to vary the beam size up to the limit imposed by the primary collimator. A magnet string following the primary collimator served to take the diffracted proton beam into another beam line and to sweep out other charged particles. Magnets located after each collimation station provided additional sweeping. From 2.54 to 7.62 cm of lead was placed in the beam at 113 m to convert photons. A vacuum region was provided between 127 m and 190 m to eliminate additional interactions in air.

The vacuum decay region began at 210 m and the neutral beam travelled through interrupted vacuum to 535 m. At 460 m the decay region ended but the neutral beam continued, running underneath the spectrometer in continuous vacuum. All pipes which ran through magnets were constructed from stainless steel. The region from

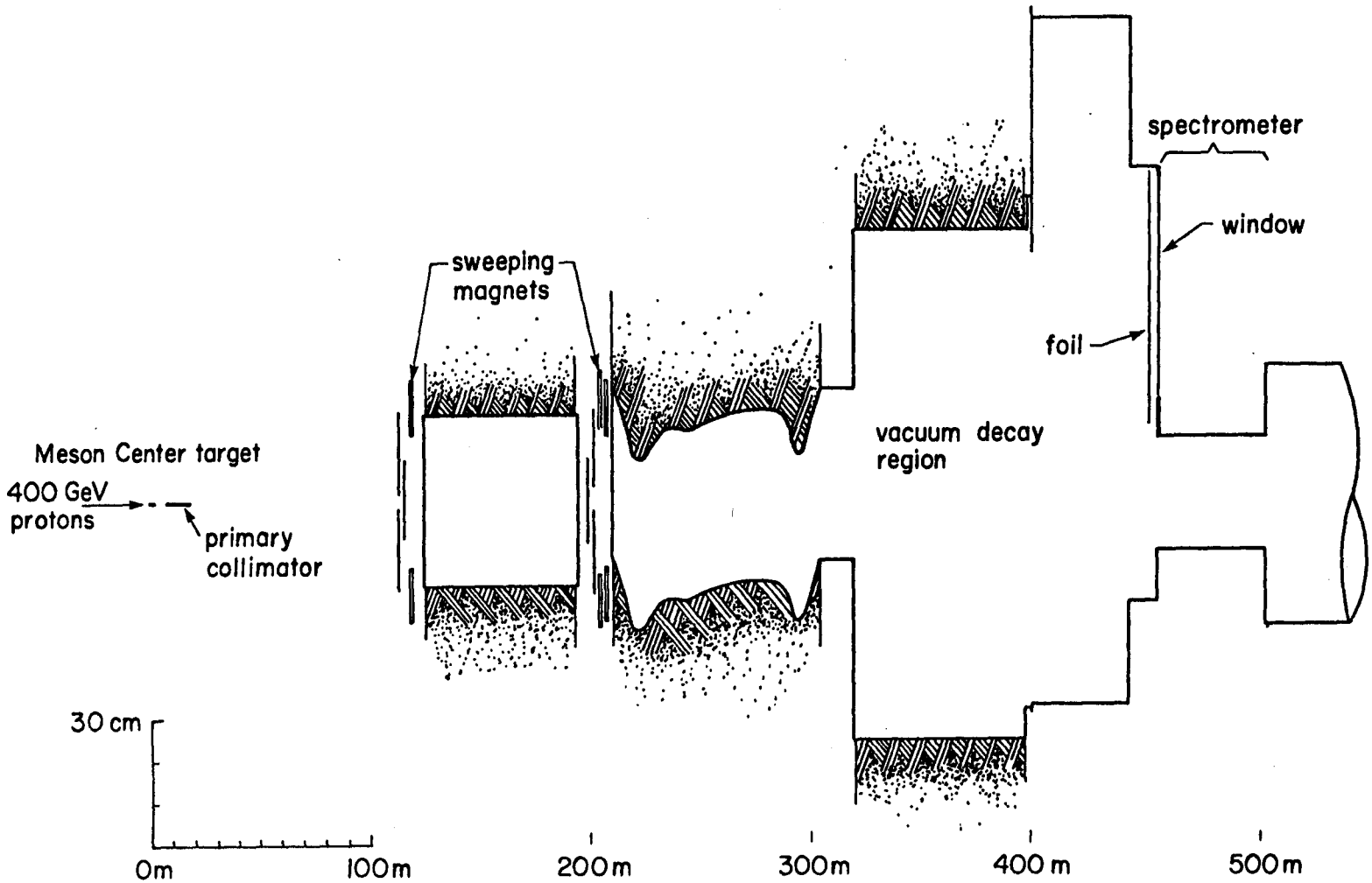


Figure 3. The M3 beam line at Fermilab.

210 m to 460 m was held at a pressure of approximately 12 microns of mercury throughout the data taking period. Neutron interactions in the residual air did not contribute to either the pi-mu atom or $K_{\mu 3}$ signals. They did provide a small background for $K_L^o \to \gamma\gamma$ events. This is discussed in reference 16.

The maximum aperture as defined by the primary collimator was 0.9 μster. A settling of the pipe at 280 m (seen in figure 3) reduced the usable size to 0.1 μster. This produced a beam size of 26.7 x 6.2 $cm^2$ at 400 m from the target.

The primary components of this beam were neutrons and $K_L^o$'s. The $K_L^o$ flux was approximately $2.4 \cdot 10^7$ $K_L^o/10^{12}$ protons on target/μster which at normal data taking conditions of $5 \cdot 10^{12}$ protons/pulse and $6.8 \cdot 10^{-2}$μster gave $8 \cdot 10^6$ $K_L^o$/pulse. The flux of neutrons depended on the targeting angle and the n/K ratio varied from approximately 50/1 to 125/1.[17]

The principal features of the M3 neutral beam line as used in this experiment are summarized in Table 2.

## B. Vacuum Window

At 460 m from the target the decay region ended. In order to minimize the amount of material traversed by particles emerging from the decay region, a special window was constructed. The window was approximately D-shaped, filling the upper 5/8 of the 81 cm diameter

Table 2. Properties of the Fermilab M3 Neutral Beam

| | |
|---|---|
| targeting angle | 0.75 - 1.25 milliradians |
| solid angle | $1 \times 10^{-7}$ steradians |
| length decay region | 250 m |
| volume decay region | 125 $m^3$ |
| decay region vacuum | 12 microns of mercury |
| $K_L^o$/pulse/$5 \times 10^{12}$ protons | $8 \times 10^6$ |
| average $K_L^o$ momentum | 65 GeV/c |
| neutron/$K_L^o$ ratio | (75 - 125)/1 |

pipe. The design and fabrication of this window was performed by the Physical Science Laboratory of the University of Wisconsin.

The window system had three components: a main window, a backup window and a metering membrane. The main window was made from 0.019 g/cm$^2$ Kevlar biaxial woven fabric (Reeves #15726) with a urethane coat on both sides for a total weight of 0.068 g/cm$^2$. The backup window was an uncoated 0.024 g/cm$^2$ 440 denier polyester triaxial woven fabric (N.F.Doweave #BP44P). The metering membrane consisted of a urethane coated (one side) 0.007 g/cm$^2$ nylon fabric (Reeves #3906) of total weight 0.017 g/cm$^2$. A 3.2 cm bleed hole was cut in the center of this membrane to allow a 200 CFM flow at a pressure difference of one atmosphere. This was to lessen the effect of a catastrophic failure of the window. The total thickness of the window system was $2.5 \times 10^{-3}$ radiation lengths.

Due to the size of the vacuum region (125 m$^3$), a series of safety tests were performed upon the main window. These consisted of hydrostatic pressure tests at 30 Psig and long term (120 hrs) creep tests at 1½ times operating pressure (22 Psig).[18]

## C. Spectrometer Magnets

There were three magnet systems used in the spectrometer: MAGV, MAGH and MAGA. As mentioned above, MAGV was used to deflect particles in the vertical plane. MAGH and MAGA deflected particles

in the horizontal plane. These two magnets were operated with magnetic field integrals equal in magnitude but with opposite polarities.

MAGV was formed by placing two 0.84 m X 0.99 m X 1.12 m magnets end to end. These magnets were normally run with a combined field integral of 2.79 kG·m. The magnetic field of each magnet including the fringe fields had been previously measured with a calibrated flip coil in a 5.08 cm X 2.54 cm X 2.54 cm grid at an integrated field of 3.77 kG·m.[19] These measurements were used to form an approximate field map; further calibrations based on special data sets will be discussed later.

Two more magnets identical to those used in MAGV were used to form MAGH. These magnets were rotated $90^{\circ}$ relative to MAGV and run at a combined field integral of 5.70kG·m. The determination of the field map of MAGH was the same as for MAGV.

The main spectrometer magnet, MAGA, was used to measure the momentum of each particle. It had an aperture 2.5 m wide x 1 m high x 1 m along the beam. Magnetic shunt plates were attached to both sides of the magnet to reduce the fringe fields. The direction of the field was opposite that of MAGH with an integrated field of 5.54kG·m. The three components of the magnetic field integral have been previously measured at a magnetic field integral of 12.6 kG·m.[20] Each component was measured at 36,000 points within the field region in a 10 cm x 2.5 cm x 2.5 cm grid. Line integrals

$\int B_y dz$ were also taken through the magnet at each point within the same 10 cm x 2.5 cm grid. These were consistent with the grid point measurements. The field map was checked at the data taking conditions in the present experiment of 5.25 kG·m and, except for the overall normalization factor, found to be adequate. This checking procedure is described in Section VII-C.

## D. Ionizing Foil

Midway between MAGV and MAGH was placed a thin aluminum foil. It was located in the vacuum which terminated after MAGH. The foil was used to ionize pi-mu atoms and convert gamma rays. Two different thicknesses were used, 0.51 mm and 0.89 mm, with approximately equal amounts of data being collected with each. Each foil was approximately D-shaped, matching the terminating window.

## E. Counters and Trigger Logic

The elements of the spectrometer are shown in figure 4. There were six scintillation counter banks: W, A, G, H, B and MU. The W counter bank was placed immediately after the vacuum window and consisted of 7 horizontal counters, each 0.16 cm thick and 5.3 cm high. The active area approximated that of the D-shaped window. The H bank was formed from eleven 122 cm x 5.4 cm x 0.95 cm

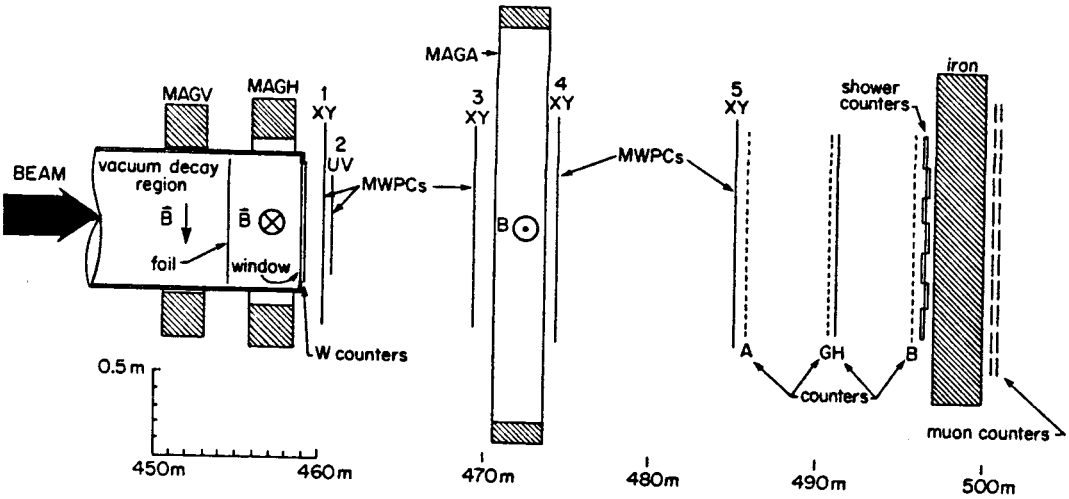


A. PI-MU ATOM SPECTROMETER PLAN VIEW

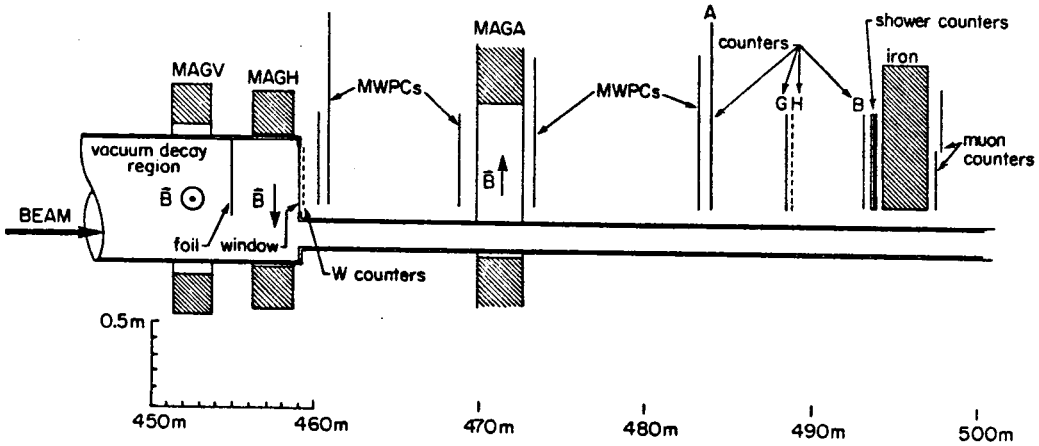


B. PI-MU ATOM SPECTROMETER ELEVATION VIEW

Figure 4. The spectrometer layout.

scintillators mounted horizontally and located about 5 m after the last wire chamber. The A, G, B and MU banks all consisted of vertical counters. The A bank, twenty-two 5.4 cm x 122 cm x 0.95 cm counters, sat immediately after the last wire chamber and was followed by the 24 G counters, each 5.1 cm x 61 cm x 0.32 cm, and the B bank, twenty-two 5.4 cm x 61 cm x 0.95 cm; with about 5 m separating each pair of banks. The 22 MU counters, each 1.3 cm thick, were located behind a 3 m thick steel wall and had a total active area of 1.6 m x 0.7 m. Each counter was connected to a single photomultiplier tube. The signal from each tube was discriminated and then those signals from each bank were logically added together to determine a specific requirement; e.g. = 2A if two and only two A counters were struck, $\geq$ 2A if two or more were struck, etc.

A shower counter bank was located just before the steel wall. Each of the 7 elements was made from 15 layers of lead, each 6.4 mm thick (17.3 radiation lengths total), interleaved with acrylic sheets. A light guide collected the Cerenkov light from the sheets and was viewed by a 12.7 cm phototube. The dimensions of each counter were 20 cm x 61 cm x 20 cm. Adjacent counters had a 2.5 cm overlap. The pulse from each tube was passively split into two signals. One of these was added to the signals from the other six tubes, with the resultant signal being discriminated at 40 mV. The counters were approximately balanced such that this level corresponsed to an electromagnetic energy deposition of about 3 GeV in

the bank. The other signal was integrated and digitized in an ADC and the value stored for later analysis. The behavior of these counters will be described in Section VII-B.

The pattern of the hits in the A and B bank was used to aid in reducing rates from unwanted triggers. A signal, TC, was formed if the pattern of struck A and B counters corresponded to that formed by two closely parallel tracks (as MAGH and MAGA were run with equal but opposite fields, most foil and beam topologies both satisfied this requirement). This signal was determined by requiring the pattern to be the same as one of a set of patterns residing in electronic memory. The technique used to determine this signal has been described previously.[21]

Three different basic triggers were defined. The KMU3 trigger was a general trigger for two track events with a muon. The more restrictive ATOM and EE triggers were designed to favor triggering on foil topologies over beam topologies. The logic signature for $K_{\mu 3}$ events was: $KMU3 \equiv \geq 1W \cdot = 2A \cdot \geq 2G \cdot \geq 1H \cdot \geq 2B \cdot \overline{\geq 5B} \cdot \geq 1MU \cdot TC$. (The restrictive trigger on the A and B bank aided in reducing the total trigger rate without biasing the pi-mu atom to $K_{\mu 3}$ determination.) The ATOM trigger was a subclass of KMU3 and was: $ATOM \equiv KMU3 \cdot = 1W \cdot = 1H$. A separate trigger for $e^+ e^-$ events consisted of removing the MU requirement from the ATOM trigger and requiring greater than 3 GeV deposited in the shower counters giving: $EE \equiv = 1W \cdot = 2A \cdot \geq 2G \cdot = 1H \cdot \geq 2B \cdot \geq \overline{5B} . TC \cdot > 3GeV$. Under normal

data taking conditions, the KMU3 trigger was prescaled by 32 and then events satisfying any of the three triggers were recorded simultaneously. When any trigger was satisfied, latch units recorded which counters had fired and the ADC's recorded the pulse height in each shower counter phototube.

## F. Wire Chambers

Particle trajectories were measured in multi-wire proportional chambers (MWPC's) whose use has been described previously.[22] Each of the 5 modules contained two orthogonal signal planes. Modules 1, 3 and 4 (see figure 4) had sets of vertical and horizontal wires which measured positions in the top and side view respectively. Module 2 had wires at $\pm 45^{\circ}$ to the vertical, whereas Module 5 was rotated by 41 milliradians relative to 1, 3 and 4. Module 3 was split, with separate readouts for the left and right halves of the horizontal wires. The first three modules had 61 cm x 122 cm active areas while modules 4 and 5 were each 99 cm x 140 cm. The chambers had 1.6 mm wire spacing with a 4.8 mm gap between the anode and cathode planes. The working gas was Ar-$CO_2$-Freon in the ratio 0.8:0.2:0.005. They were typically operated at 3500 V with a 300 V plateau and a 50 ns wide load pulse. The cathode wires were connected through a 1 Megohm guard resistor to the high voltage power supply to safeguard against catastrophic

failure. This limited the dark current which the chambers could draw to about 10 microamps (which would occur at a flux of $\sim 5 \times 10^6$ particles/sec in the chamber). The efficiencies of the chambers depended upon the dark current and varied from 88% to 99% in the different planes. The effect of these inefficiencies is discussed in Section VII-A.

## G. Data Acquisition System

The data acquisition system was controlled by a PDP 11/45 computer. There was also an additional auxiliary memory consisting of 64K 16-bit words which was used as an interface between the computer and the readout electronics of the proportional chambers.

Whenever a trigger occurred, the data acquisition program residing in the PDP-11 began the readout sequence. During this, the chamber hit information was written directly into the 64K memory. The trigger counters hit information was interfaced through coincidence registers which were directly read by the PDP-11 and then stored in the 64K memory. The pulse size information from the shower counters was digitized by LeCroy 2249 10-bit ADC's modified to be directly readable. This information was also deposited in the 64K memory. The entire readout sequence for one event required 250 microseconds, with each event being typically 50 words. No new trigger was accepted during this time. All of the data from

one beam pulse was temporarily stored in the 64K memory and then the accumulated contents were transferred to magnetic tape between beam pulses.

## V. Data Collection

Data was collected during a period from July to December of 1979. Various calibration sets were collected at intervals throughout this time.

### A. Main Data

The majority of the data was collected with the trigger previously described, a 24.3 cm x 4.5 cm beam at 400 m and a vacuum of 12 microns. The nominal flux of $8 \times 10^6$ $K_L^o$/pulse and from $4\text{-}10 \times 10^8$ n/pulse produced a trigger rate of about 250 triggers/pulse. This yielded about 0.002 pi-mu atoms /pulse or about 0.5 atoms/hour. The beam intensity was limited by the singles rate through the spectrometer which in turn was dominated by the neutron flux. A rate of about $5\times 10^6$ particles/pulse in the first chamber was maintained by either varying the size of the beam or the amount of lead at 113 m. All data was collected with one of three different beam sizes at 400 m: $24.3 \times 4.5$ cm$^2$, $14.5 \times 4.5$ cm$^2$ or $26.7 \times 6.2$ cm$^2$.

A total of 242 magnetic tapes were recorded at 800 bpi with an average of 160,000 events on each tape.

## B. Calibration Data Sets

Various calibration data sets were collected with special single track triggers. Single muons were collected by placing a 3.7 m steel beam stop in the beam. The trigger required one or more hits in each of the six scintillation counter banks. Muon data collected with MAGA turned off served to align the MWPC's and counters. During the data taking period, chambers 1 and 2 each had to be removed for repairs and the chambers were realigned following each such disturbance. A total of seven alignment sets were collected, interspersed with normal data collection. Sets with MAGA on were used to study the resolution of the chambers. Additional data using both single and two track triggers were collected with each counter bank removed in turn from the trigger. These counter studies were used to measure counter efficiencies and to determine the pattern of extra hits in each bank due to delta rays.

Two sets of magnet calibration data were collected; one midway and one at the end of the data taking period. During these, a 9.5 mm thick aluminum target which covered the beam was placed at 400 m from the meson target. This was used as an especially well-defined source of $\Lambda^0$'s and single particles produced in neutron interactions. $\Lambda^0$'s were collected with MAGV and MAGH turned off and MAGA run at its standard current. Reconstructed $\Lambda^0 \rightarrow p\pi^-$ decays were

used to set the overall strength of MAGA's field and also to check its field map. Single pions from this target were taken with MAGA always on and with MAGV and MAGH in the four combinations of on and off. These served to determine the magnitude of each magnet's field relative to MAGA and to check their field maps. Also, this data was used to locate the position of the beam at 400 m relative to the chambers. The results of these calibration sets are described in Section VII-C.

## VI. Monte Carlo Calculation

The primary purpose of the Monte Carlo calculation was to determine the relative detection efficiency for pi-mu atoms and $K_{\mu 3}$ decays. Also, by comparing Monte Carlo generated events to data, sources of possible systematics could be found and studied. In addition, backgrounds from decays such as $K_L^o \to \pi e \nu$ ($K_{e3}$) and $K_L^o \to \pi^+ \pi^- \pi^o$ ($K_{\pi 3}$) could be calculated.

The Monte Carlo calculation included standard Dalitz plot distributions for $K_{\pi 3}$ and $K_{e3}$ decays plus the first order radiative corrections for $K_{\mu 3}$ decays. The particles were tracked through the spectrometer with the effects of multiple scattering and chamber resolution included. The reproduction of the trigger counter performance included the inefficiencies and extra hit frequencies deduced from the calibration runs.

### A. $K_L^o$ Decays

The input $K_L^o$ momentum spectrum used to generate events followed the measurement of Skubic *et al.*[23] above 60 GeV/c. Below 60 GeV/c, the $K_L^o$ momentum spectrum was determined using $K_{\mu 3}$ events in the data. The input momentum distribution used is shown in figure 5. Decays were then generated using this spectrum over the length of the decay region, 210 m to 450 m, in an exponential

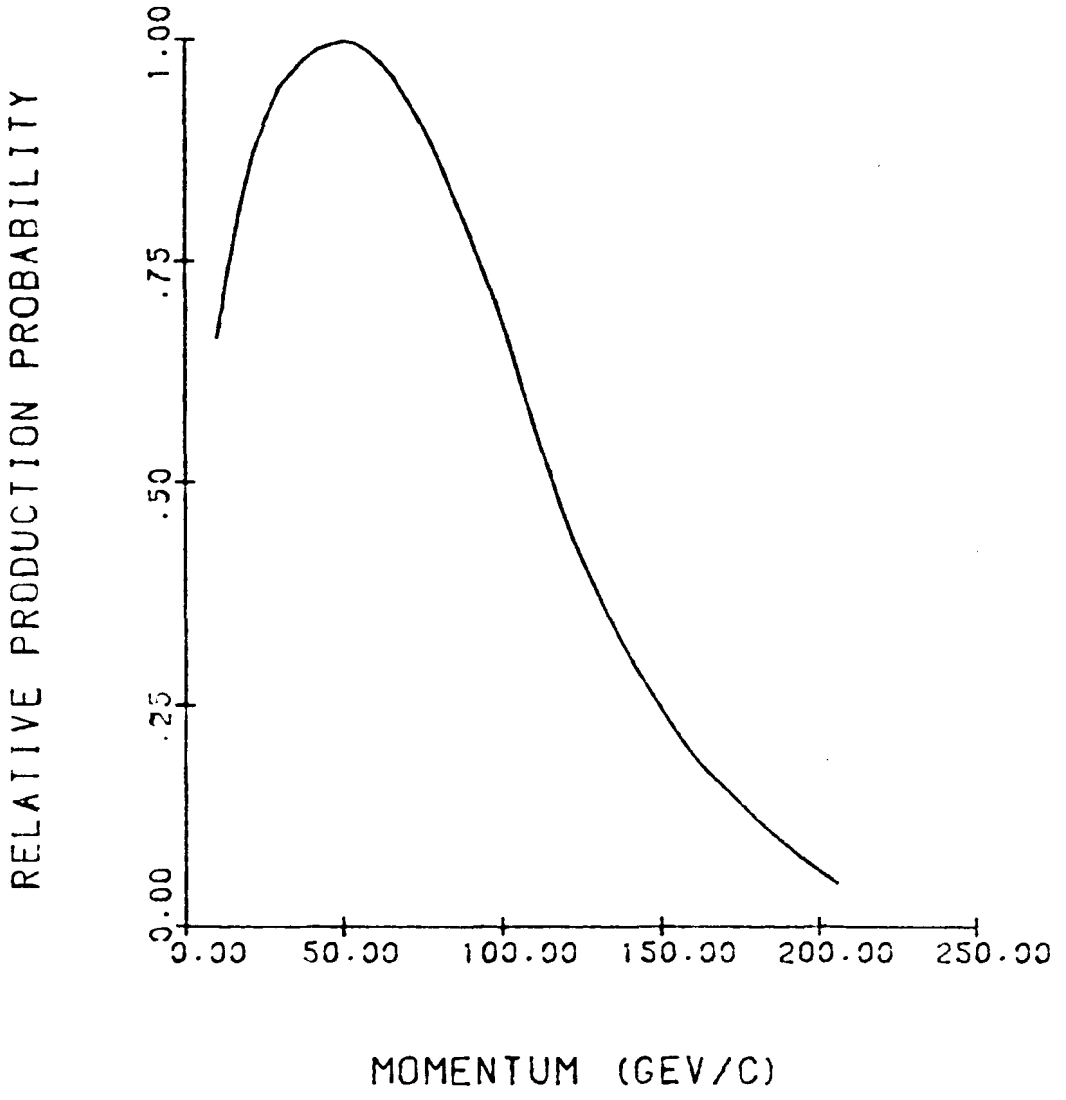


Figure 5. The $K_L^o$ momentum spectrum at the production target used as input to the Monte Carlo calculation.

distribution using the $K_L^o$ lifetime of $c\tau$ = 15.5 m. The transverse beam components of the decay point were distributed isotropically over the same dimensions as the data; i.e. a pyramid determined by the primary target as a point source and the collimators. Three beam sizes of 14.4 x 4.5 $cm^2$, 24.3 x 4.5 $cm^2$ and 26.7 x 6.2 $cm^2$ at 400 m corresponding to the major data taking conditions were generated.

Events from four decay modes were generated: pi-mu atoms, $K_{\mu 3}$, $K_{e3}$ and $K_{\mu 3}$. The events were generated in the kaon center-of-mass system with the particles then transformed to the laboratory system along the direction of the $K_L^o$. Pi-mu atoms were generated isotropicallyin the $K_L^o$ frame with a momentum of 189 MeV/c The atoms were then tracked as neutral particles to the stripping foil where they were immediately considered ionized to their charged components and then allowed to multiple scatter in the foil.

The $E_\pi$ and $E_\mu$ for $K_{\mu 3}$ events were generated on a Dalitz plot which included the first order radiative effects calculated by Ginsberg.[24] This gave[25]

$$\Gamma\ (E_\pi,\ E_\mu) = \Gamma_o(E_\pi,\ E_\mu) + \Gamma_{rad}\ (E_\pi,\ E_\mu)$$

$$\Gamma_o\ (E_\pi,\ E_\mu) = f_+^2\ (q^2)\ (A + B\xi(q^2) + C\xi^2(q^2)\ )$$

$$A = m_K\ (2E_\mu\ E_\nu - m_K E_\pi^{\prime}\ ) + m_\mu^2 (E_\pi^{\prime}/4 - E_\nu)$$

$$B = m_\mu^2\ (E_\nu - E_\pi^{\prime}/2)$$

$$C = m_\mu^2 E_\pi^{\prime}/4$$

$$E_\pi' = E_\pi^{max} - E_\pi$$

$$= \frac{m_K^2 + m_\pi^2 - m_\mu^2}{2m_K} - E_\pi$$

where $\Gamma_{rad}$ is Ginsberg's virtual term. $K_{e3}$ events, used to determine the background in $K_{\mu 3}$ events from this source, were generated using just the $\Gamma_o$ corresponding to the electron mass.

The $K_{\pi 3}$ events were generated according to the matrix element:[26]

$$\Gamma(T_o) = 1 + \frac{2a_0 m_K}{m_{\pi^o}^2} (2T_o - T^{max})$$

where $T_o$ is the $\pi^o$ energy and $a_o = -0.277$.

Pion decays, $\pi \rightarrow \mu\nu$, were included for all Monte Carlo events using the pion decay length $c\tau = 7.802$ m. The decay muons were generated isotropically in the pion center-of-mass. For pi-mu atoms, if the pion decay occurred before the atom was ionized, the event was considered lost; if not, the pion decay was handled the same as other decay modes.

B. Tracking Through the Spectrometer

Each particle for the $K_L^o$ decay was tracked through each element of the spectrometer. The relative location of each element to that of the beam was determined either by surveying or through the data itself. Errors on these measurements were estimated and the effect on the relative acceptance studied. All magnetic

fields were assumed to be step functions which turned on at the magnets' pole pieces. The strengths of the fields were determined from the field maps of the magnets. Charged particles were tracked through each magnet in circular trajectories using these field strengths.

Multiple scattering was simulated in each element using one of two techniques. The thin elements (all but the shower counters and the steel wall) were treated using the Moliere theory to generate a standard distribution corresponding to $10^{-3}$ radiation lengths of aluminum.[27] This standard distribution was then sampled at random and the actual deflection obtained by scaling the sample $\theta_s$ by the factor:[28]

$$\theta/\theta_s = \frac{E_s\ (x)^{\frac{1}{2}}}{p}\ (1 + \frac{\log\ (10x)}{8})$$

where x was the thickness in radiation lengths of a given element in the spectrometer and $E_s$ depended upon the material of each element. Each particle was given a 22% chance of striking a chamber wire in passing through a MWPC module. If this occurred, x was scaled accordingly. The transverse scattering was found by:[29] $y = \frac{1}{\sqrt{3}} D\theta$ where D is the thickness of the element. The algorithm used to determine the scattering in the two thicker elements followed that of Rossi.[30] The angular and transverse displacement of the particles ($\theta$ and y) were determined using the probability:

$$P(\theta, y) = \frac{2\sqrt{3}}{\pi} \frac{1}{D} \frac{1}{\theta'^2} \exp\left\{\frac{-4}{\theta'^2}\left(\theta^2 - \frac{3y\theta}{D} + \frac{3y^2}{D^2}\right)\right\}$$

$$\theta'^2 = \left(\frac{E_s}{\beta c p'}\right)^2 \times$$

where $p'$ was equal to the incoming momentum minus one half the energy lost due to ionization in the element.

The intercepts of the two tracks in the MWPC planes were converted to wire hits using the following approximation. The distance between two adjacent wires was divided into three regions with the middle one being equidistant from both wires. If a track passed through the central region, both wires were considered struck. A track in one of the other two regions struck just the nearest wire. The width of the middle region was determined by the observed frequency of one and two wire hit events in the data.

Particle trajectories were also projected to the locations of each counter bank and, using the same dimensions and locations as in the experiment, hits were recorded in each struck counter. Counter efficiencies caused small differences in the ratio of the total pi-mu atom to $K_{\mu 3}$ acceptances due to slightly different illuminations. The measurement of the efficiencies of all counters is described in Appendix C and was also included in the Monte Carlo. Also, each track could have associated with it an extra hit from a delta ray. Again, the probability and pattern of this extra hit were determined in special data sets. Monte Carlo

events were constrained to pass through the same trigger requirements as the raw data and then both Monte Carlo and data events were processed by the same analysis program.

# VII. Reduction of Data

## A. Track Definition

The major goal of the track finding method used in this experiment was that the measurement of the pi-mu atom rate of formation not be a function of the method; i.e. that the retrieval rate for atom and $K_{\mu 3}$ events be nearly the same with any difference small and calculable by a Monte Carlo and that the relative rate be independent of chamber performance. Therefore, the algorithm used set fairly tight requirements on all event types which , while losing some events, aided in meeting this goal.

The algorithm used in finding two track events consisted of first converting the chamber information into side (nonbending) and top (bending) view hit locations, then forming line segments from these hits and finally combining the line segments into complete particle trajectories. Segments before and after magnet MAGA in the top view were combined by requiring the projection of these segments to the center of MAGA to be within 3.2 mm. The correlation between the side and top view segments was accomplished by using the information in the two rotated chambers. The side and top view hit locations in these chambers were given by

$$S_{ij} = U_i \sin\theta + V_j \cos\theta$$

$$T_{ij} = U_i \cos\theta - V_j \sin\theta$$

where $U_i$ and $V_j$ are the ith and jth hits in the two rotated planes and $\theta$ is the angle of rotation of the chamber. As $S_{ij}$ and $T_{ij}$ are formed by the same UV combination, a requirement that the side view segment including $S_{ij}$ be combined with its counterpart which contained $T_{ij}$ was used to determine which side and top view segments to combine together. These segments were then fitted to determine the track slopes in the front and back halves of the spectrometer and the common coordinate in the center of the magnet in the top view and a straight line in the side view to form a complete particle trajectory.

As stated before there were two topologies, the foil and beam, which had to be retrieved in an understandable way. The foil topology's two side view projections lay virtually on top of one another whereas, due to MAGV, the beam topology always had two separated side view projections. In fact, 30% of the foil events appeared to have only one side view segment when using only the information in the unrotated chambers. This required allowing events in which only one side view segment was found to be considered as good events with that one side view segment being assigned to both tracks. These events were then easier to retrieve as only one of the two segments needed to be identified. In order

to minimize this difference between foil and beam events the following procedure was used. Any side view segment was allowed to be missing a hit in any one of chambers 1, 2, 3 or 4. Since chambers 1 and 2 are close to one another (as are 3 and 4) a miss in any one caused little degradation in spatial resolution. Chamber 5 was rotated 41 milliradians so that the two tracks in a foil type event could be differentiated. Thus, the hit requirements in this chamber were the same for the two classes. This led to a retrieval rate as a function of the individual wire plane efficiencies for the foil and beam classes to be:

$$EFF_{foil} = E_5^2E_7^2E_9^2E_{10}^2\ (E_3^2E_4^2 + 2E_3E_4E_1^2(2-E_3-E_4))\ \times$$
$$(E_2E_6 + E_2E_8 + E_6E_8 - 2E_2E_6E_8)$$

$$EFF_{beam} = E_5^2E_7^2E_9^2E_{10}^2\ (E_3^2E_4^2(1-(1-E_6)(1-E_8))^2 +$$
$$2E_3E_4(2-E_3-E_4)E_1^2E_2(1-(1-E_6)(1-E_8))^2)$$

where the planes are numbered as in Table 3. A graph of ($EFF_{foil}$/ $EFF_{beam}$) for an identical $E_{chamber}$ for all ten planes is shown in figure 6. This shows the sensitivity of the retrieval rate ratio between the two classes to the chambers' efficiencies. The measured chamber efficiencies (Appendix C) are given in Table 3 and yield an ($EFF_{foil}/EFF_{beam}$) of 1.024 ± 0.011.

Beam events had a variety of topologies in the top view (see figure 7) whereas foil events always had that seen in figure 7a.

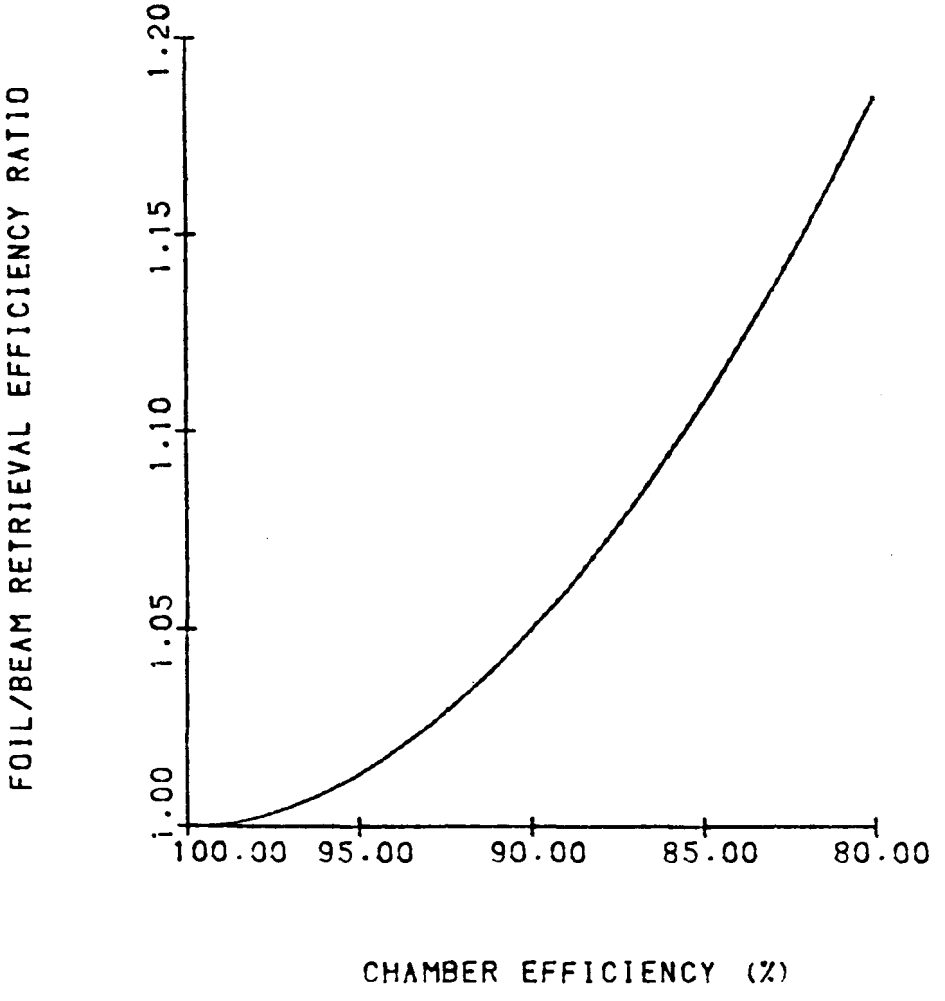


Figure 6. The relative retrieval efficiency for foil and beam topology events as a function of an identical efficiency for all ten wire planes.

Table 3. Chamber Efficiencies

| Wire plane | Efficiency (%) |
|---|---|
| 1. module 1 vertical plane | 91.4 ± 3.0 |
| 2. module 1 horizontal plane | 93.1 ± 3.0 |
| 3. module 2 U plane | 89.0 ± 3.0 |
| 4. module 2 V plane | 91.0 ± 3.0 |
| 5. module 3 vertical plane | 95.8 ± 3.0 |
| 6. module 3 horizontal plane | 94.3 ± 3.0 |
| 7. module 4 vertical plane | 96.3 ± 3.0 |
| 8. module 4 horizontal plane | 96.5 ± 3.0 |
| 9. module 5 vertical plane | 98.4 ± 3.0 |
| 10. module 5 horizontal plane | 97.5 ± 3.0 |

Track retrieval efficiency foil events - 72.6%

Track retrieval efficiency beam events - 70.9%

Foil/beam retrieval efficiency ratio - 1.024 ± 0.011

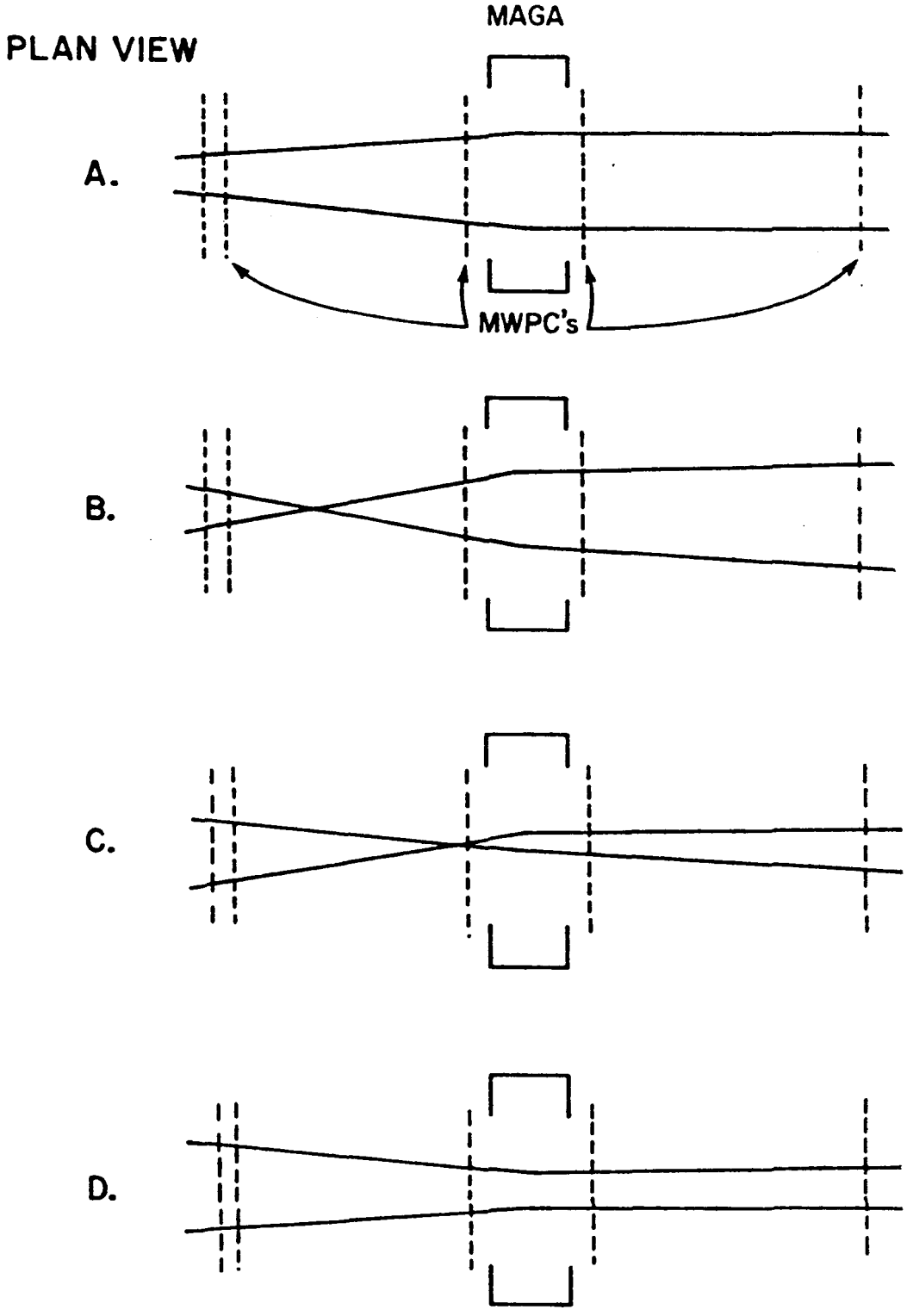


Figure 7. Four $K_{\mu 3}$ topologies.

Table 4. Comparison of $K_{\mu 3}$ Topology Classes

| | Fraction of total events (%) | |
|---|---|---|
| Class | Data | Monte Carlo |
| a | 58.1 ± 0.3 | 60.7 ± 1.3 |
| b | 9.8 ± 0.1 | 9.2 ± 0.4 |
| c | 0.13 ± 0.01 | 0.11 ± 0.04 |
| d | 32.0 ± 0.2 | 30.0 ± 0.8 |

Table 4 gives the fraction of well identified $K_{\mu 3}$ events in each class for data and Monte Carlo events. This agreement shows that any retrieval rate difference between the 7a topology and the other types was reproduced in the Monte Carlo. This implies that the Monte Carlo also reproduced the relative retrieval between foil and beam events. From this, and from a detailed study of individual events, the systematic uncertainty on the foil to beam track retrieval ratio due to the algorithm used was estimated to be less than 2.5%.

It was also possible to relax the requirements used to identify foil events and therefore obtain 25% more pi-mu atom events for use in studies of kinematic distributions. Gamma events were used to verify that the shapes of kinematic distributions were independent of the track retrieval requirements.

## B. Particle Identification

The spectrometer was able to identify leptons by using the lead-lucite shower counters and the MU hodoscope located behind 3 m of steel. Hadrons could only be identified by the absence of a lepton signal. The shower counters were tuned and studied using well identified gamma and $K_{e3}$ events (see Section VII - D-5).

An electron deposited about 98% of its energy in the shower counters. The pulse height, $PH_n$, in the shower counter which the

nth track struck (n being 1 or 2) was converted to the fraction of energy deposited by forming a quantity

$$FRAC_n = \frac{(PH_n - ADC_0)}{P_n} \times ADC$$

where $ADC_0$ was the offset of the appropriate ADC channel, $P_n$ was the momentum of the particle as measured with the spectrometer and ADC was a variable proportional to the gain. ADC was then adjusted for each counter so that $FRAC_n$ was distributed about 1.0 for identified electrons from gamma conversions. Figure 8 gives the $FRAC_n$ distribution for these electrons. For particles incident on the overlapped regions of the shower counters, $FRAC_n$ was determined by summing the two adjacent counters. For about 5% of the events, it was not possible to separately determine a $FRAC_n$ for each particle. A $FRAC_{total}$ was then determined by the ratio of the total energy deposited in the shower counter to the sum of the two charged momenta.

Well identified $K_{e3}$ events were used to determine the $FRAC_n$ distribution for pions (Note: Pions had about a 40% probability of interacting in the shower counters). If the $FRAC_n$ of one of the particles from these events was greater than 0.85, it was identified as an electron and the other particle was called a pion. Figure 8 also gives the $FRAC_n$ distribution of these pions.

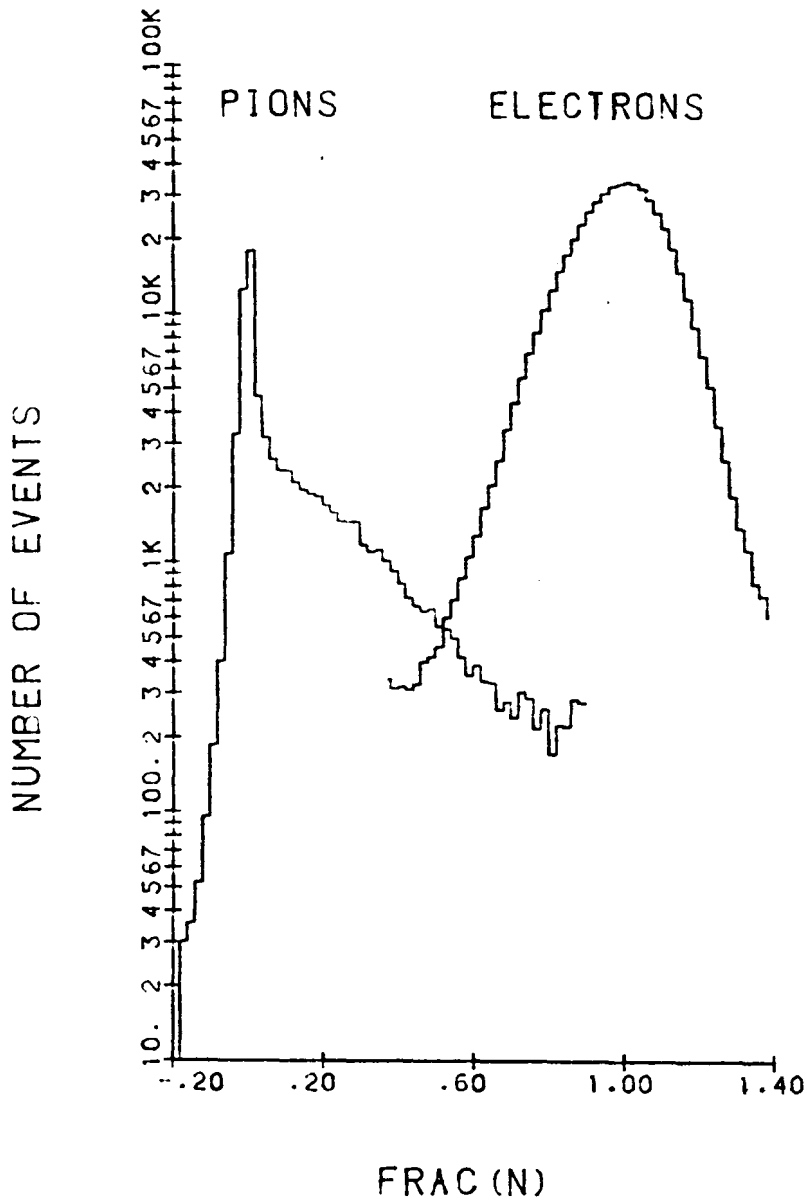


Figure 8. The distribution in $FRAC_n$ for identified pions and electrons.

The shower counter requirements for various particle combinations are given in Table 5. Also, from the distributions in figure 8, it was determined that 96% of the pions and 2.7% of the electrons had $FRAC_n$ below 0.7.

Muons were identified using the information in the MU hodoscope. In two track events, the probability for each track to have scattered into the area of any struck counter was determined assuming a Gaussian shape for the probability of a scatter into a given angle in passing through the steel wall. The track with the higher probability was labelled a muon. If, instead of doing this, the muon was simply identified as being that track closest to the struck counters, then greater than 98.5% of the events had identical muon assignments. This demonstrated that the muon identification was insensitive to the assigning technique. An ambiguous event was one where either both tracks had high probabilities to be a muon or where there were two or more separated muon counter hits. An event was determined to have a good muon identification if both tracks projected to the MU bank and if the muon identification was unambiguous. As the muon from both pi-mu atoms and $K_{\mu 3}$ events had very similar momentum distributions and MU bank illuminations, any systematic muon identification errors cancelled in determining the ratio of atom to $K_{\mu 3}$ events.

Table 5. Shower Counter Requirements

| Particles in event | $FRAC_n$ | $FRAC_{total}$ |
|---|---|---|
| $\pi\mu$ | both < .70<br>one < .20 | < .65 |
| ee | both > .70 | > .70 |
| $\pi\pi, \pi p$ | both < .70 | < .65 |

## C. Magnet Tuning

As previously described, the three magnets had had their field maps measured at different excitations than those at which they were run during this experiment. The overall strengths of these magnets were determined and the shapes of their field maps checked using data collected with a 9.5 mm aluminum target inserted into the M3 beam at a point 400 m from the meson target.

Two track events taken with this target (with MAGV and MAGH off) were used as a source of $\Lambda^{o}$'s. Events with the following characteristics were selected:

1. Two oppositely charged particles
2. Longitudinal vertex between 395 m and 435 m
3. Minimum separation of tracks at the vertex < 6 cm
4. Both tracks identified as hadrons
5. (Momentum positive)/(momentum negative) > 3

The positive track was then called a proton and the negative a pion and their invariant mass calculated. A peak was observed and the overall strength of MAGA was adjusted by 1.2% so that this peak centered on the known $\Lambda^{o}$ mass (see figure 9). A sample of 4000 $\Lambda^{o}$'s gave an overall accuracy on the field strength of 0.3%. The map was checked by dividing MAGA into four sections and determining the field strength for each region. All regions gave consistent results.

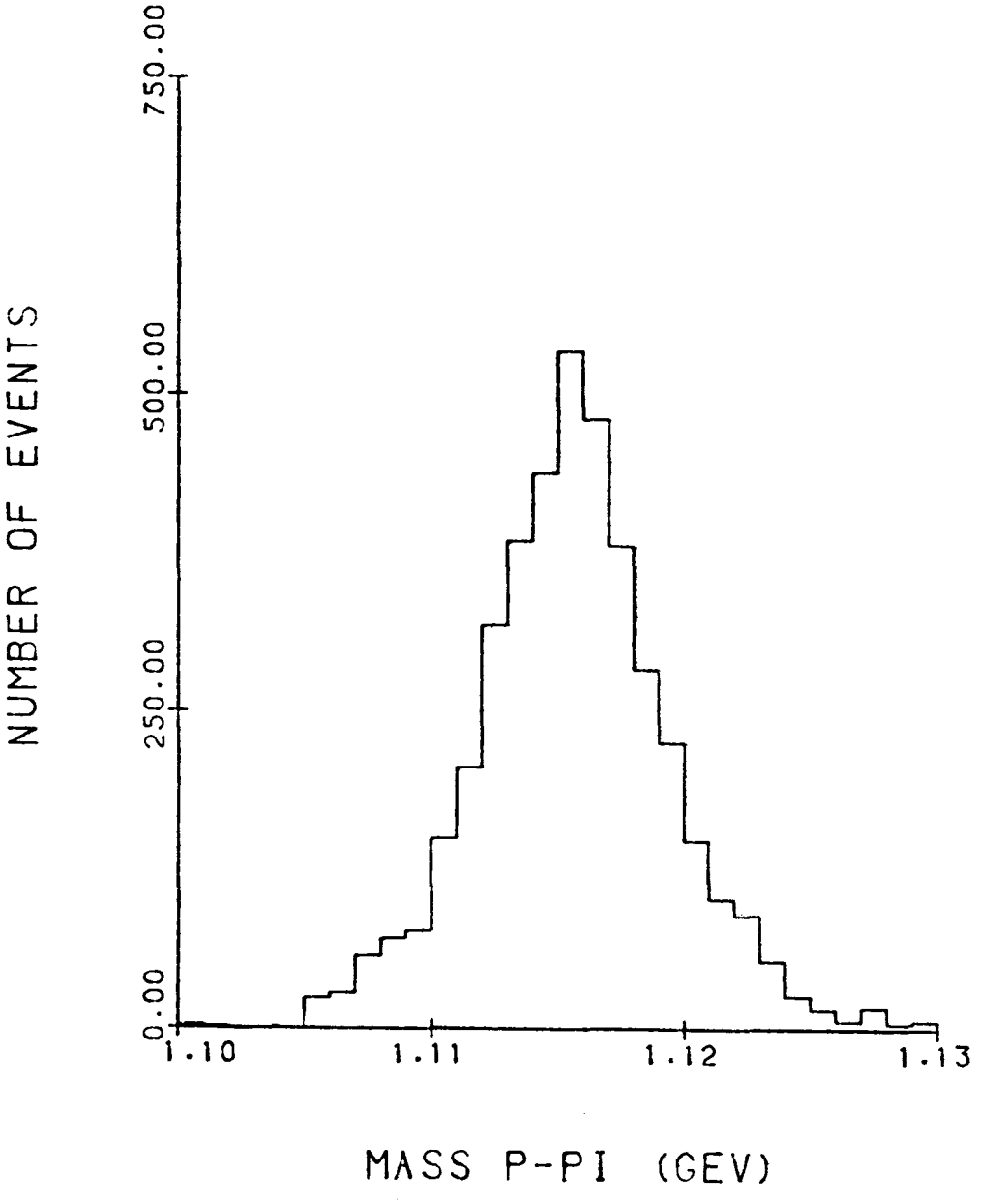


Figure 9. The $M_{p\pi^-}$ distribution for the target-in calibration data.

MAGV and MAGH were tuned relative to MAGA using pions produced by neutron interactions in the aluminum target. Figure 10 shows the intersection of single hadrons with the beam for data collected with both MAGV and MAGH turned off. The signal away from the peak at 400 m was primarily due to $K_L^o$ decays and was removed by requiring the momentum transverse to the beam to be greater than .230 GeV/c. Figure 11 gives the horizontal and vertical location of these pions projected to the location of the target. The central parts of these two distributions were fit to Gaussian shapes to determine their average. The data collected with the magnets off was used to determine the location of the beam relative to the spectrometer at 400 m.

Single pions from the target taken with just MAGV on and just MAGH on were tracked through each magnet using the approximate field map (see Section IV-C) weighted by BOOST X (1 ± Q) where the sign of Q depended upon the pion's charge. BOOST and Q were adjusted as a function of position in each magnet so that all particles of both sign projected to the known beam locations at the aluminum target. The overall strength of MAGV and MAGH relative to MAGA were determined to better than 0.3% with all deviations from the approximate field map being less than 0.9%.

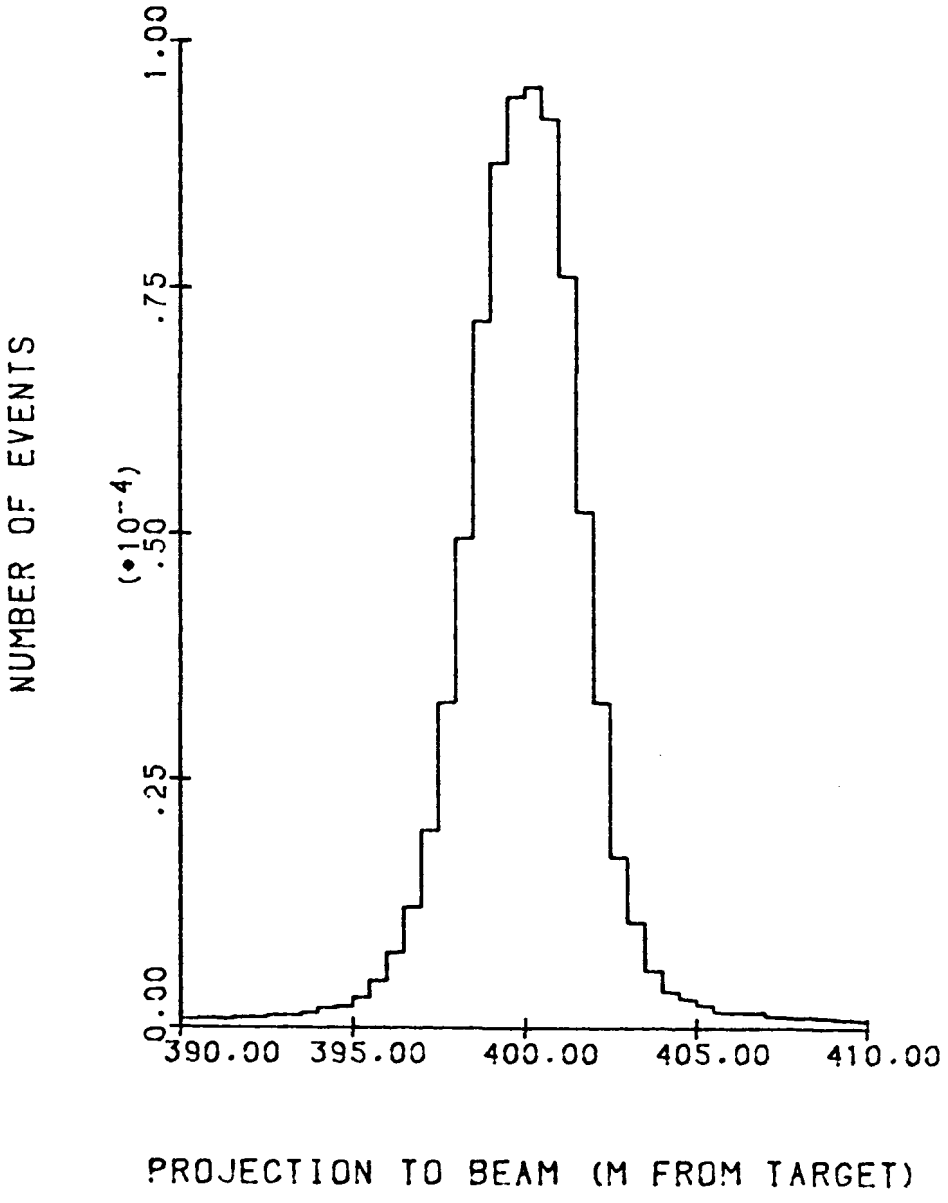


Figure 10. The distribution of the longitudinal intersection of single particles with the beam for target-in calibration data.

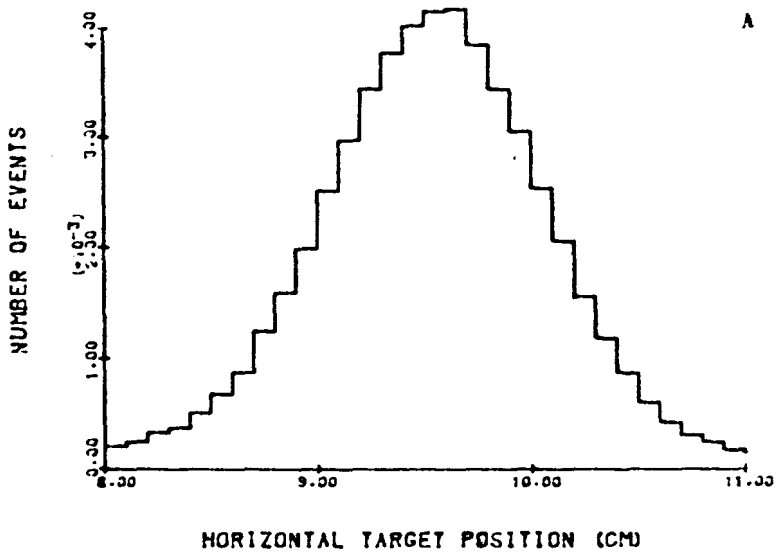


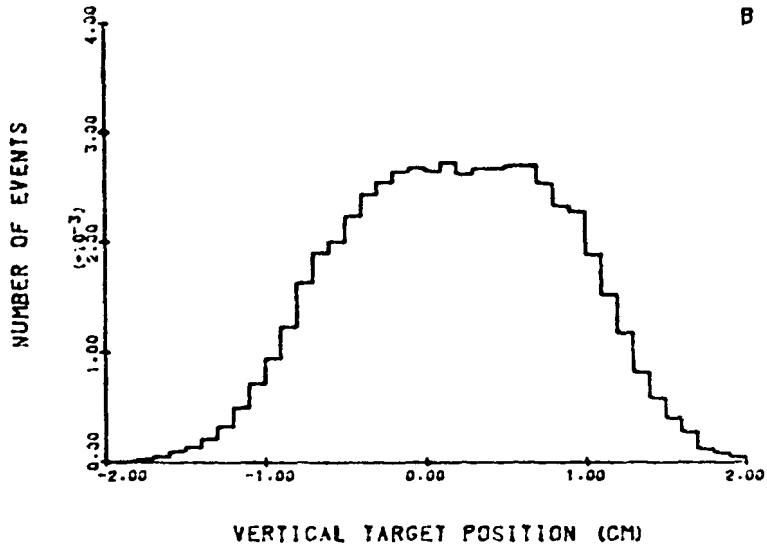


Figure 11. The distributions for the horizontal (A) and vertical (B) transverse locations of single particles projected to the target for target-in calibration data.

## D. Event Selection

### 1. General Classes

There were two basic classes of events looked at in this experiment (figure 2). The beam type consisted of $K_{\mu 3}$, $K_{e3}$ and $K_{\pi 3}$ events formed in $K_L^o$ decay. The foil type were formed from neutral particles converting to two charged particles in the aluminum foil. Examples of this type were pi-mu atoms and gamma conversions.

Foil type events had an apparent vertex in the center of MAGH. Also, due to the effect of MAGV, beam events had a clean separation in the side view. Figures 12 and 13 show the location of this vertex and the maximum separation in the side view for raw ATOM, KMU3 and EE triggers. Also shown in figure 14 is the separation in space of the two tracks at the vertex for EE events. A clean vertex centered on MAGH is seen for EE events. Also, beam and foil events can be clearly differentiated using the side view separation. The requirements that events had to satisfy to fall into one of the two classes are given in Table 6.

The technique used in tracking particles through MAGH and MAGV and then determining if the event originated in the beam depended upon whether the event was a beam or foil type. For foil types, the two particles were tracked through only MAGH and then

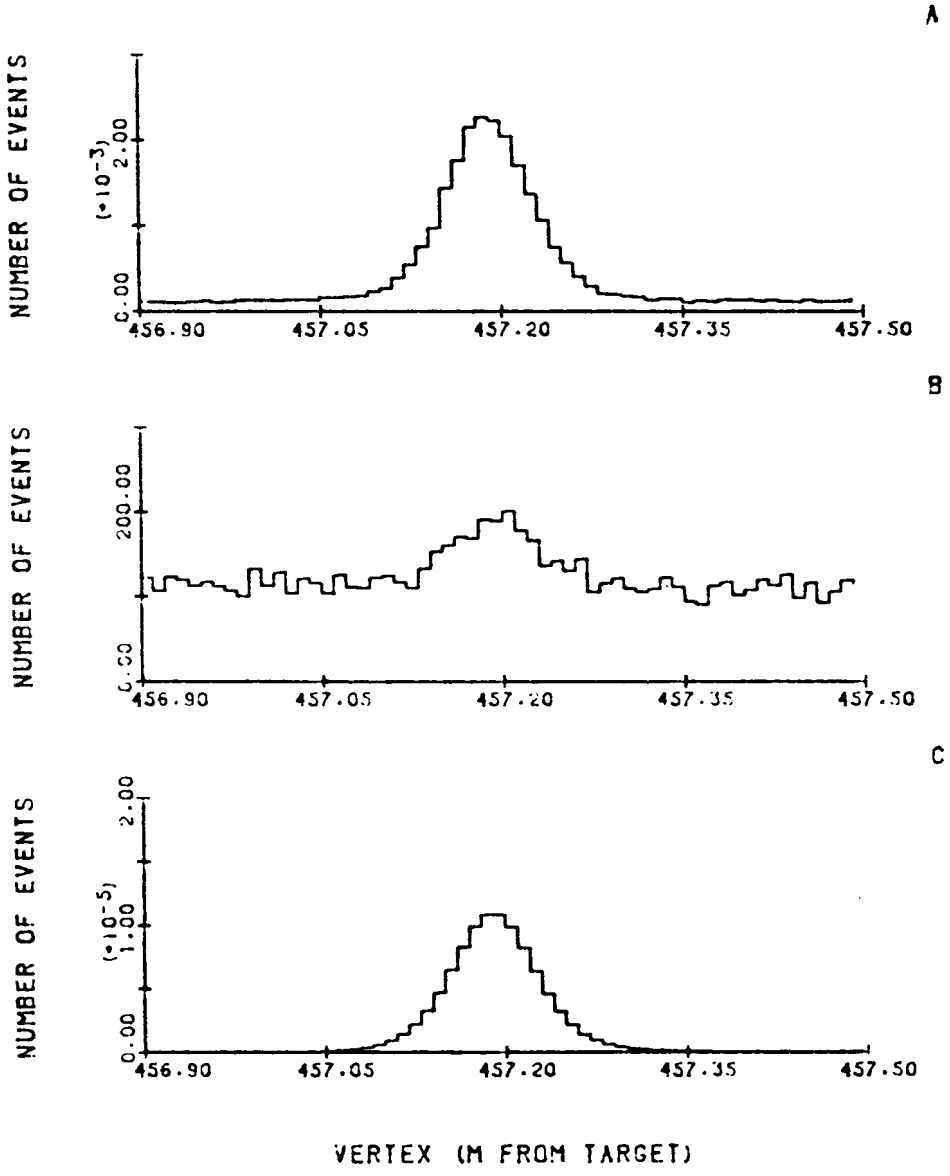


Figure 12. Two particle vertex distributions for raw ATOM (A), KMU3 (B) and EE (C) triggers.

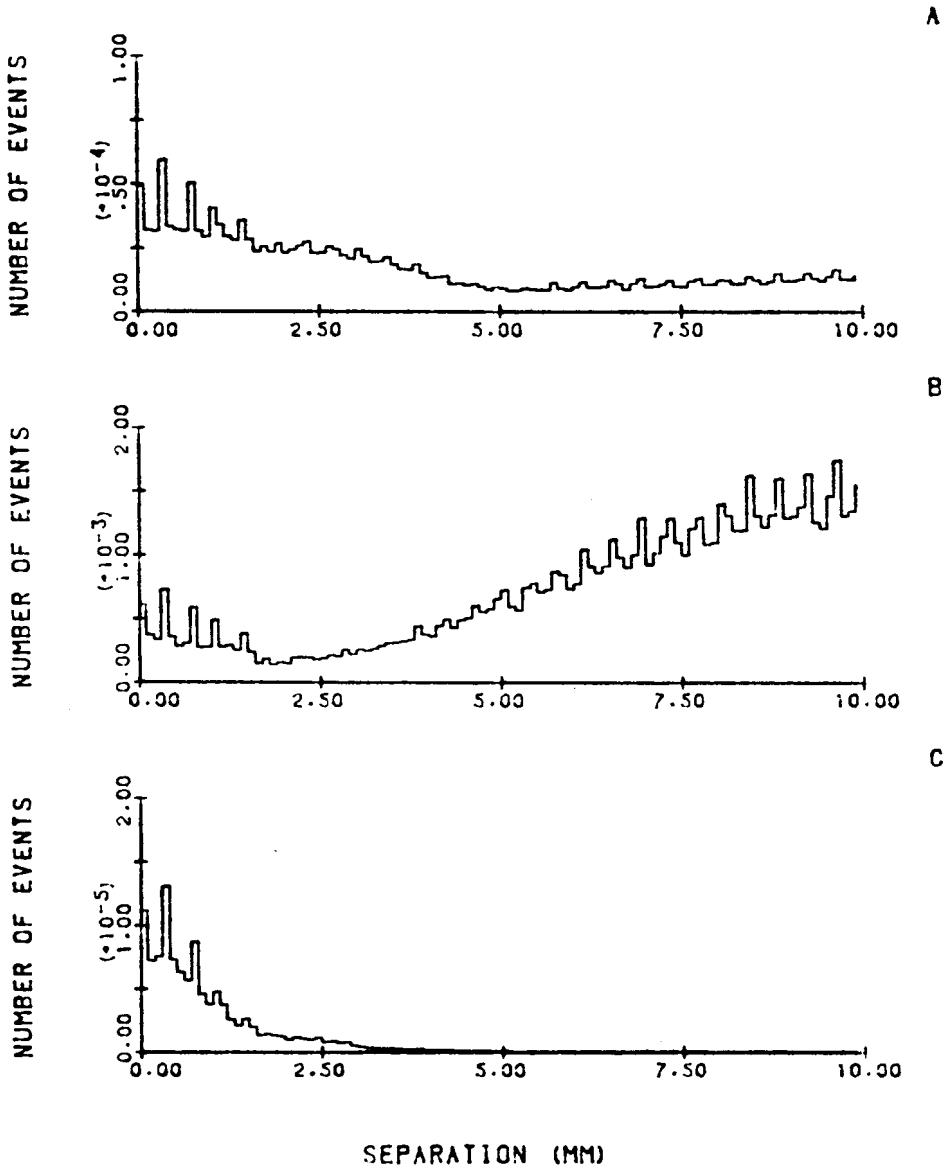


Figure 13. The distribution of the maximum separation between the tracks in the side view for raw ATOM (A), KMU3 (B) and EE (C) triggers.

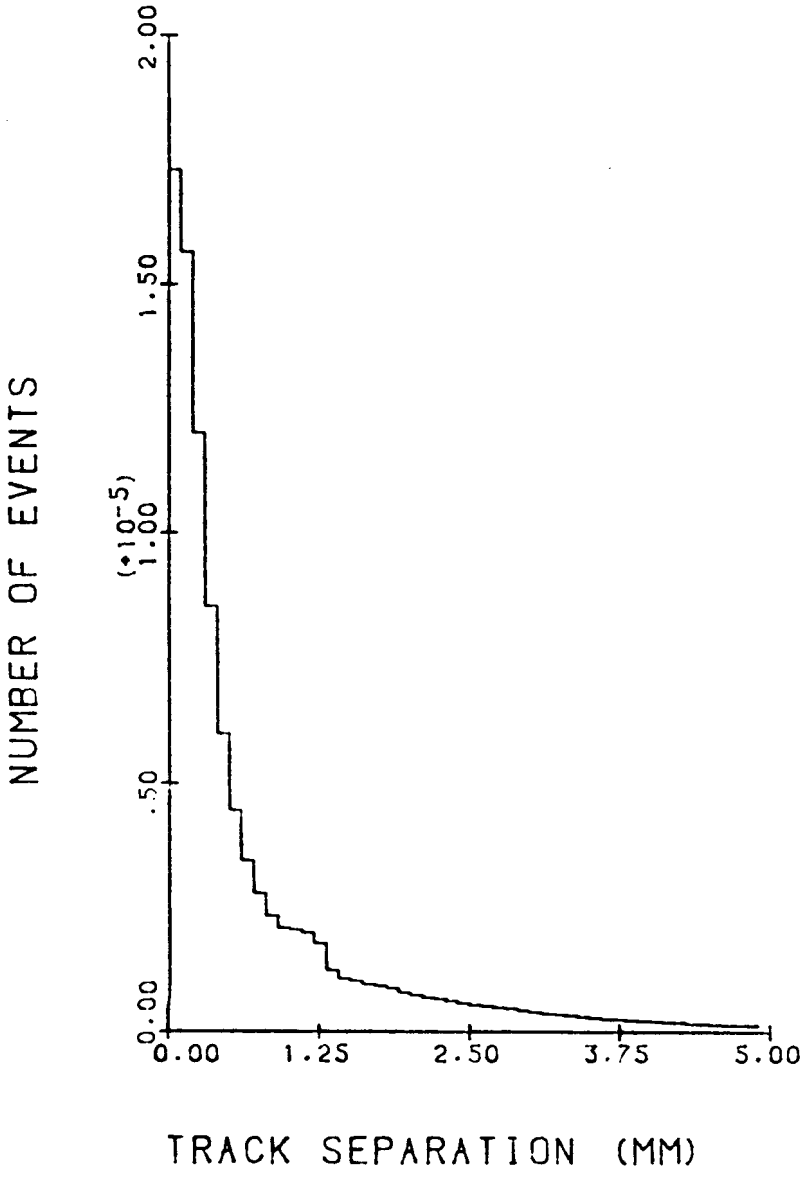


Figure 14. The distribution in the distance of closest approach of the tracks at the vertex for EE triggers.

Table 6. Requirements for General Classes

| | Foil class | Beam class |
|---|---|---|
| vertex (V) | $\lvert V-457.19 \rvert < 21$ cm | $\lvert V-457.19 \rvert > 14$ cm |
| distance of closest approach (DCA) | DCA < 6 mm | ——— |
| maximum separation in side view (S) | S < 3.4 cm | S > 1.3 cm |

combined to determine the momentum and trajectory of the neutral parent from which it was assumed they originated. MAGV would have had no effect upon this trajectory. The intersection of this parent particle trajectory and the pyramid of the beam was then determined, with the position of the assumed decay point located midway between the point where the line entered the beam and where it exited (see figure 15). A few percent of the events never intersected the beam. This was noted and an alternate decay point found by determining the position of closest approach between the line of the parent particle and the center line of the beam. A plot of the horizontal transverse vertex position determined in the second manner is given in figure 16 for $e^+e^-$ events from a central portion of the decay region. The size of the beam is also shown. A foil event was defined to have a good vertex if either this transverse vertex fell within the beam or the line intersected the beam.

Particles from beam type events were tracked through both MAGH and MAGV. A vertex was then determined. The location of this vertex and the SIZE (defined as (distance of closest approach)/(distance of vertex from MWPC1)) are given in figures 17 and 18 for KMU3 triggers. A beam event had a good vertex if the vertex location was within the beam and the SIZE was less than 0.0015.

With the vertex location known, it was possible to calculate all necessary kinematical quantities for both event classes.

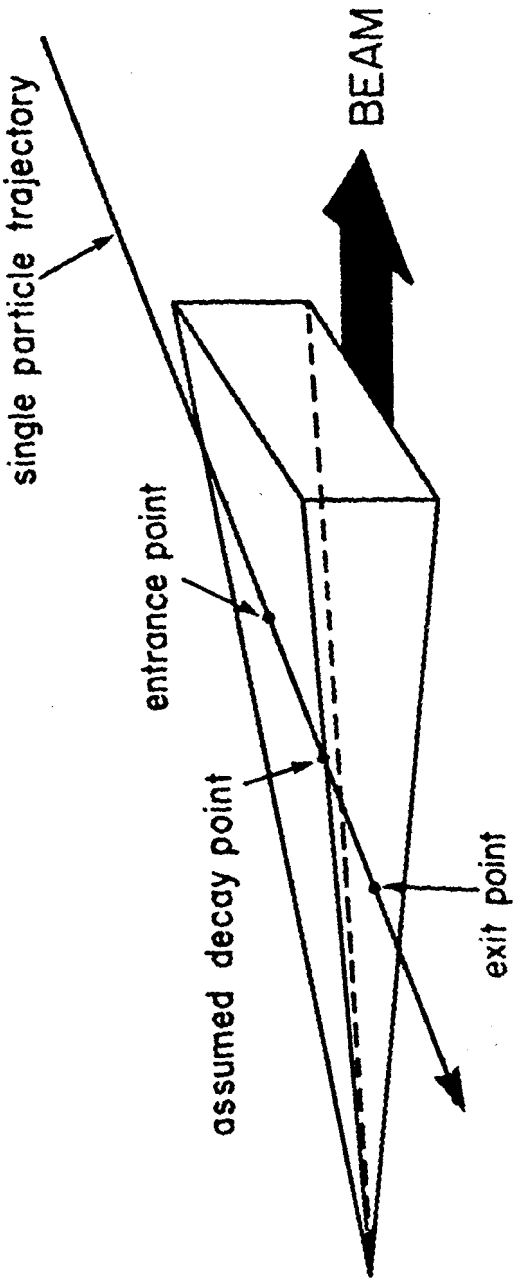


Figure 15. The technique used to track single particles to a decay point within the beam.

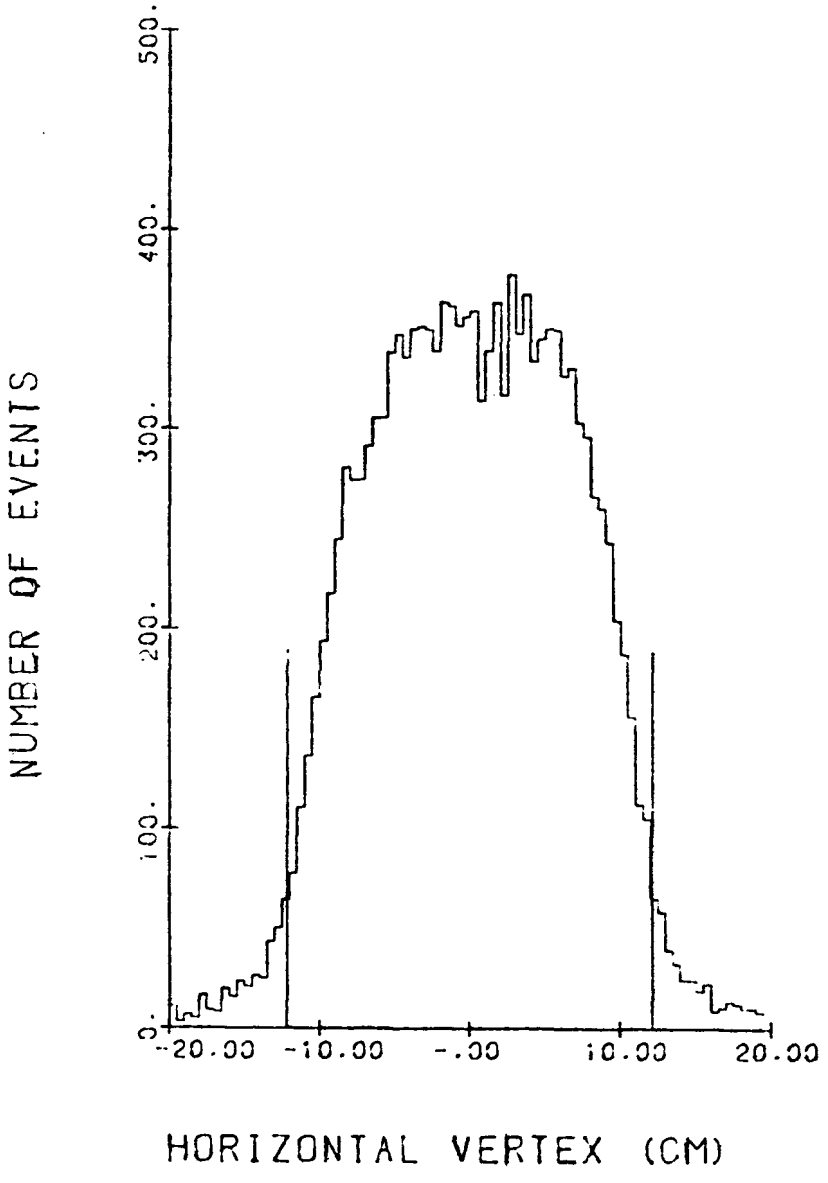


Figure 16. The distribution of the horizontal distance of projected tracks from the beam center for gamma events whose decay point lay between 390 m and 410 m. The lines indicate the beam width in this region.

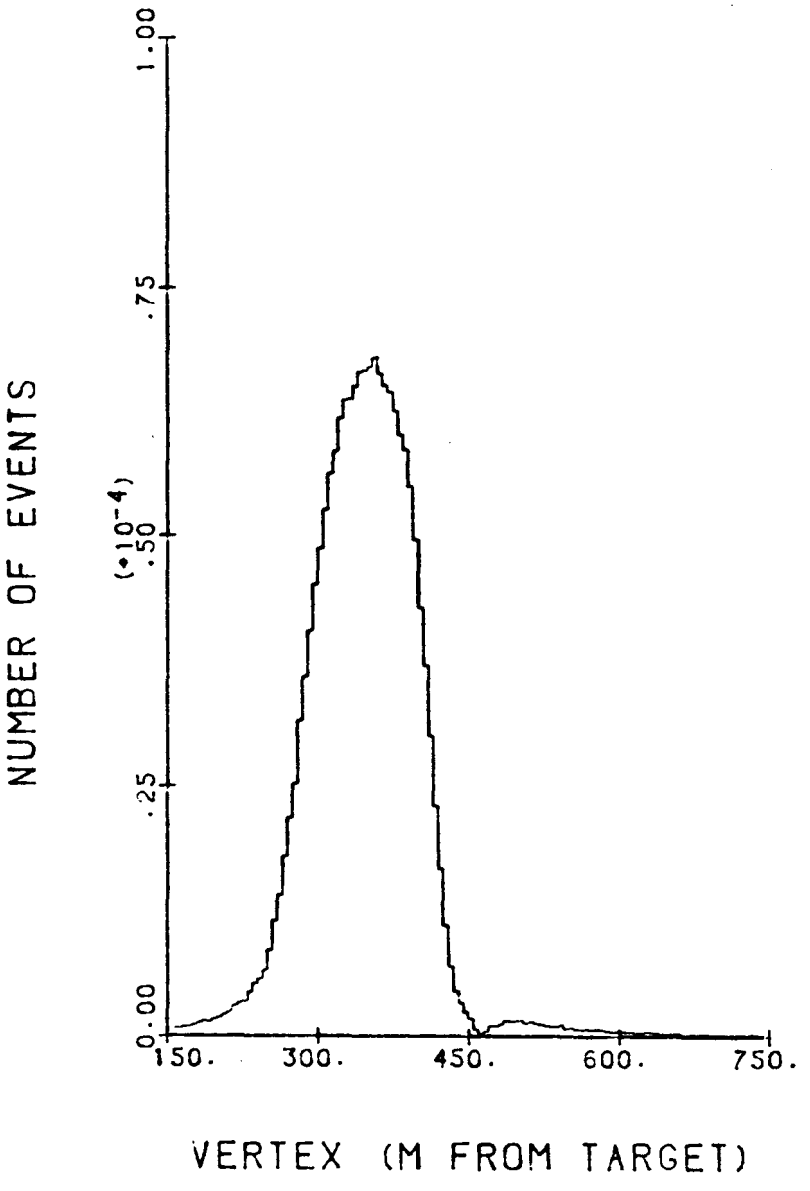


Figure 17. The longitudinal vertex distribution for KMU3 triggers.

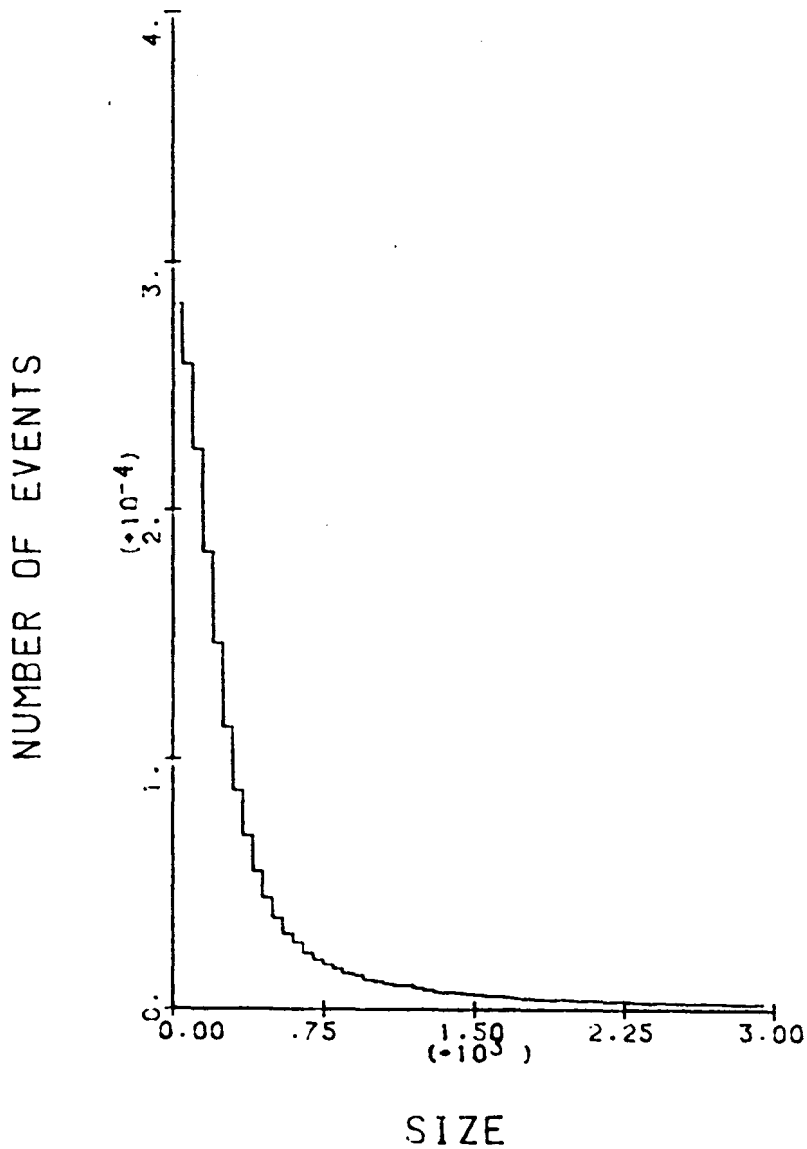


Figure 18. The SIZE distribution for KMU3 triggers.

The $p_t$ was found by:

$$p_t = (p^2 - (\vec{p}\cdot n)^2)^{\frac{1}{2}}$$

where $\vec{p} = \vec{p}_\pi + \vec{p}_\mu$ and n was the $K_L$ direction. Due to the missing neutral, there was a two fold ambiguity in determining the $K_L$ momentum for $\pi$-$\mu$ events. Accordingly, the average of the two solutions and a quantity ARG were calculated by:

$$p_K = \frac{(p_+ + p_-)}{2}$$

$$p_\pm = (1 \pm \sqrt{ARG}) \left(\frac{(\vec{p}\cdot n)\ X}{2\ (E^2 - (\vec{p}\cdot n)^2}\right)$$

$$E = E_\pi + E_\mu$$

$$X = M_K{}^2 - \vec{p}^{\,2} + E^2$$

and

$$ARG = 1 - \frac{((\vec{p}\cdot n)^2 - E^2)\ (X^2 - 4E^2\ m_K{}^2)}{(\vec{p}\cdot n)^2\ X^2}$$

All events were initially subjected to the following requirements. First, the counter latch information was checked to determine if it agreed with the trigger. Less than 1% of the events failed this requirement and they were then removed from the event set. Next, all trajectories were projected to the vacuum window and all MWPC's and counter banks. Those which lay outside the bounds of these apertures were eliminated. Finally, all particles were required to have a momentum between 5 and 200 GeV/c.

## 2. Pi-Mu Atoms

Pi-mu atoms were isolated by looking at events with the following characteristics:

1. ATOM trigger
2. Foil event topology
3. Unambiguous muon identification
4. $\pi$-$\mu$ shower counter requirement (Table 5)
5. Particles of opposite sign

The $FRAC_{total}$ for these events before imposing the shower counter requirement is shown in figure 19. A clean separation between a dominant $e^+e^-$ signal (seen in the peak around 1.0) and $\pi$-$\mu$ events is seen. These $e^+e^-$ events were due to normal gamma conversions with a randum MU counter struck. The quantity $\alpha$, defined as

$$\alpha = \frac{(p_\pi - p_\mu)}{(p_\pi + p_\mu)}$$

was then histogrammed for these events (figure 20a). For particles with identical velocities, $\alpha$ became only a function of the masses, equal to 0.14 for atoms. Figure 20a shows a clear pi-mu atom signal centered at 0.14. There is also another peak at -0.14 with 3% of the events seen at 0.14. These are events in which the pion and muon assignment were reversed.

The primary source of background was "broken" $K_{\mu 3}$'s. These

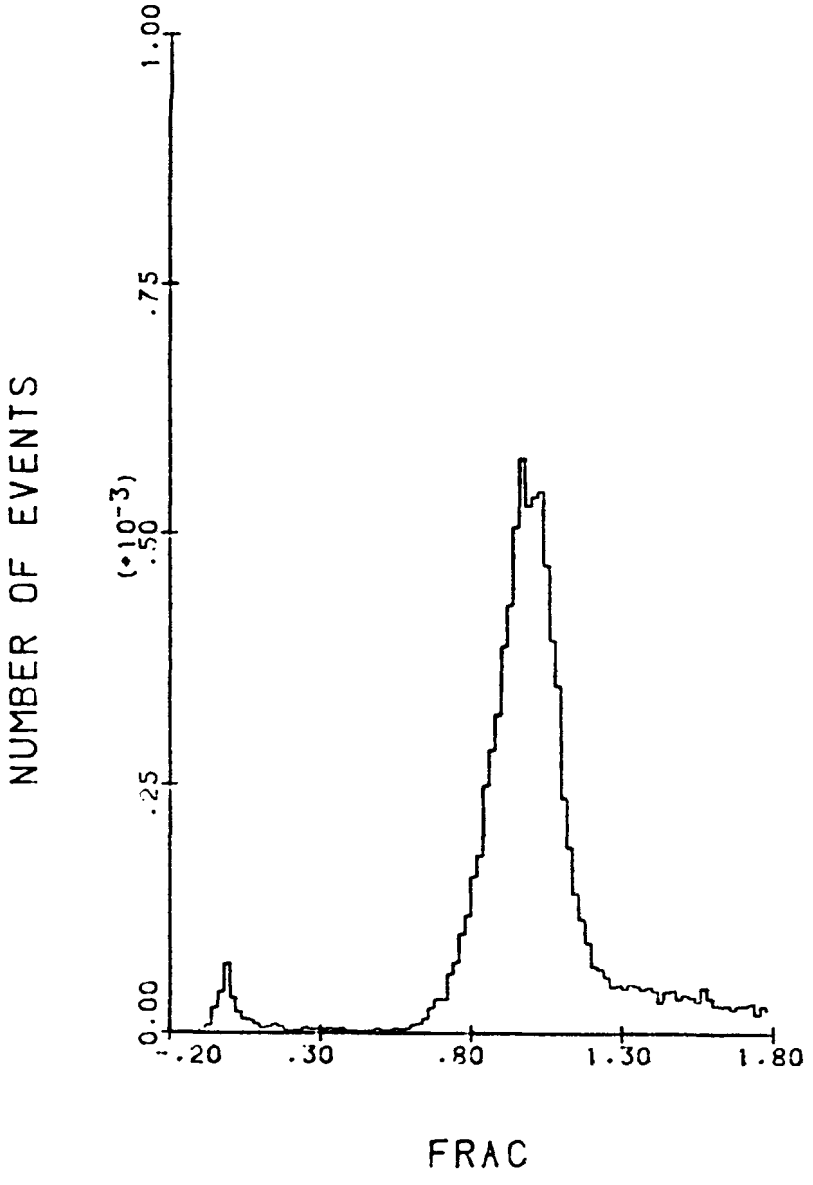


Figure 19. The $FRAC_{total}$ distribution for pi-mu atom candidates.

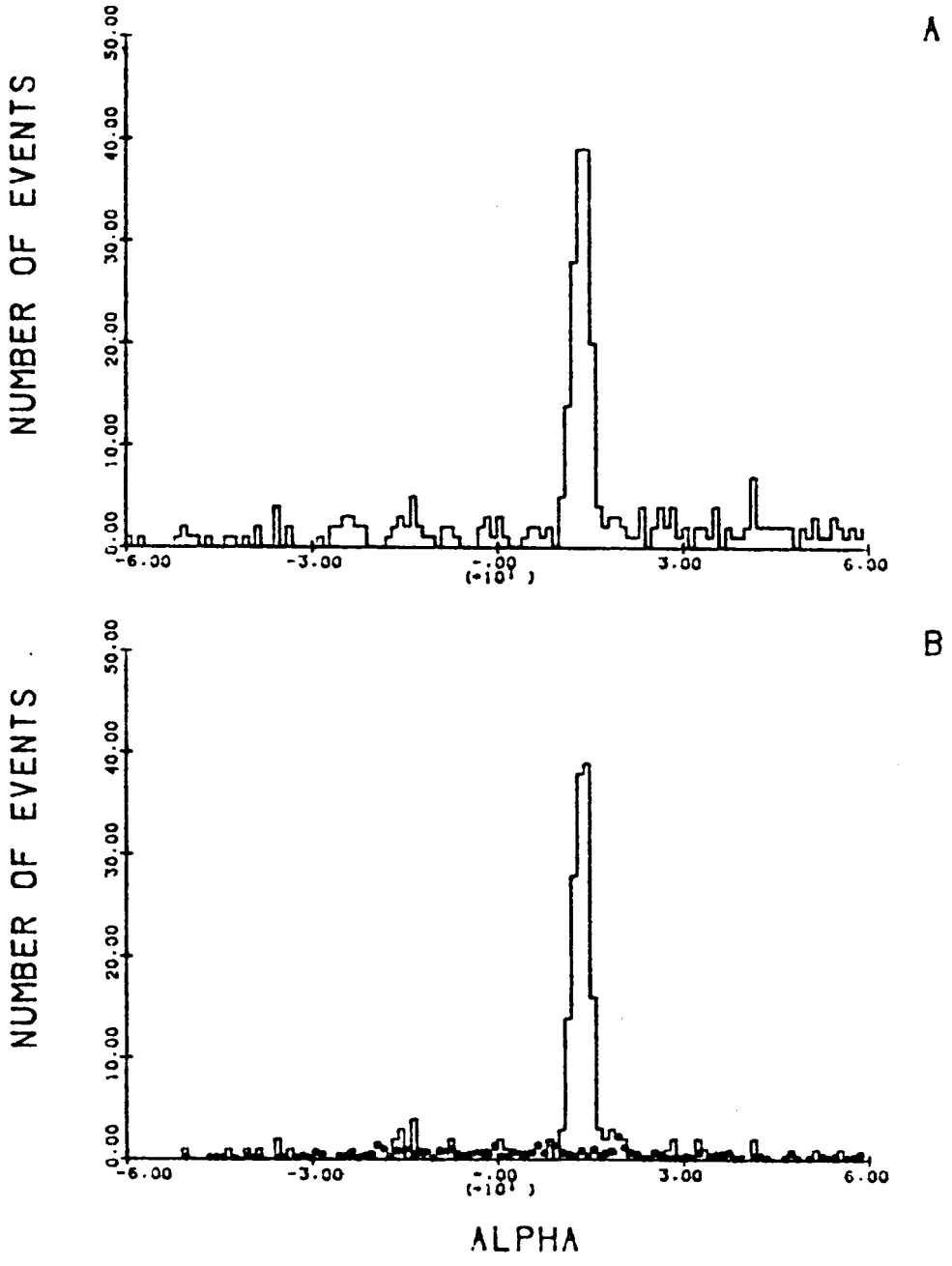


Figure 20. The distribution in the variable α for pi-mu atom candidates before (A) and after (B) imposing vertex and $p_t$ requirements. The dots are the α distribution for the simulated background.

were events in which, due to inefficiencies in the side view wire planes, only one side view track was found. Evidence for a second track could be seen in most of these events. This background was simulated by using $K_{\mu 3}$ events from the data and disregarding one of the side view tracks. Due to a combination of missing one of the tracks and not taking into account the effect of MAGV, these background events had vertex characteristics and kinematic distributions different from atoms. Figure 21a shows the $p_t$ distribution for events in 20a. The background is seen as an excess of events at higher and lower $p_t$. A plot of the simulated background in figure 20b shows the same effect. The following requirements removed most of the atom background:

1. $p_t < .210$ GeV/c
2. Good vertex

Figure 20b shows the $\alpha$ distribution for these events after all requirements.

The simulated background was passed through the atom requirements and the $\alpha$ for these events is also shown in figure 20b. The remnant pi-mu atom background outside the peaks fitted this shape well and the resultant background subtraction using the simulated shape to extrapolate underneath the peaks gave 140 ± 12 pi-mu atoms with 6 ± 2 background events. Of these atoms, 75 were $\pi^+\mu^-$ atoms and 65 $\pi^-\mu^+$.

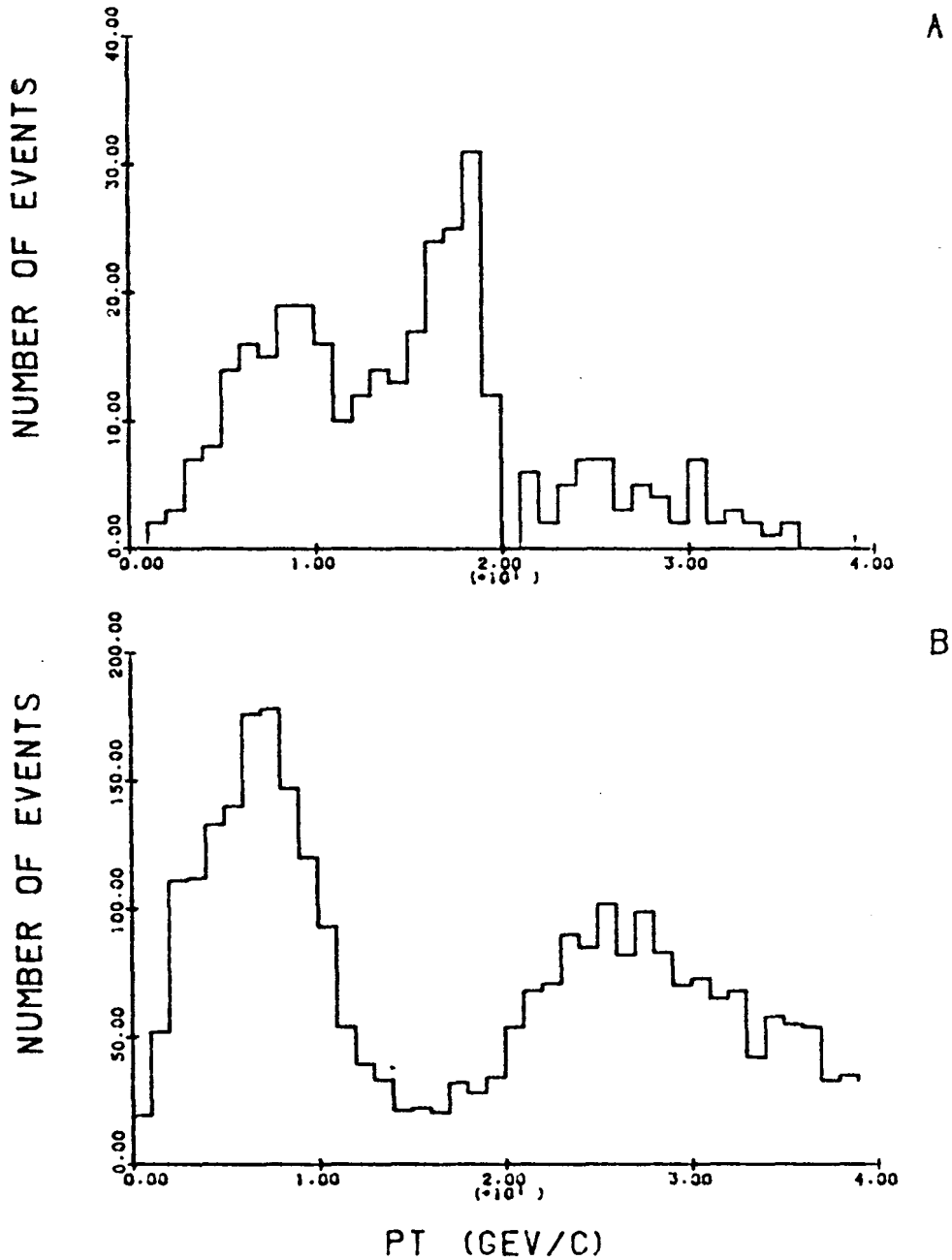


Figure 21. The $p_t$ distribution for pi-mu atom candidates (A) and the simulated background (B) before imposing vertex and $p_t$ requirements.

By relaxing the requirements imposed on atom candidates it was possible to obtain a sample of 216 pi-mu atoms with 11 background events. The requirements relaxed were the track finding, the trigger and the particle identification. Comparisons of the $p_t$, the longitudinal vertex, the atom's momentum and the atom's proper time (using as the path length the distance from the decay point to the foil) of these events to Monte Carlo generated events are given in figures 22-25. All of the distributions are statistically indistinguishable from the Monte Carlo. The lifetime distribution is discussed further in Section XI.

### 3. $K_{\mu 3}$'s

$K_{\mu 3}$'s were selected by initially requiring the following:

1. KMU3 trigger
2. Beam event topology
3. Unambiguous muon identification
4. $\pi$-$\mu$ shower counter requirement
5. Particles of opposite sign
6. Good vertex
7. 90 MeV/c $< p_t <$ 195 MeV/c

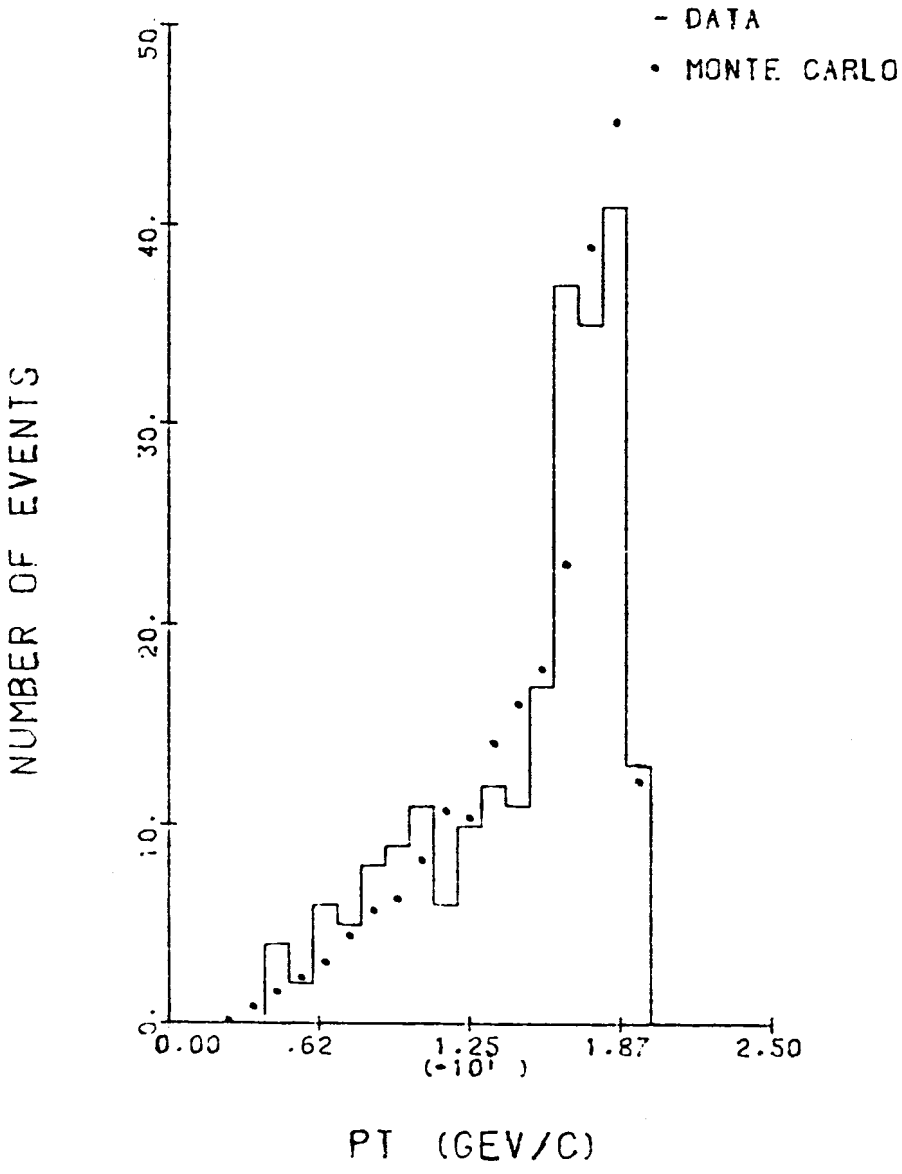


Figure 22. Comparison of data to the Monte Carlo prediction for the $p_t$ distribution of pi-mu atoms.

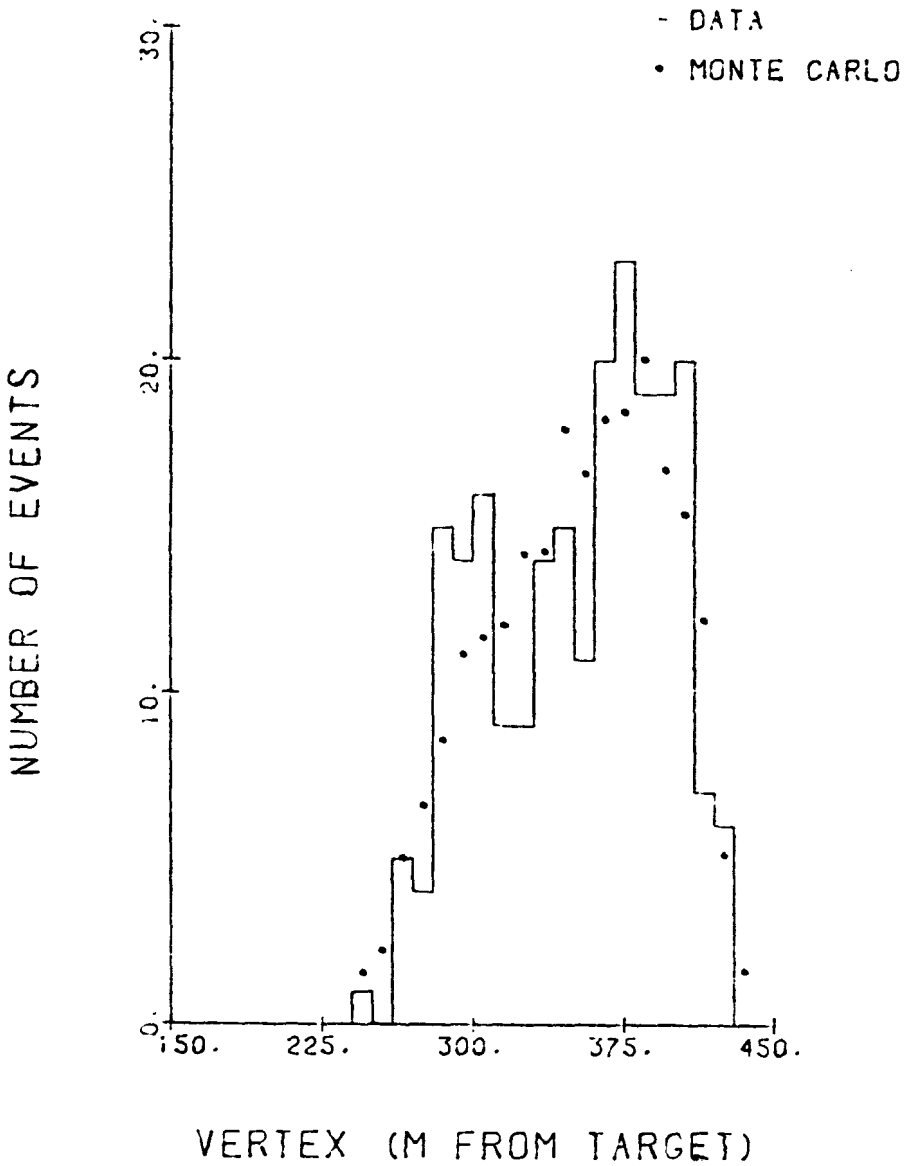


Figure 23. Comparison of data to the Monte Carlo prediction for the longitudinal vertex distribution of pi-mu atoms.

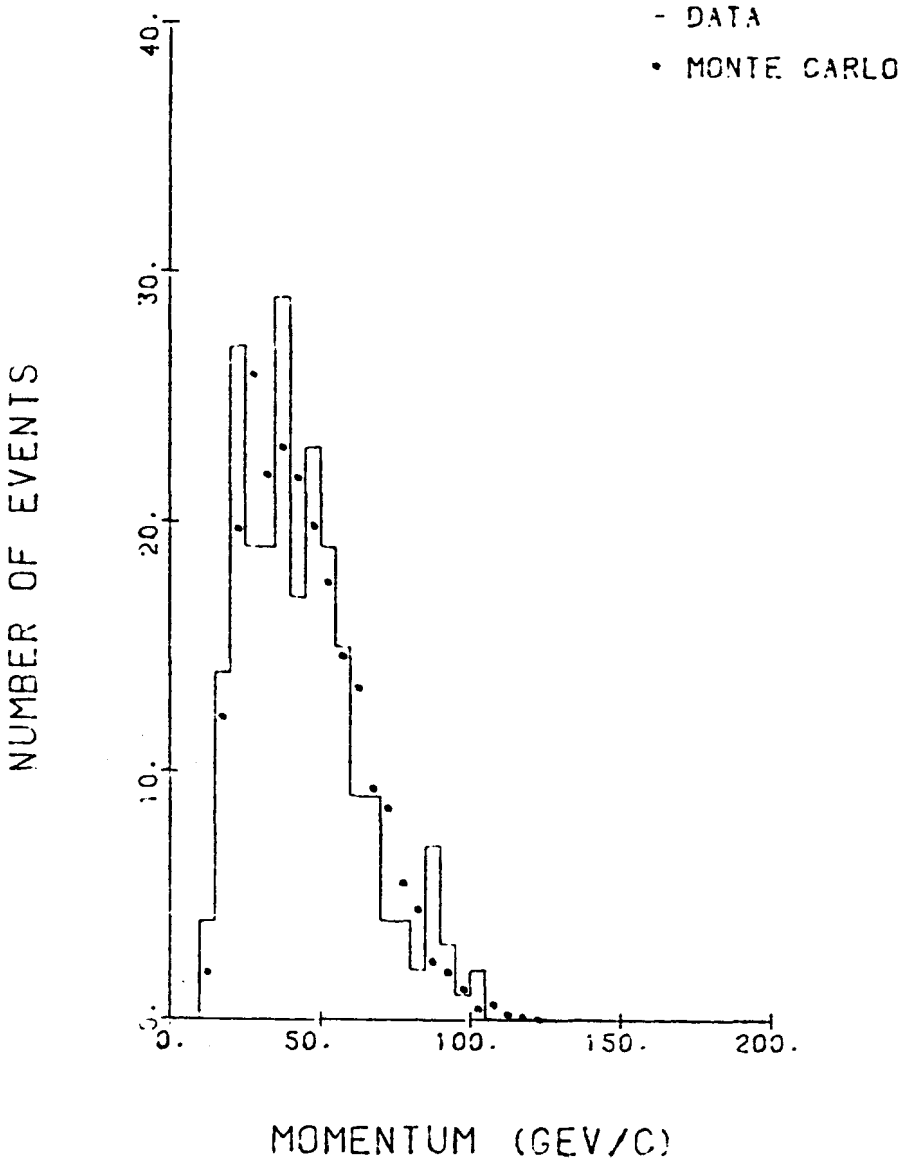


Figure 24. Comparison of data to the Monte Carlo prediction for the momentum distribution of pi-mu atoms.

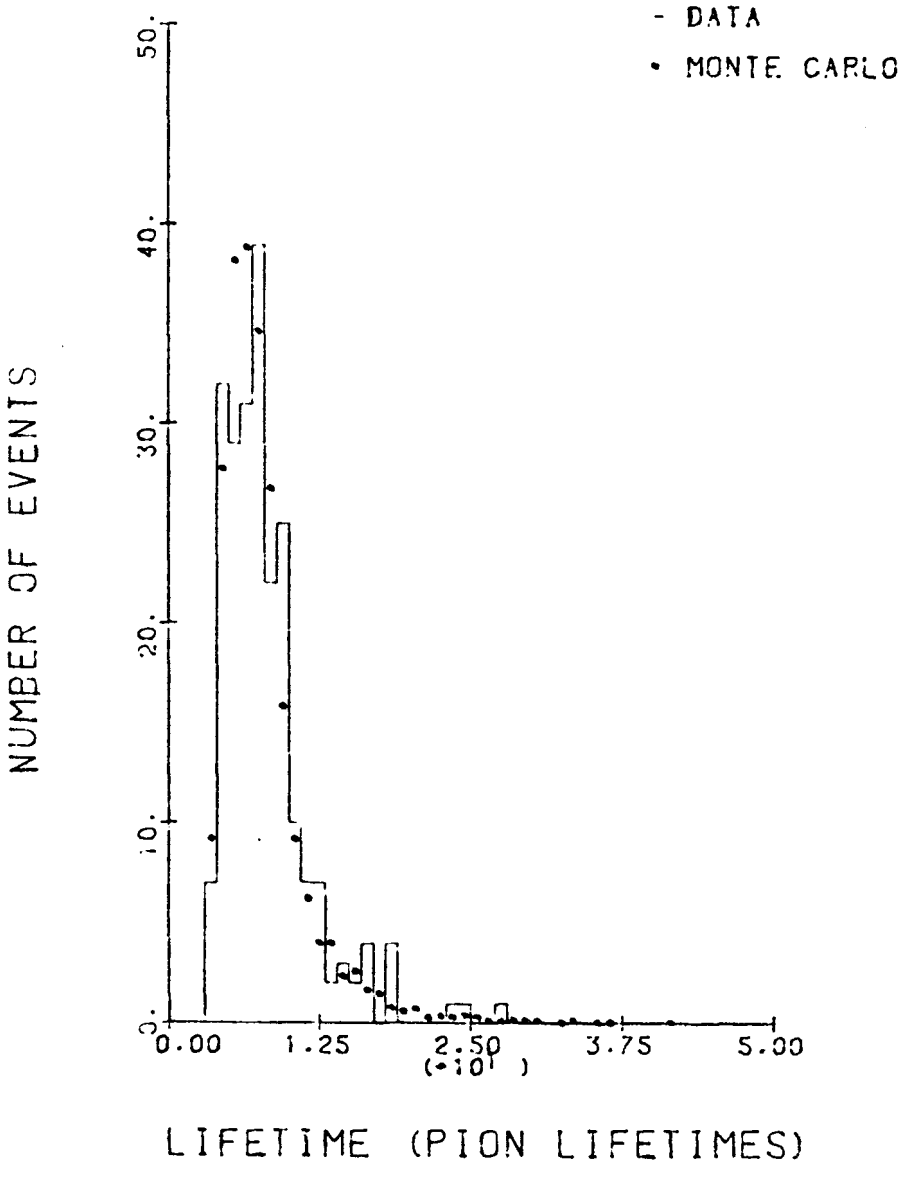


Figure 25. Comparison of data to the Monte Carlo prediction for the proper time of pi-mu atoms.

In addition, a quantity $p_o'^2$, defined as

$$p_o'^2 = \frac{(m_K^2 - m_\pm^2 - m_{\pi^o}^2)^2 - 4\ (m_\pm^2 m_{\pi^o}^2 + m_K^2\ p_t^2)}{4\ (p_t^2 + m_\pm^2)}$$

where $m_\pm$ represents the invariant mass of the two charged particles assuming each were pions, was required to be between -0.047 and -0.002.[31] This aided in eliminating $K_{\pi 3}$ events. The horizontal transverse vertex distribution of these events before vertex requirements along with the beam size for events from the central region of the decay volume is shown in figure 26. In addition, the longitudinal vertex and measured $K_L^o$ momentum distributions are given in figures 27 and 28.

These $K_{\mu 3}$ events were used to normalize the pi-mu atom events and to verify the Monte Carlo calculation. These events will be discussed in greater detail in Section VIII.

### 4. Gamma Events

Converted gamma events were selected by the following requirements:

1. EE trigger
2. Foil event topology
3. e-e shower counter requirement
4. Particles of opposite sign

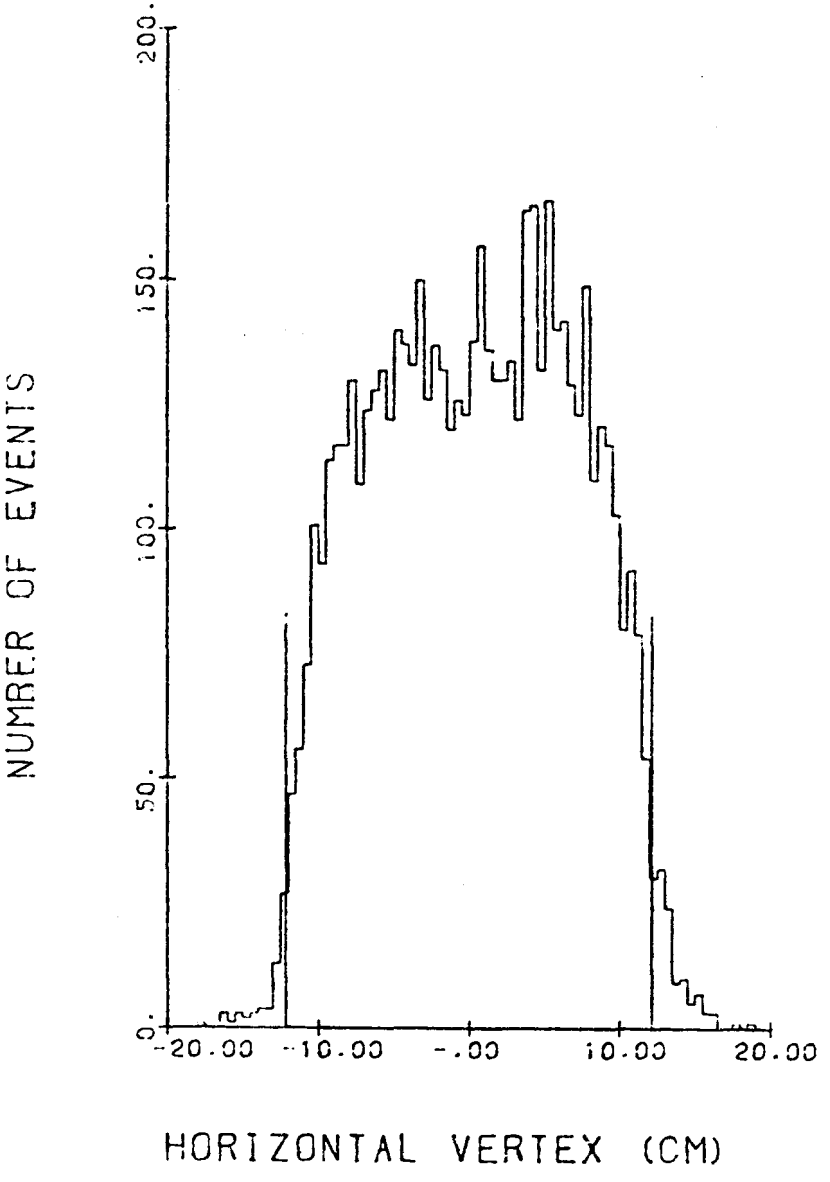


Figure 26. The distribution in the horizontal distance of the vertex from the beam center for $K_{\mu 3}$ events whose longitudinal vertex lay between 390 m and 410 m. The lines indicate the beam width in this region.

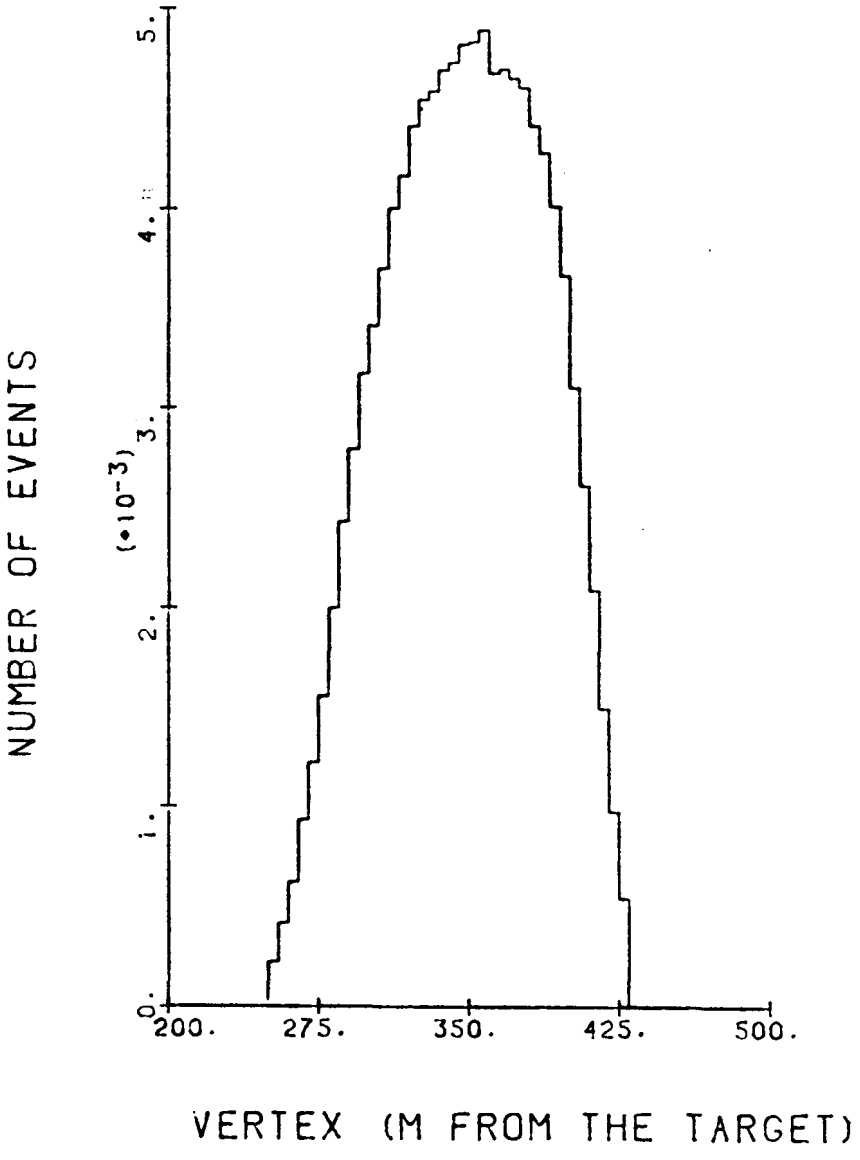


Figure 27. The longitudinal vertex distribution for $K_{\mu 3}$ events.

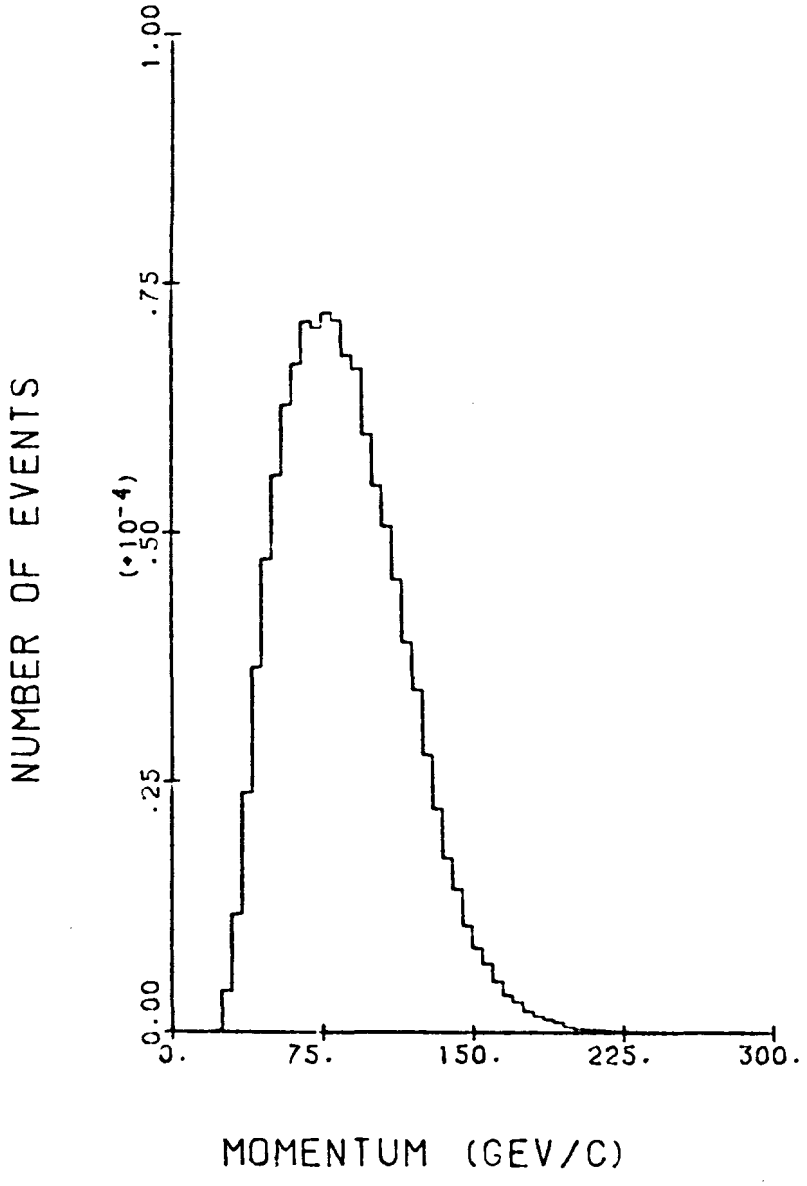


Figure 28. The $K_L^0$ momentum distribution for $K_{\mu 3}$ events.

5. Good vertex

The $p_t$ of these events is shown in figure 29. There are three main regions. Below 137 MeV/c, events from $K_L^o \to 3\pi$ dominate. Between 137 and 250 MeV/c there exists a shelf due to $K_L^o \to \pi^o\pi^o$ and $K_L^o \to \gamma\gamma$. The region above 250 MeV/c is due to $\pi^o$'s produced in neutron interactions in the residual gas in the decay tank. The relevant $p_t$ distribution for the $\gamma\gamma$ mode and the result of a Monte Carlo calculation are also shown. The shape of the region above 250 MeV/c was determined using data collected with a vacuum in the decay region ranging from 900 to 2000 microns compared to the normal condition of 12 microns. Details of this calculation, of background subtraction and of the extraction of the number of events in each mode are described in reference 16.

## 5. $K_{e3}$'s

$K_{e3}$ events were used in shower counter studies (Section VII-B). They were selected by the following requirements:

1. EE trigger
2. Beam event topology
3. Particles of opposite sign
4. Good vertex

In addition, $p_o'^2$ was required to be less than -0.025. This eliminated $K_{\pi 3}$ events.

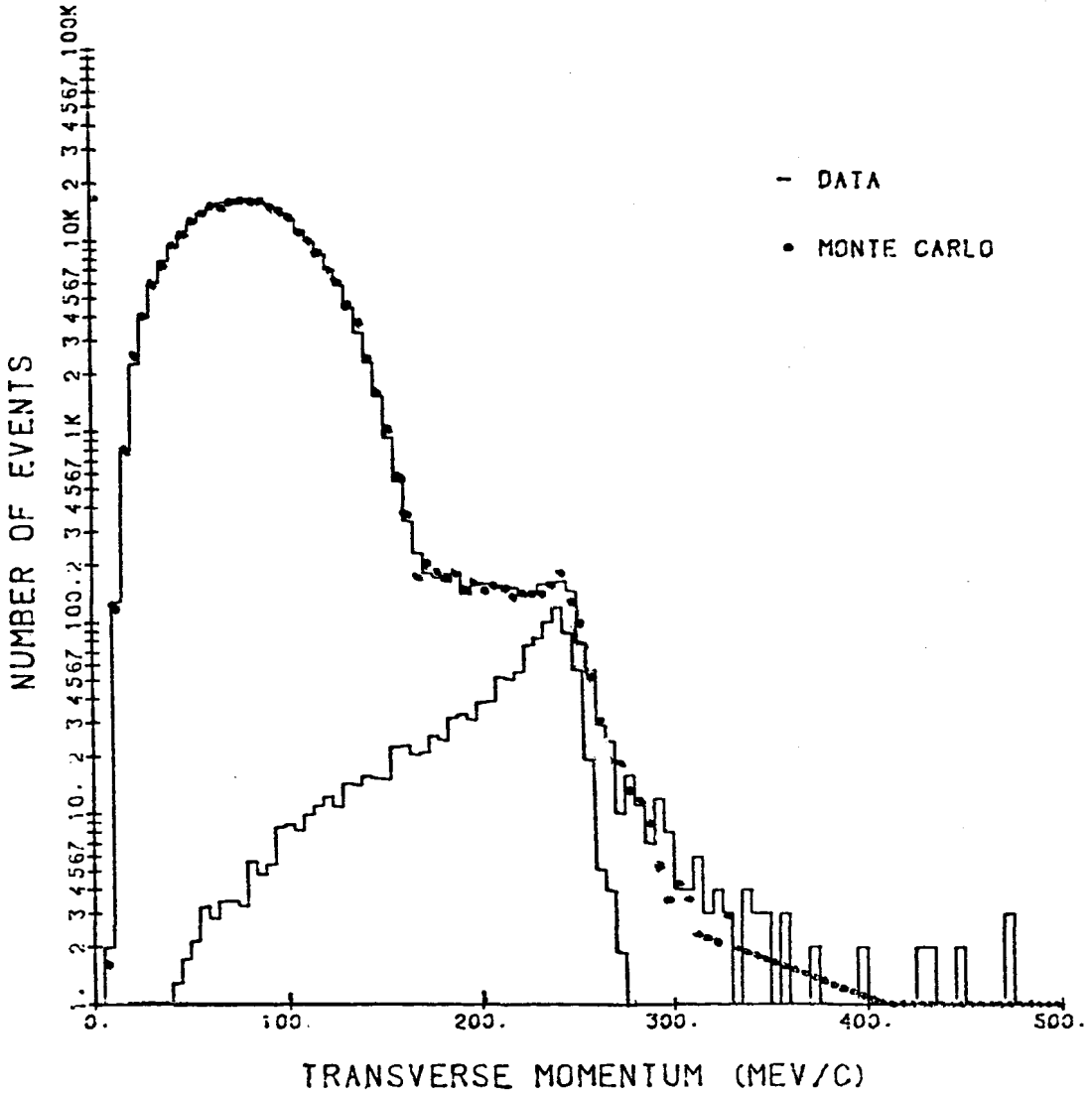


Figure 29. The $p_t$ distribution for gamma events. The dots are the result of a fit using Monte Carlo and calibration data. Also shown is the $p_t$ distribution for Monte Carlo generated $K_L^o \rightarrow \gamma\gamma$ events (shifted downward from its proper normalization).

## VIII. $K_{\mu 3}$ Background

There were two main sources of $K_{\mu 3}$ background. The first was due to other $K_L^o$ decays such as $K_{\pi 3}$ and $K_{e3}$ with a subsequent pion decay. The average path lengths of the pions was about 20% of a pion lifetime. Due to the different Q of these reactions, the requirements on $p_t$ and $p_o'^2$ for $K_{\mu 3}$ events lowered the $K_{\pi 3}$ and $K_{e3}$ contributions by 70% and 28% respectively. The calculation of the size of this background was done by Monte Carlo using the known branching ratios for these modes. This calculation gave a background contribution of 0.76% from $K_{\pi 3}$'s and, assuming 2.7% of e-μ events were misidentified as π-μ events, 0.07% from $K_{e3}$'s.

The second source of $K_{\mu 3}$ background was two random tracks from different $K_L^o$ decays being combined together into an assumed single decay and also neutrons in the beam halo and $K_L^o$ decay products interacting in the beam pipe. (The radius of the beam pipe increased from 15.2 cm to 45.7 cm at 321 m. This, plus the settled pipe at 280 m (figure 3), was the source of the events in the 310 m region seen in figures 30-33.) As both of these sources did not come from a single $K_L^o$ decay, they can be considered as "non-beam" background. Four techniques, described below, gave similar estimates of the non-beam background contribution.

The weighted average was then used and gave a non-beam contribution of (4.36 ± 0.73)%.

Figures 30a-33a give the longitudinal vertex distribution for the four classes of events described in Table 7 (Class 1 being the $K_{\mu 3}$ class). These events have passed the first four requirements on page 69 and the distributions in figures 30b-33b are for those events which also passed the vertex requirements. Also shown is the distribution of two particles taken from separate KMU3 trigger events normalized using the region between 480 m and 550 m (the normalization was done using 30a-33a with this normalization also being used in 30b-33b). These agree for the non-$K_{\mu 3}$ classes. The first technique assumed that the effects of all $K_{\mu 3}$ requirements on the non-beam background were identical to those on these simulated events with the region between 480 m and 550 m being used to normalize to the data.

Figure 34 gives the $p_t$ distribution for opposite and like sign events following vertex requirements. The $K_{\mu 3}$ events have a kinematic cutoff at about 195 MeV/c whereas the distribution seen in 34b is smooth through this region. The distribution in any variable for those background events with a $p_t$ between 195 and 250 should be similar to those whose $p_t$ is less than 195. Any difference in a distribution's shape as a function of $p_t$ was estimated by looking at like sign events. Techniques 2-4 each used a different

Table 7. $K_{\mu 3}$ Non-Beam Background Classes

| Class |
|---|
| 1. - particles of opposite charge, $p_t < 195$ MeV/c |
| 2. - particles of opposite charge, $p_t > 195$ MeV/c |
| 3. - particles of like charge, $p_t < 195$ MeV/c |
| 4. - particles of like charge, $p_t > 195$ MeV/c |

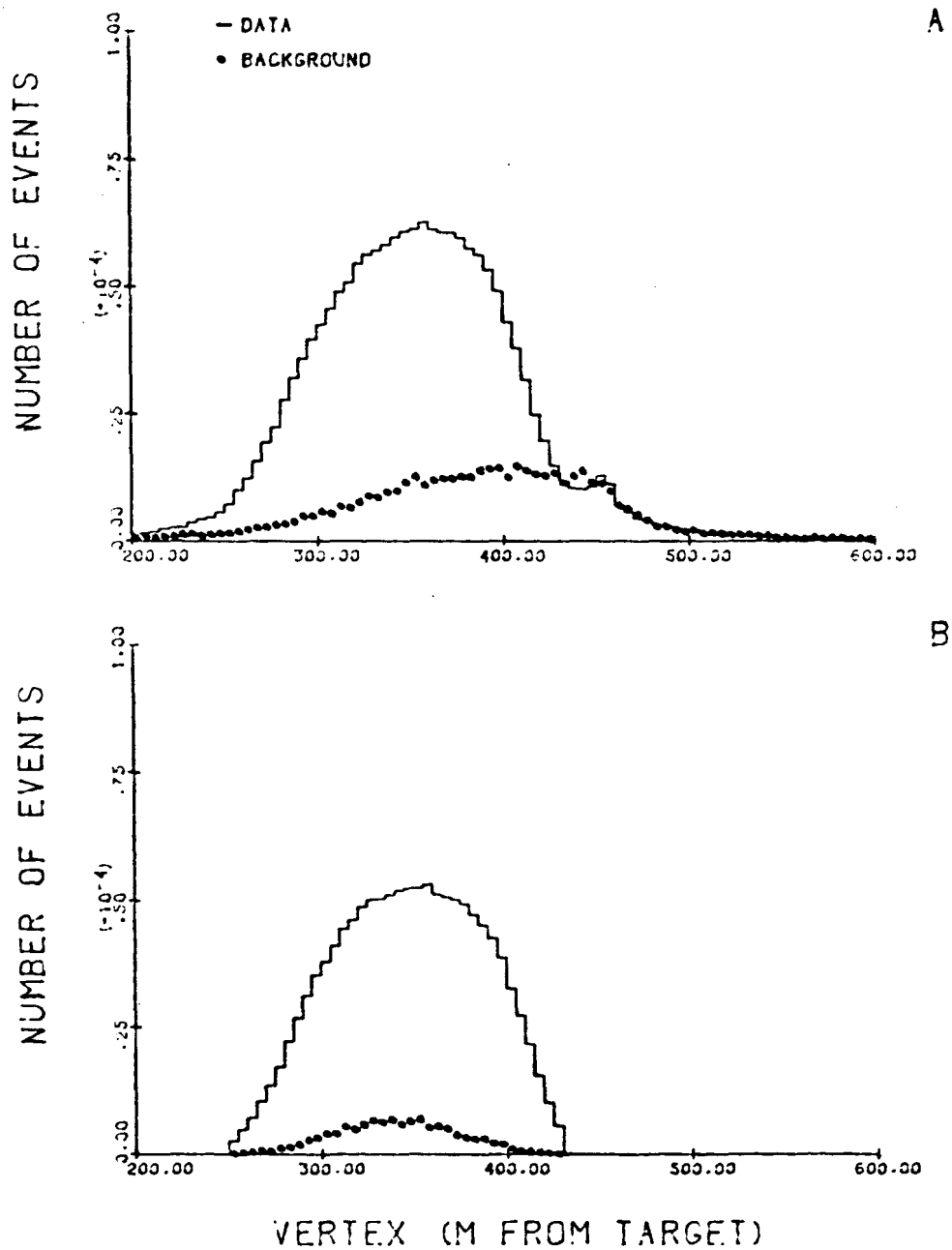


Figure 30. The longitudinal vertex distribution for Class 1 events before (A) and after (B) imposing vertex requirements. The dashed line is the simulated background normalized to the region between 480 m and 550 m in A.

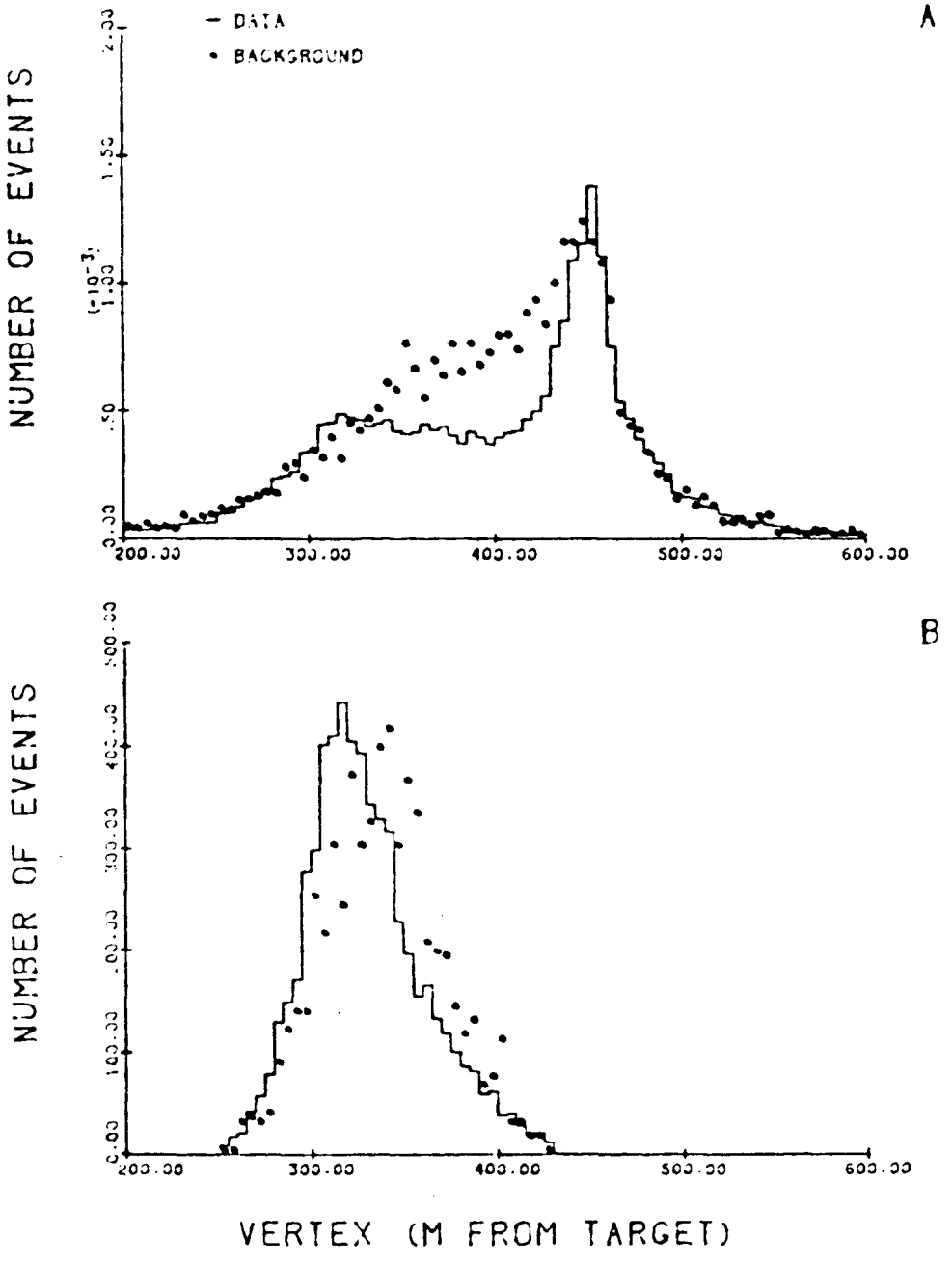


Figure 31. As in figure 30 for Class 2 events.

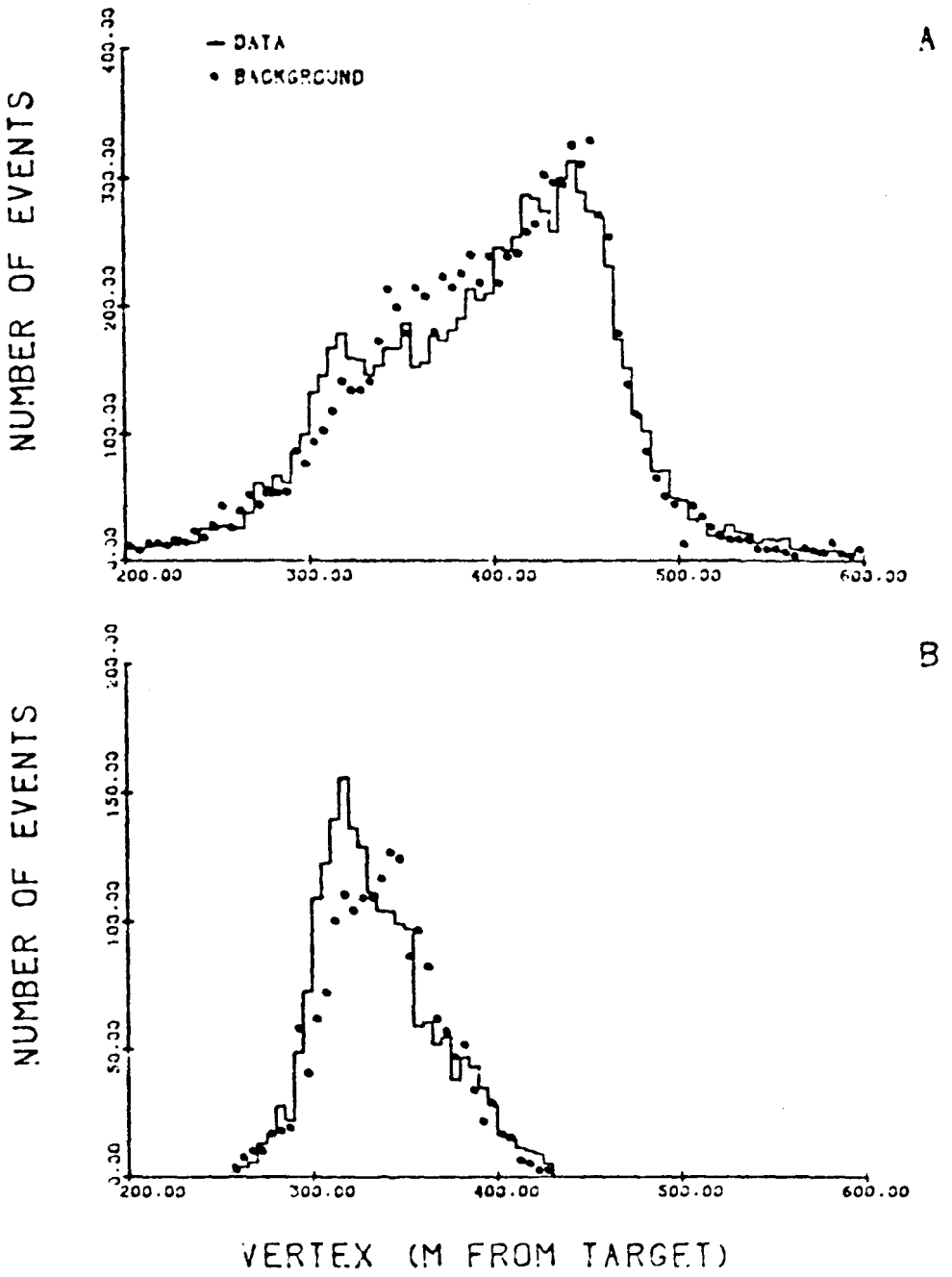


Figure 32. As in figure 30 for Class 3 events.

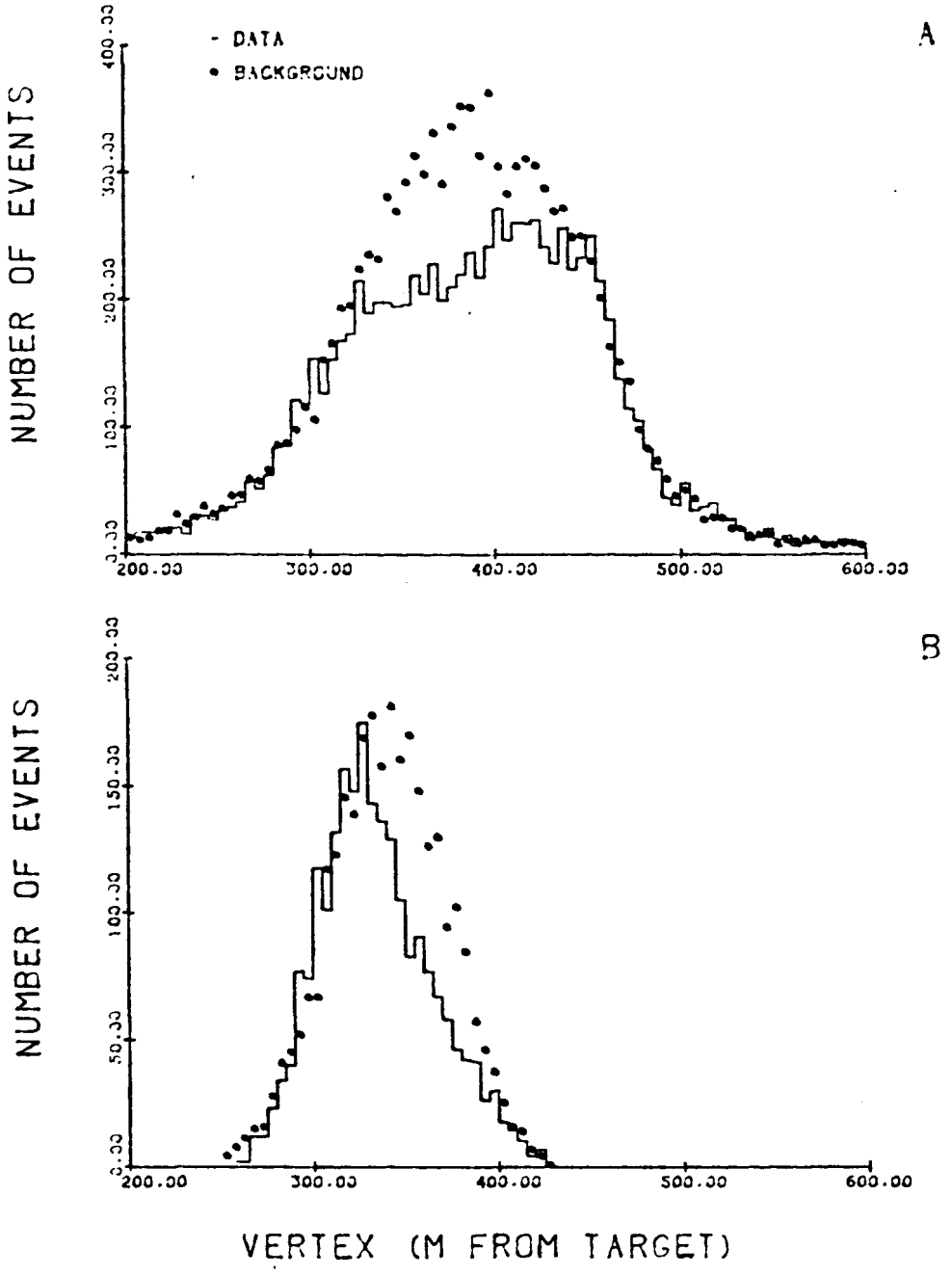


Figure 33. As in figure 30 for Class 4 events.

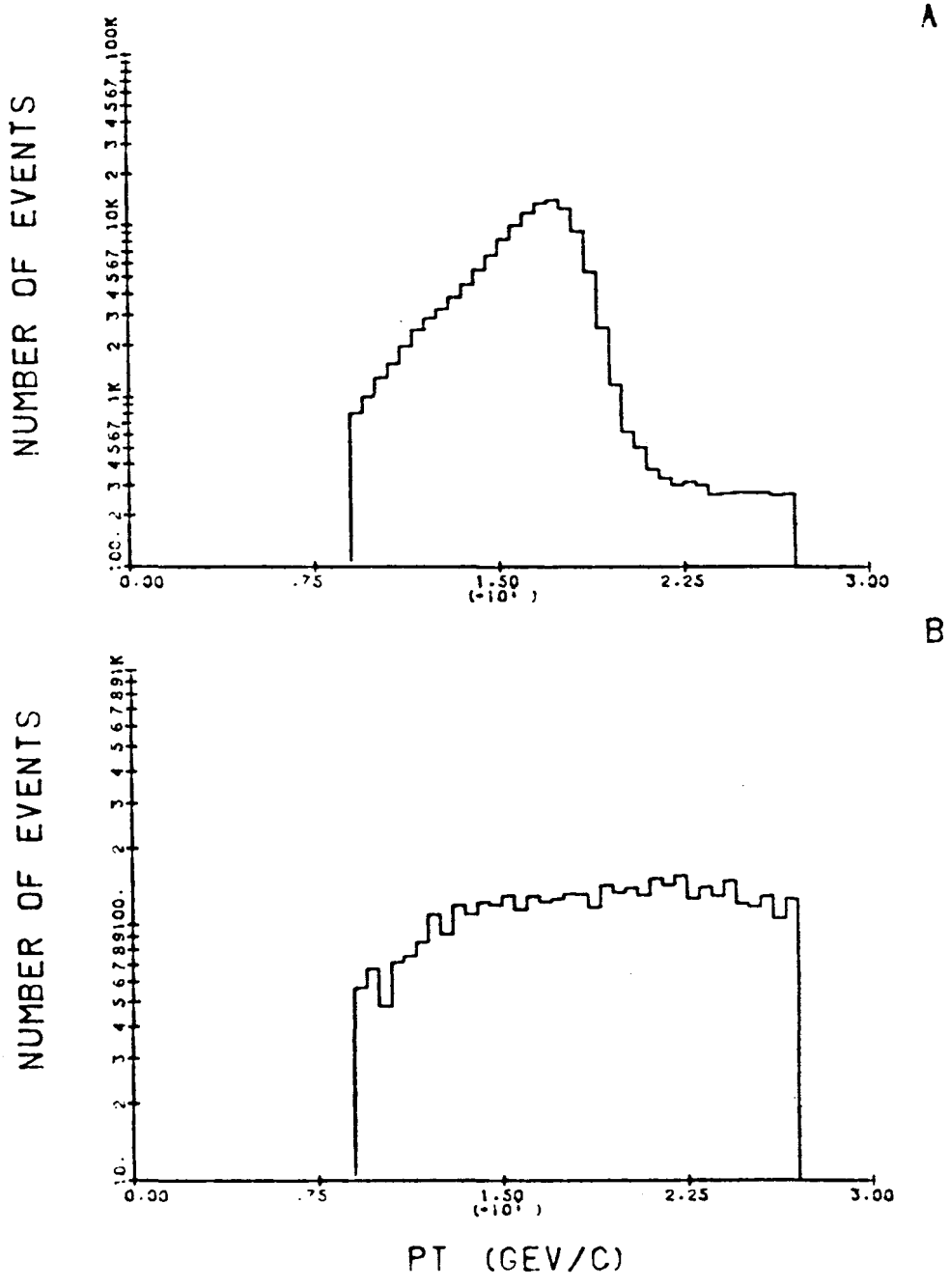


Figure 34. The $p_t$ distribution for opposite charge (A) and like charge (B) beam events.

distribution to estimate the total non-beam background. (Note: The $p_o'^2$ requirement eliminated all events with a $p_t$ greater than 210. The following calculations were done before this requirement was imposed and their results were then weighted by the effect of the $p_o'^2$ requirement on Class 3 events.)

The second technique used the $p_t$ distribution itself. It assumed that the shapes of the like and opposite sign non-beam events were the same and then extrapolated opposite sign events from $p_t$ greater than 200 underneath the $K_{\mu 3}$ signal using the like sign distribution.

The center of the beam was 2.9 cm to the beam right of the center of the pipe at 321 m. This caused an asymmetry in the horizontal transverse vertex distribution for events between 310 m and 325 m. This is seen in figure 35b for Class 2 events. By measuring the asymmetry of this distribution in Class 1 events (figure 35a) relative to the Monte Carlo and assuming the excess was due to background, the number of background events in this region was estimated. The longitudinal distribution of Class 2 events shown in figure 31b was used to extrapolate to all regions. This is the third technique.

The fourth technique assumed that the number of non-$K_{\mu 3}$ events removed from Class 1 events by the vertex requirement could be estimated using the Class 2 events. The effect of this requirement

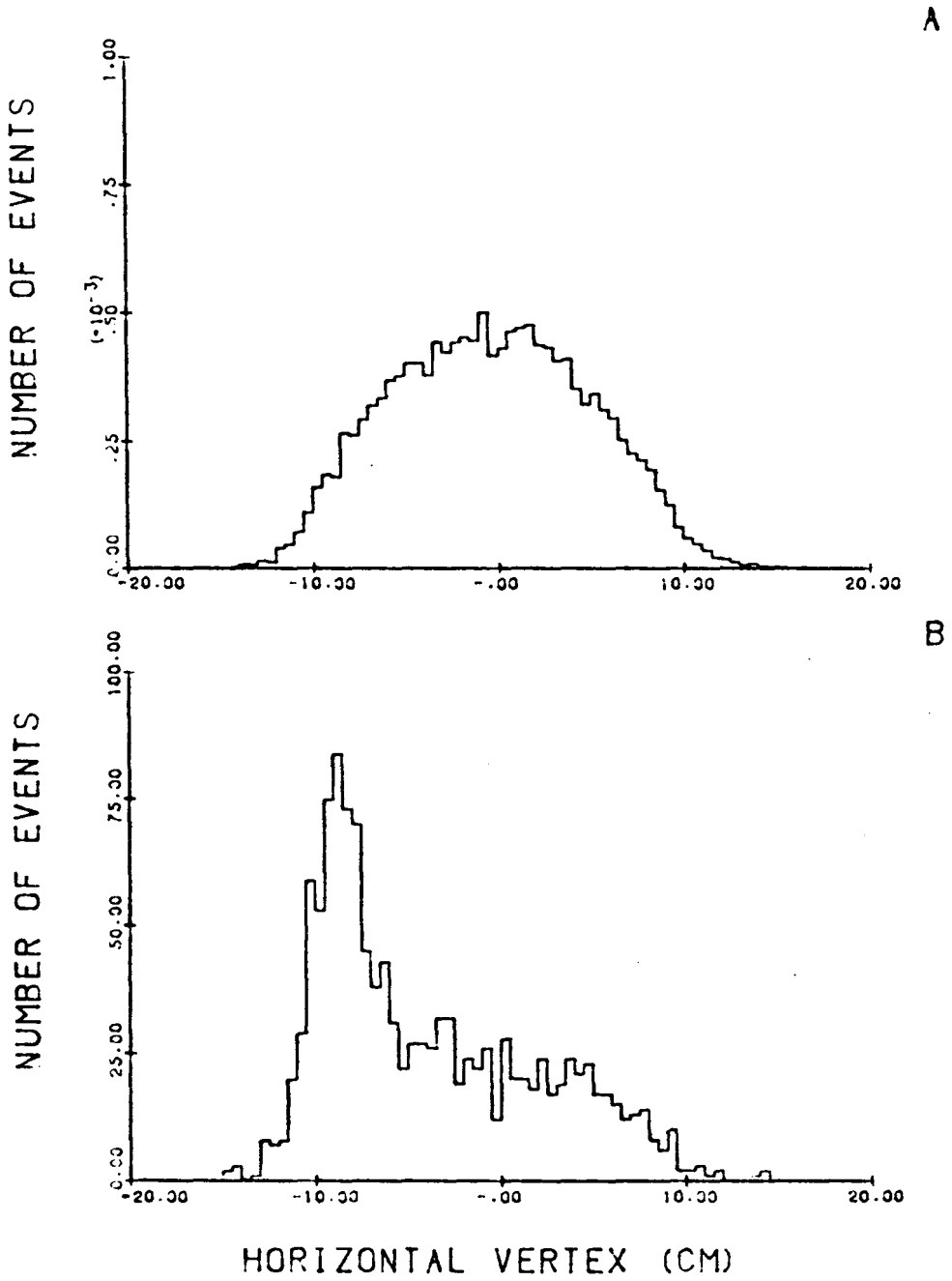


Figure 35. The distribution in the horizontal distance of the vertex from the beam center for Class 1 (A) and Class (2) events.

is seen in figures 30-33. The random track signal from 480 m to 550 m provided a means of normalizing to the Class 1 events. Quantitatively, if $BEFORE_{Cn}$ was the number of Class n events with a longitudinal vertex position between 480 m and 550 m before the requirements were imposed then the number of background events in Class 1 was equal to

$$BEFORE_{C1} \times \frac{(\text{total Class 2 after})}{BEFORE_{C2}}$$

The average of these four techniques gave a non-beam background contribution of $(4.36 \pm 0.73)\%$ where the error has been weighted by a scale factor of $(\chi^2/DF)^{\frac{1}{2}}$. This gave a total $K_{\mu 3}$ background of $(5.29 \pm 0.75)\%$. A summary of all $K_{\mu 3}$ background sources is given in Table 8.

Table 8. Sources of $K_{\mu 3}$ Background

| Source | Contribution (%) |
|---|---|
| A. $K_L^o \to \pi^+\pi^-\pi^o$ followed by $\pi \to \mu\nu$ | 0.76 ± 0.10 |
| B. $K_L^o \to \pi e\nu$ followed by $\pi \to \mu\nu$ | 0.07 ± 0.04 |
| C. Non-beam background | |
| Technique 1 - 7.48 ± 0.30<br>2 - 4.20 ± 0.18<br>3 - 3.68 ± 0.16<br>4 - 3.30 ± 0.55 | |
| Average non-beam background | 4.36 ± 0.73 |
| Total $K_{\mu 3}$ background | 5.29 ± 0.75 |

# IX. Comparison of Data to Monte Carlo

## A. Single Muons

Single muon events were used to study the resolution of the spectrometer. This study also provided chamber performance values for input to the Monte Carlo.

A miss distance, $\delta$ , in a given MWPC was defined by the difference between the projection of the line determined by the other chambers to that MWPC and the hit in the MWPC. The size of this delta depended upon the position resolution of the chambers and on the size of the multiple scattering in the apparatus. These two effects would add in quadrature. For any given chamber, $\delta$ was centered about zero and its standard deviation $\sigma$ was determined by fitting the distribution to a Gaussian shape. Figure 36 shows $(\sigma P)^2$ where P is the particle's momentum versus $P^2$ for the third module for data events. Both the data and Monte Carlo were fitted to the form $AP^2 + B$. The terms dependent on the chambers and multiple scattering (A and B respectively) and the $\chi^2$ for these fits are given in Table 9, with the Monte Carlo limits also shown in figure 36. The agreement demonstrates that the Monte Carlo correctly reproduced the position resolution of the chambers. This resolution was found to be the same for all data taking conditions and particle types.

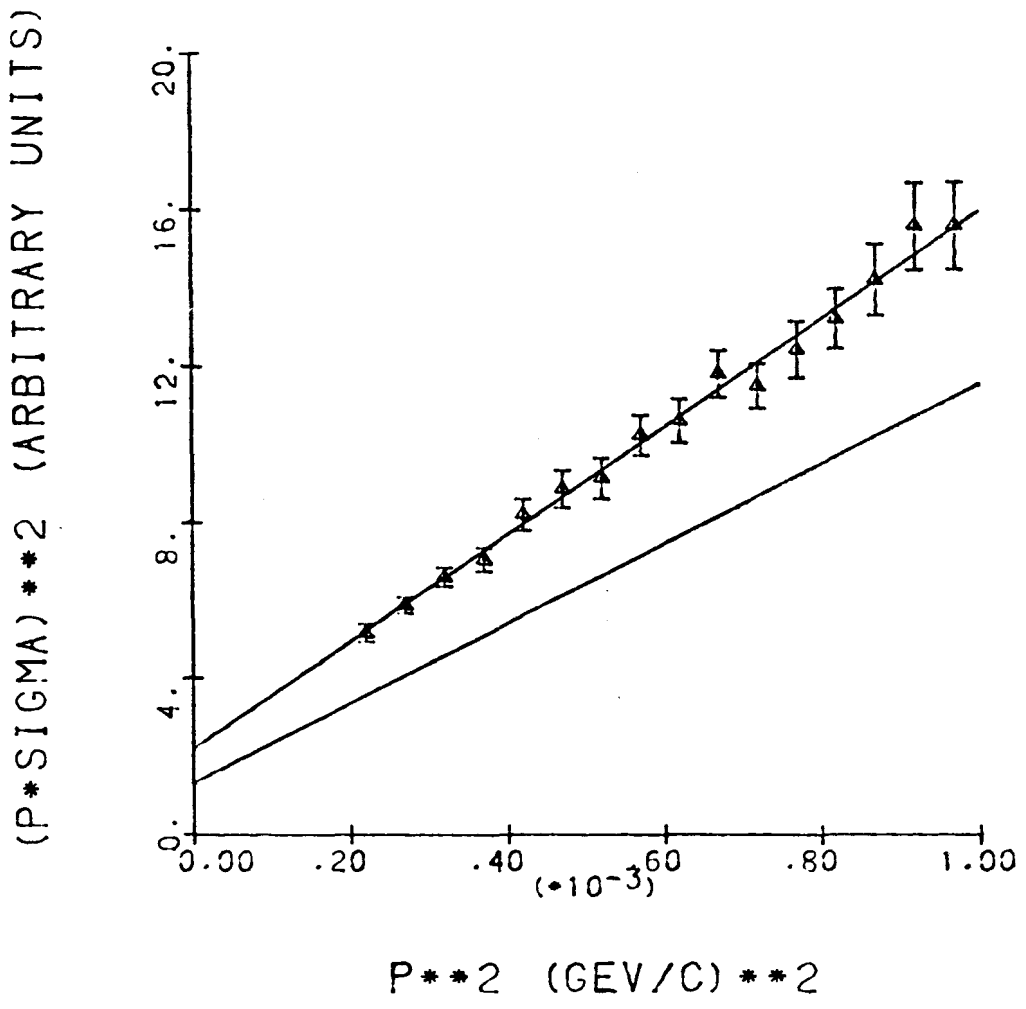


Figure 36. The square of the momentum P times the chamber position resolution $\sigma$ $(P\sigma)^2$ versus $P^2$ for wire plane 6. The lines are the limits of a Monte Carlo calculation.

Table 9. Chamber Resolution Fit Results

| | A | B | $\chi^2$/DF |
|---|---|---|---|
| Data | 2.06 ± 0.24 | 0.0138 ± 0.0006 | 3.7/14 |
| Monte Carlo | 1.77 ± 0.44 | 0.0118 ± 0.0011 | 10.0/14 |

## B. $K_{\mu 3}$'s

Comparisons between data and Monte Carlo $K_{\mu 3}$ distributions were used to determine input parameters to the Monte Carlo and then to verify the Monte Carlo calculations of the pi-mu atom and $K_{\mu 3}$ acceptances.

The ARG distribution, defined in Section VII-D, for $K_{\mu 3}$ data and Monte Carlo events is shown in figure 37. The sensitivity of this parameter is demonstrated in figure 38 where the fraction of events with $|ARG| < .01$ (unambiguous events, those whose two $K_L^o$ momentum solutions differed from their average by less than 10%) is plotted for Monte Carlo events with the position of the $K_L^o$ production target used to calculate ARG varied vertically from the position used in the Monte Carlo generation. From this sweep, the position of the target can be determined to about 1 cm. As the target is 450 m from the apparatus, this gives a sensitivity of about 20 microradians on the $K_L^o$ beam direction. This technique was used to locate the target position. Figure 39 shows the target sweep for the data compared to the Monte Carlo following the target determination. The agreement demonstrates that the quality of the magnet tune was sufficient. Though the sensitivity was less, the horizontal target position could also be found in this way. These sweeps for data and Monte Carlo are given in figure 40.

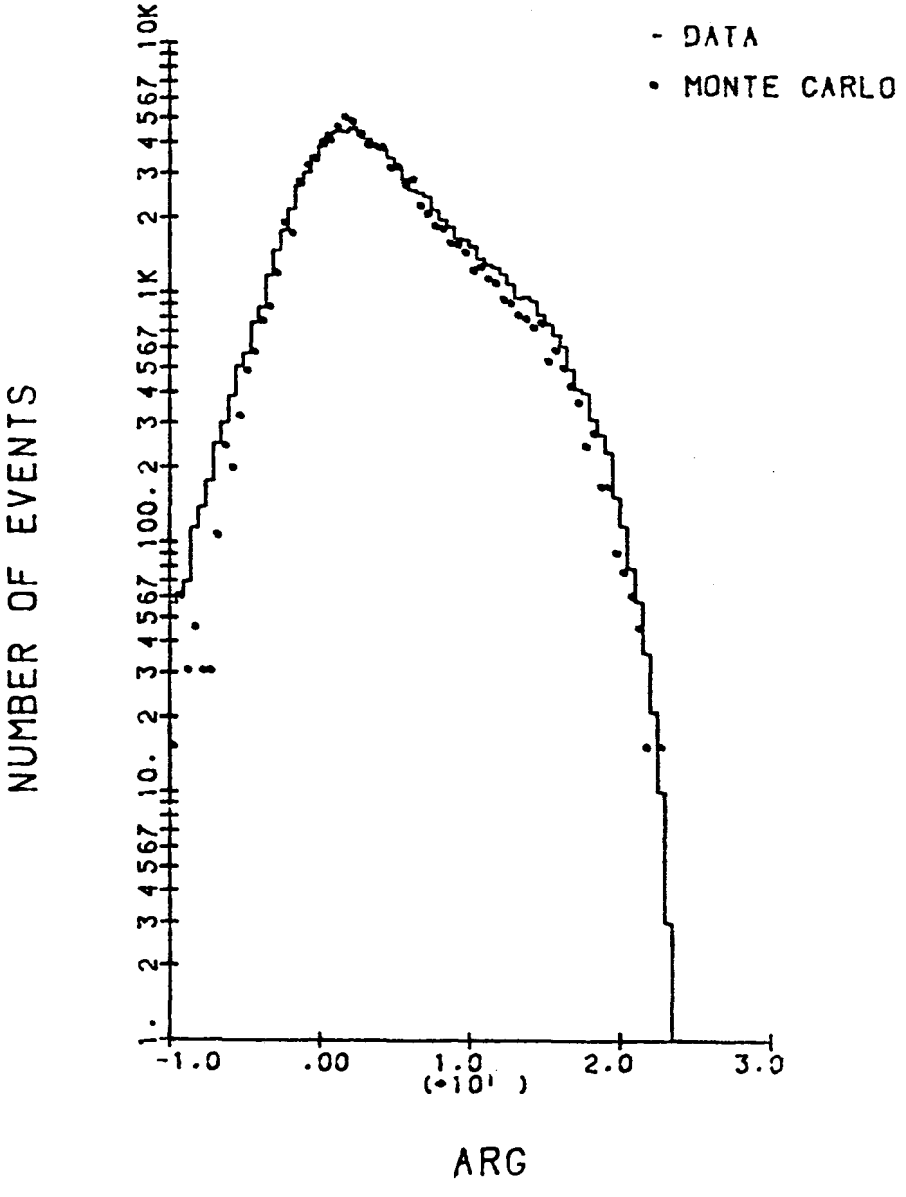


Figure 37. Comparison of data to the Monte Carlo prediction for the ARG distribution for $K_{\mu 3}$ events.

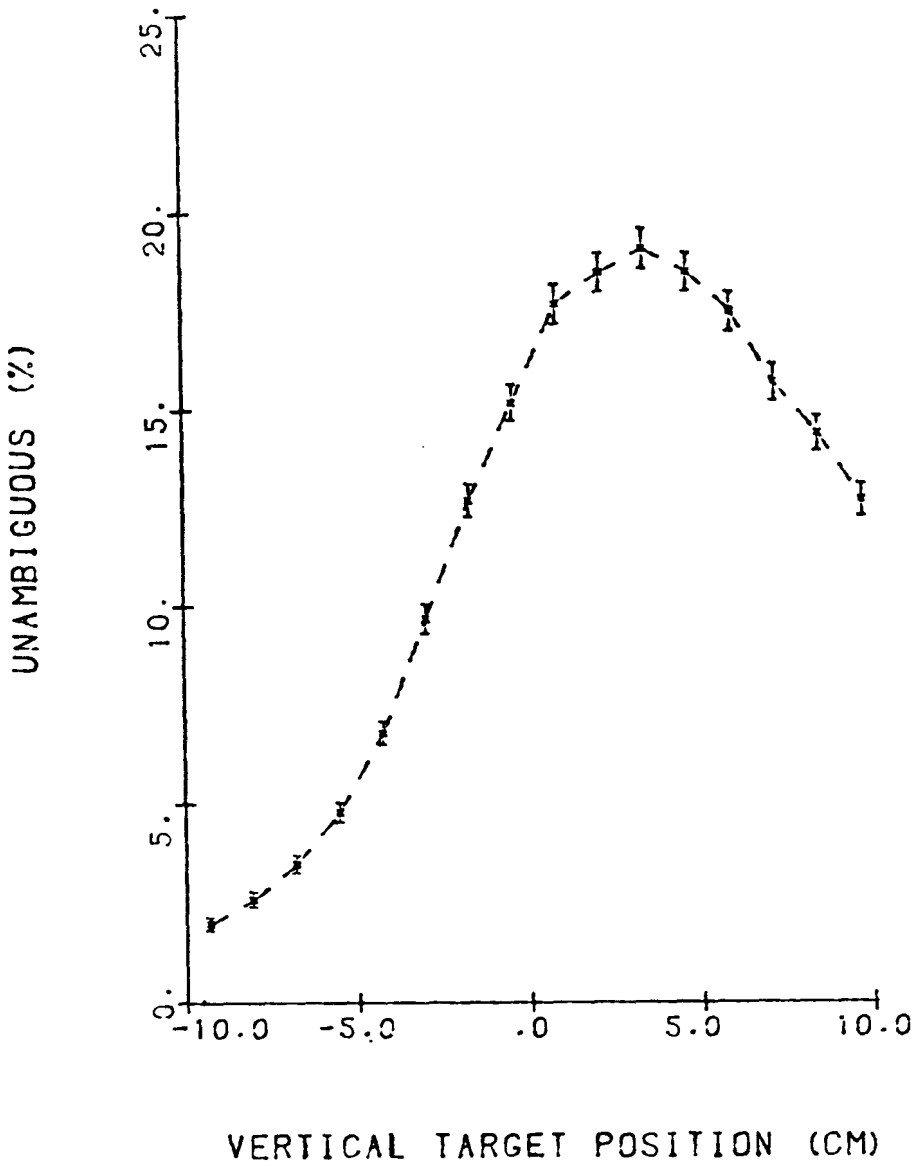


Figure 38. The vertical target sweep for Monte Carlo generated events where ARG was calculated varying the vertical target position from its location used in generating the events. (unambiguous events have $|ARG| < 0.01$)

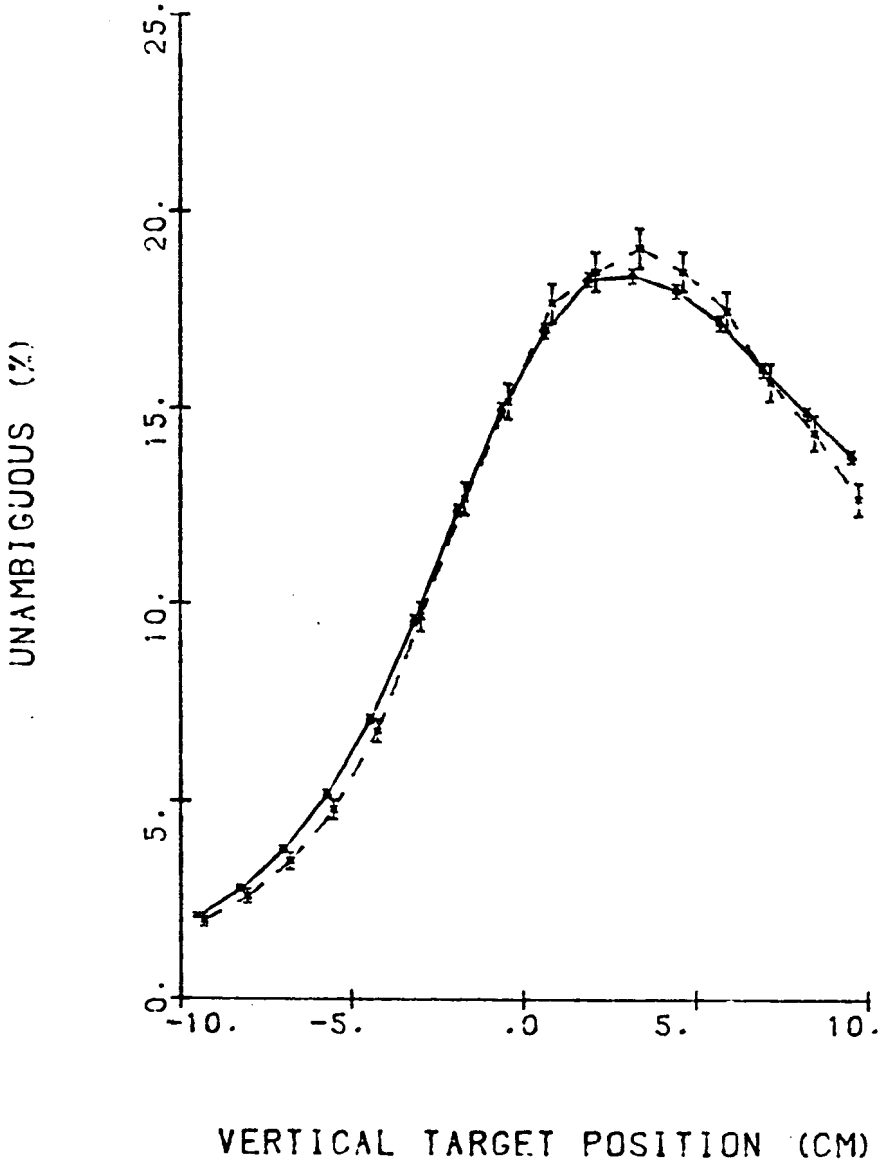


Figure 39. The vertical target sweep for data and Monte Carlo $K_{\mu 3}$ events (solid and dashed lines).

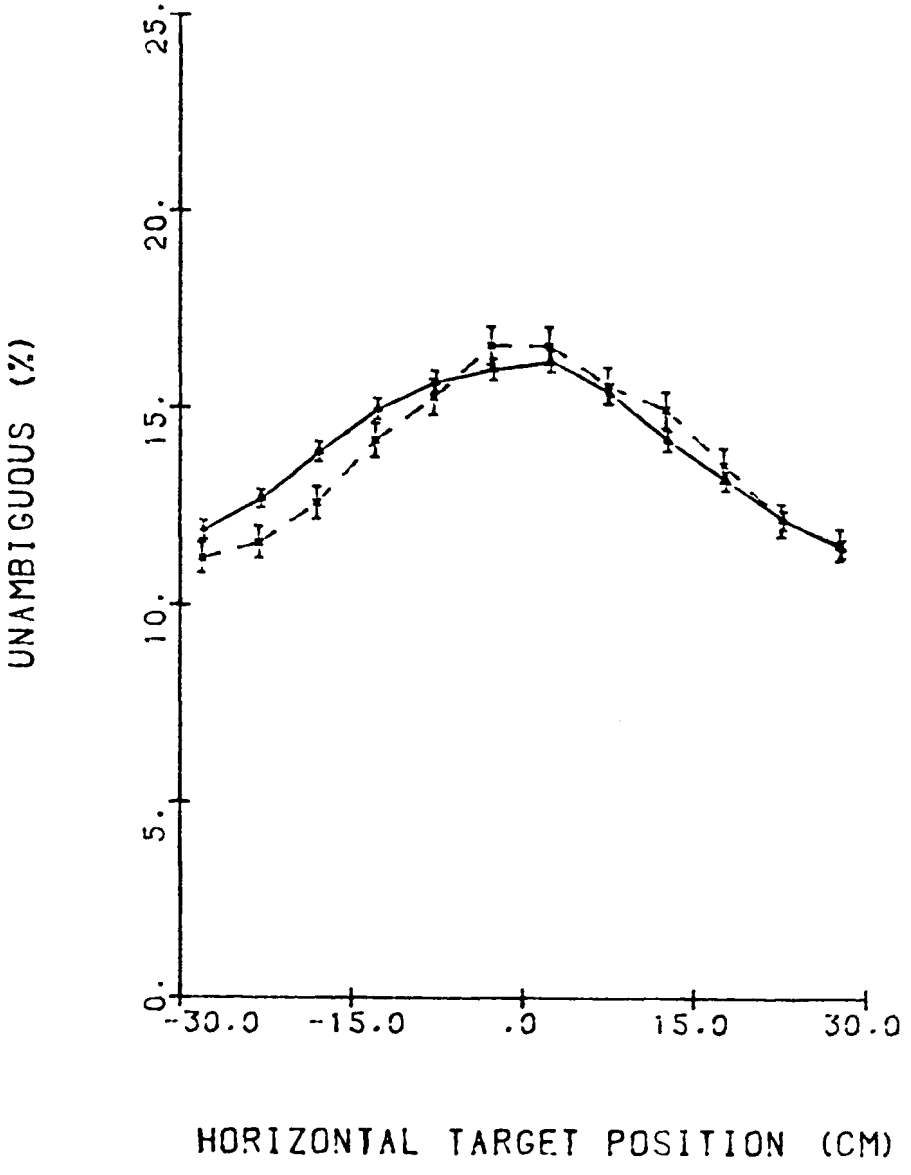


Figure 40. The horizontal target sweep for data and Monte Carlo $K_{\mu 3}$ events (solid and dashed lines).

Another parameter sensitive to a particle's trajectory was the quality of the $K_{\mu 3}$ vertex as measured by SIZE. Figure 41 compares the data to the Monte Carlo for this parameter. This agreement demonstrates that the requirement that the SIZE be less than 0.0015 had the same effect on both the data and Monte Carlo events.

The $K_L^o$ momentum spectrum at the production target used as input to the Monte Carlo was determined from the data for momenta below 60 GeV/c. Figure 42 compares the measured $K_L^o$ momentum spectrum for $K_{\mu 3}$ events with Monte Carlo generated events. It was necessary to increase the number of $K_L^o$'s below 60 GeV/c by 70% over the parametrization of Skubic (Section VI-A) to get this agreement. This agrees qualitatively with previous measurement of the $K_L^o$ momentum spectrum produced at a targeting angle of 7.5 milliradians[32] (the angle in this experiment varied from 0.75 to 1.25 milliradians). Also shown in figure 43 is the data to Monte Carlo comparison of the momentum of converted gamma events. The momentum acceptance of these events differed from $K_{\mu 3}$ events and was similar to that for pi-mu atom events. The agreement of both the $K_{\mu 3}$ and gamma momentum distributions with the Monte Carlo calculation demonstrated that any systematic biases on the measurement of the $K_L^o$ momentum spectrum were small.

Figures 44 and 45 compare the $p_t$ and longitudinal vertex distributions for data and Monte Carlo $K_{\mu 3}$ events. The agreement

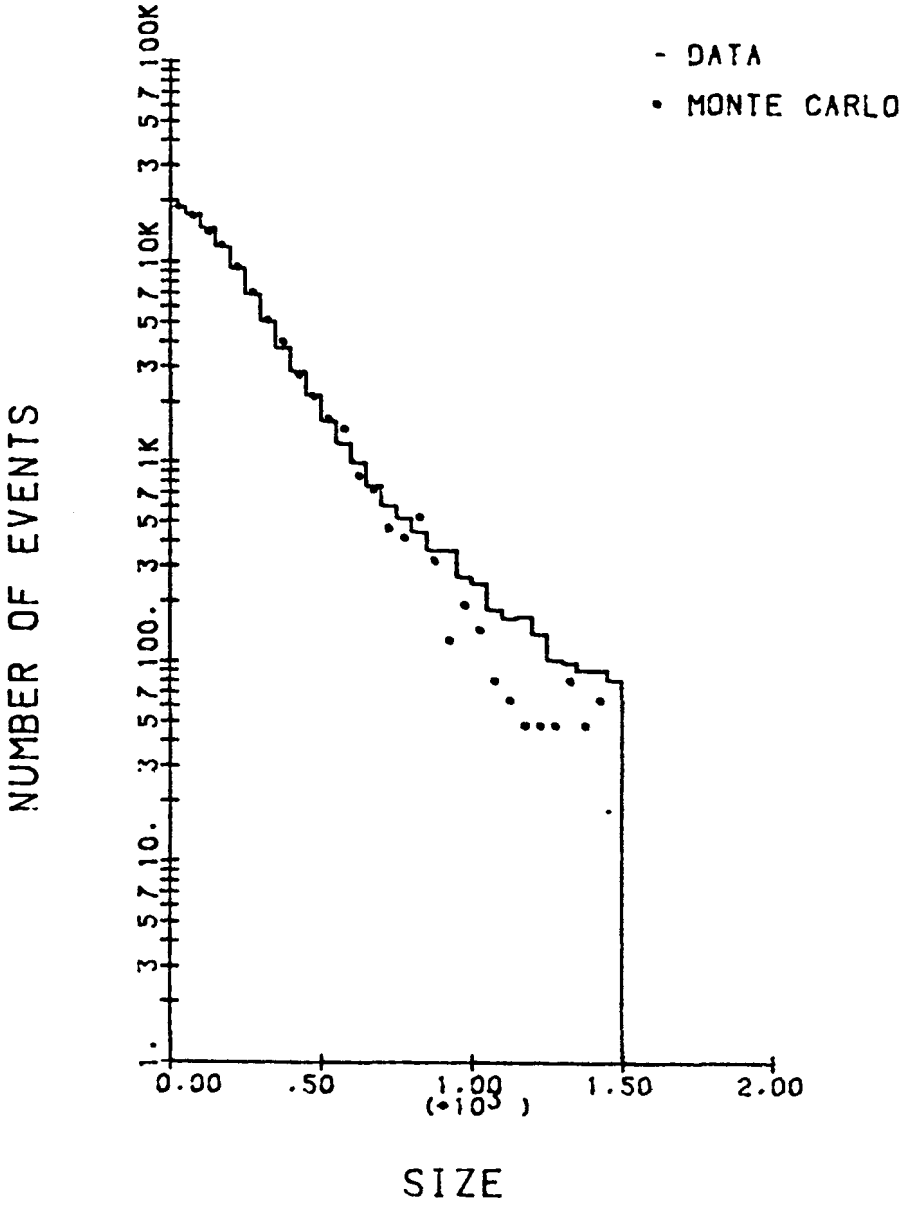


Figure 41. Comparison of data to the Monte Carlo prediction for the SIZE distribution of $K_{\mu 3}$ events.

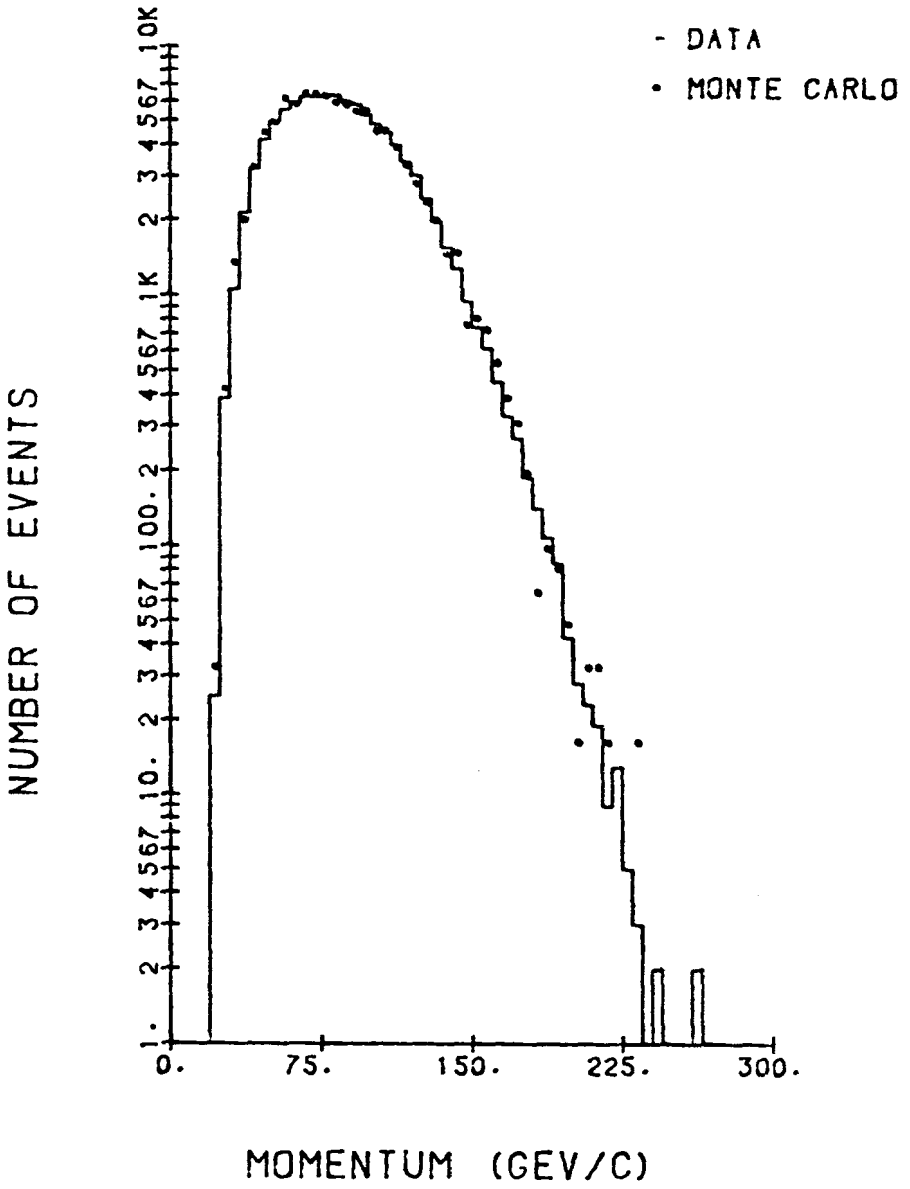


Figure 42. Comparison of data to the Monte Carlo prediction for the $K_L^0$ momentum distribution of $K_{\mu 3}$ events.

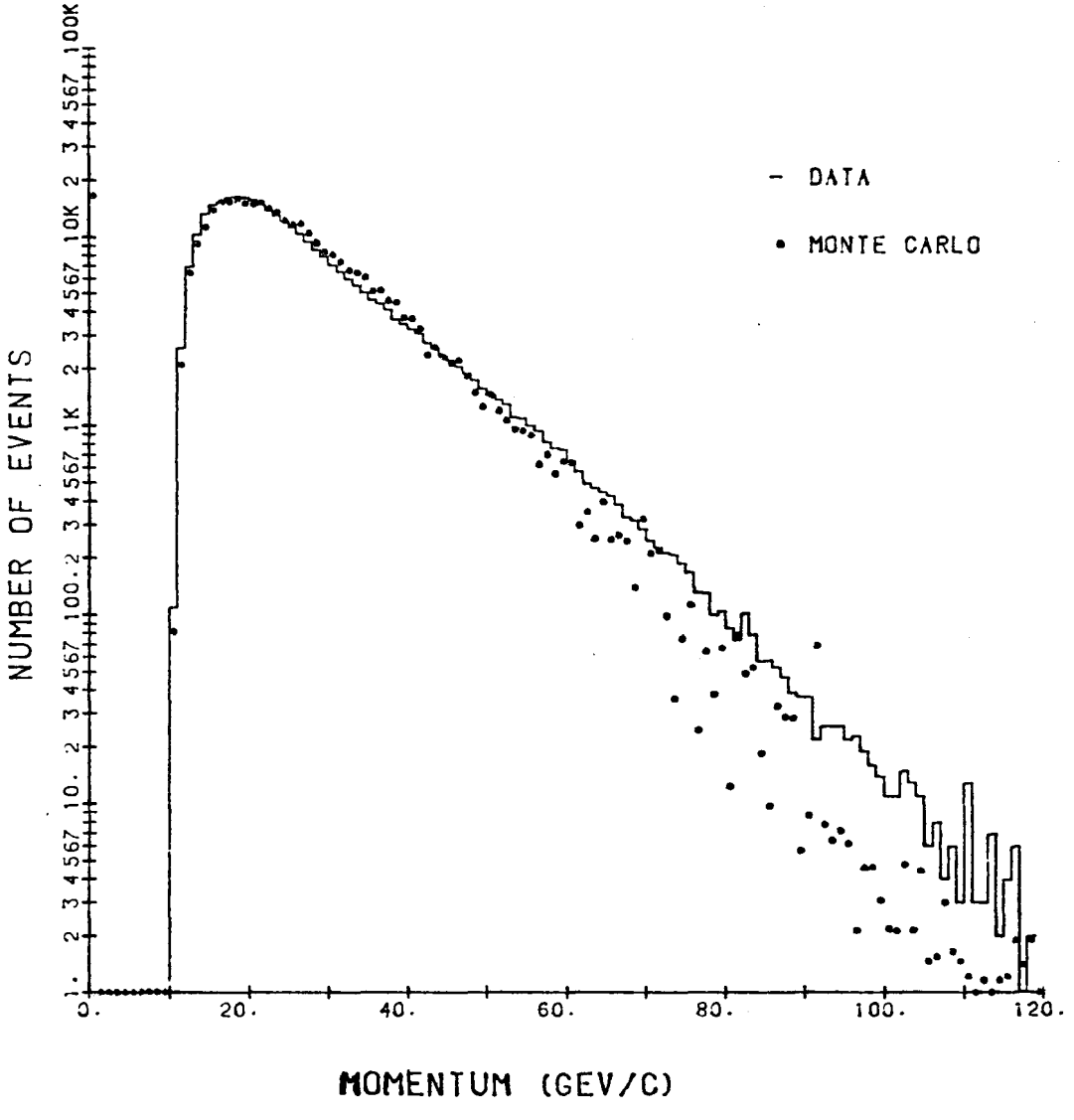


Figure 43. Comparison of data to the Monte Carlo prediction for the momentum distribution of gamma events.

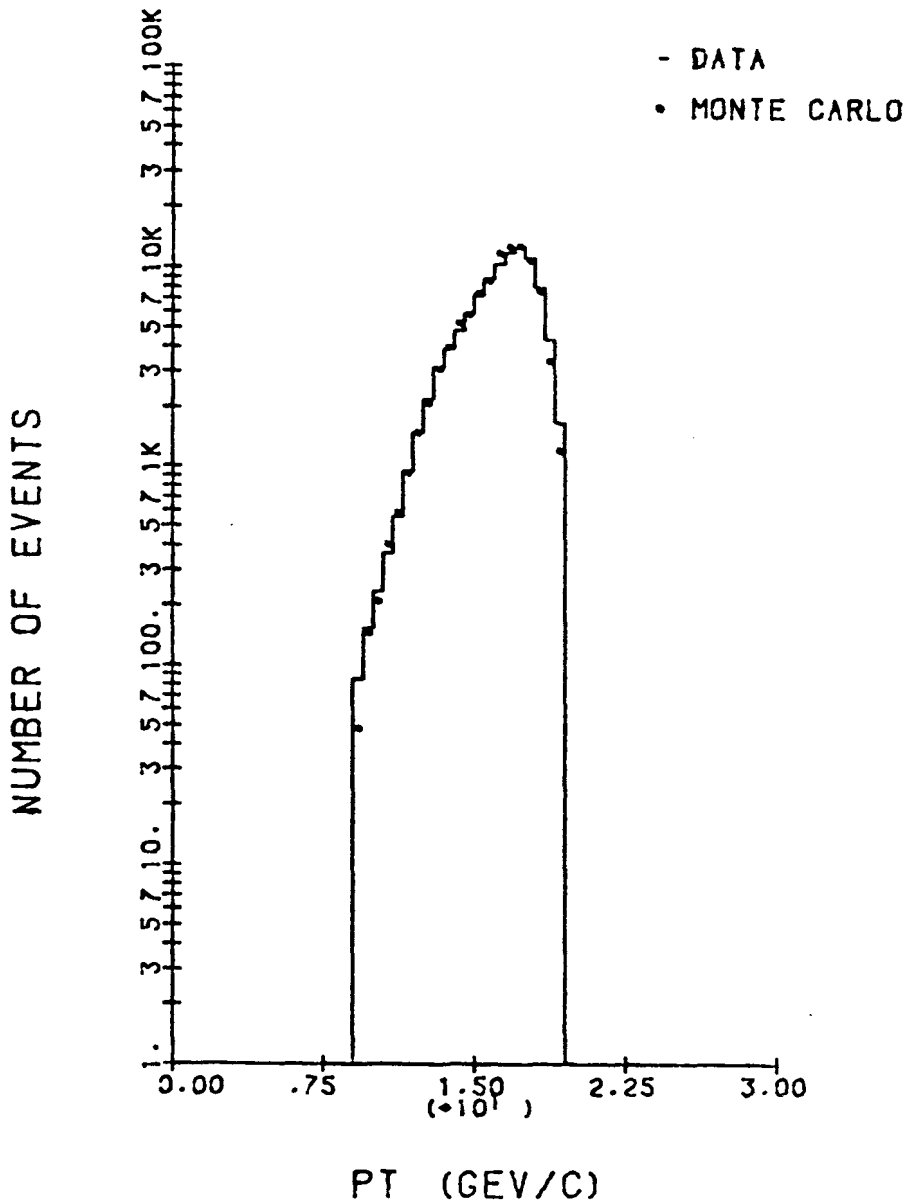


Figure 44. Comparison of data to the Monte Carlo prediction for the $p_t$ distribution of $K_{\mu 3}$ events.

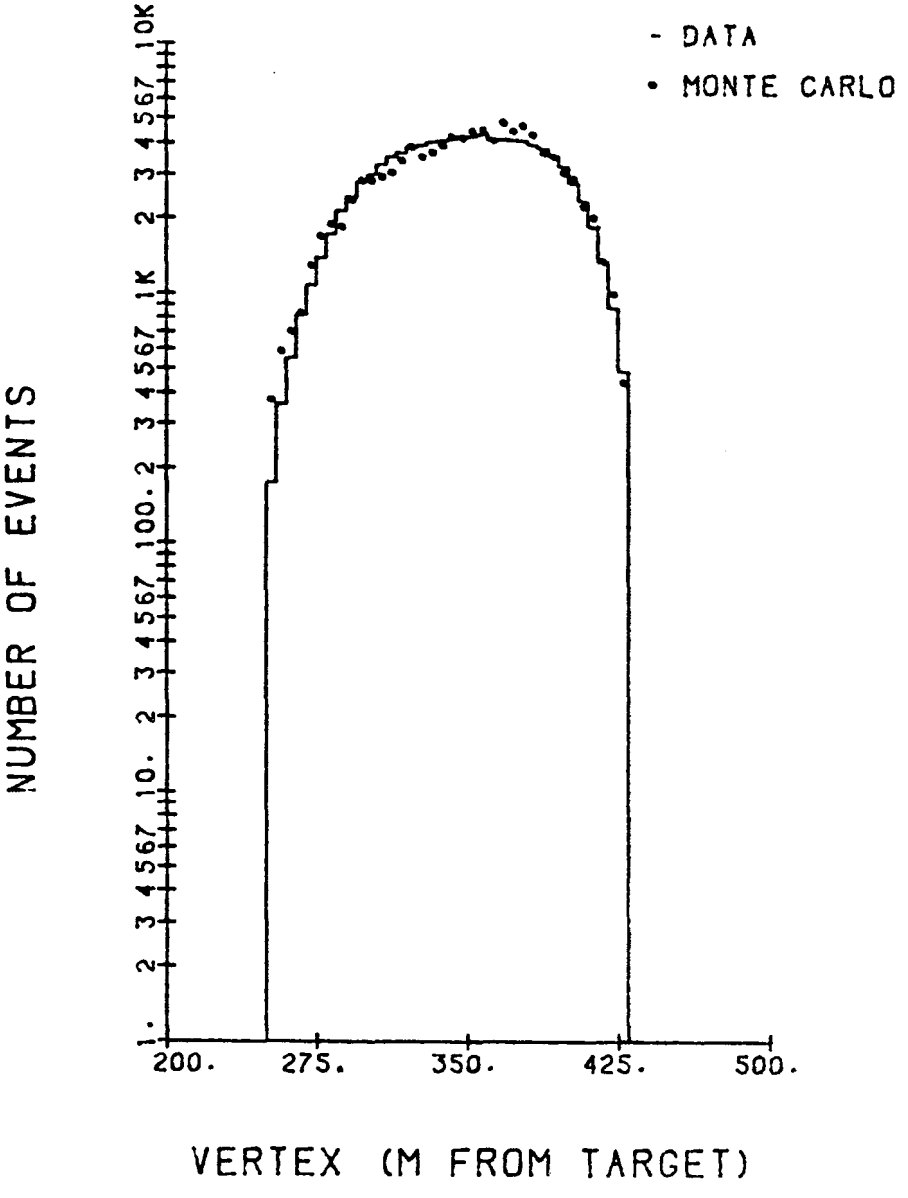


Figure 45. Comparison of data to the Monte Carlo prediction for the longitudinal vertex distribution of $K_{\mu 3}$ events.

is good in both cases. Also shown in figure 46 are the energy of the pion and muon in the $K_L^o$ rest frame for those events in which the difference between the two solutions for both the pion's and muon's energies were less than 10 MeV. The agreement with the Monte Carlo is good though no attempt was made to use these distributions to determine the $K_{\mu 3}$ form factors.

All $K_{\mu 3}$ events were required to have a vertex that originated in the beam. By imposing this, events were lost due to a combination of resolution and uncertainties on the size and location of the beam. In order to estimate the size of any systematic effect of the vertex requirements, the size of the beam in which the vertex had to lie was increased up to a factor of two horizontally and three vertically. The ratio of accepted data and Monte Carlo events was found to vary by less than ± 0.9% over that range. If the effect of $K_{\mu 3}$ background was included, it was estimated that there was a 1.2% systematic error due to the $K_{\mu 3}$ vertex requirements.

## C. Monte Carlo Studies

Uncertainties in the values of various parameters could cause systematic errors on the ratio of pi-mu atom to $K_{\mu 3}$ acceptances. The Monte Carlo was used to determine the size of these systematic errors.

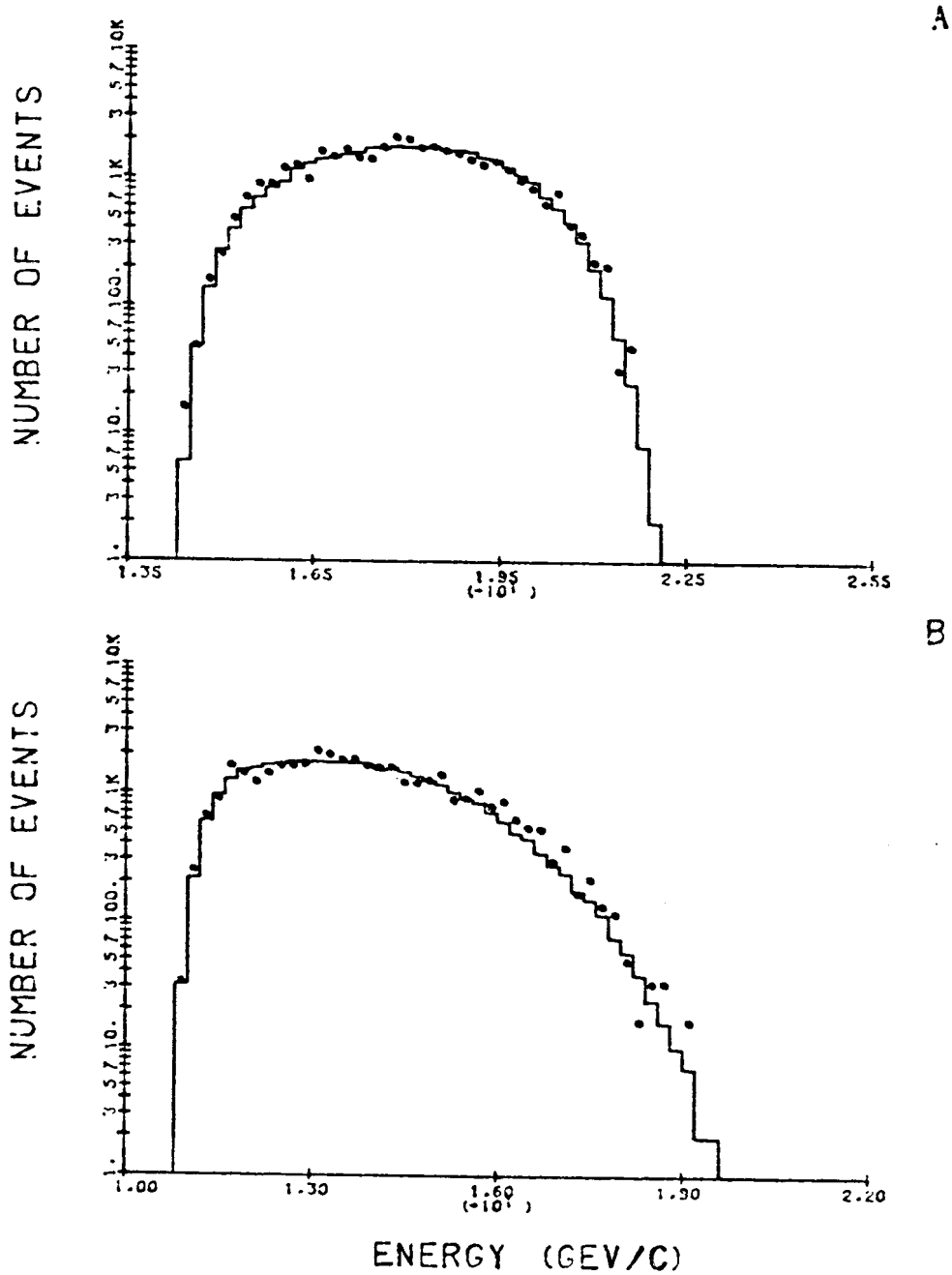


Figure 46. Comparisons of data to the Monte Carlo predictions for the pion (A) and muon (B) energies in the kaon center-of-mass for $K_{\mu 3}$ events.

The $K_L^o$ momentum spectrum used in the Monte Carlo below 60 GeV/c was measured using the data itself. Figure 47 shows the change in the atom to $K_{\mu 3}$ acceptance as the ratio of generated $K_{\mu 3}$'s and atoms with momentum below 60 GeV/c to those above was varied. This figure demonstrated that the acceptance ratio is not very sensitive to the momentum spectrum and, with a conservative estimate of a ± 20% error on the momentum spectrum measurement, gave a systematic error of 1.2%.

The location of the apparatus with respect to the beam was critical in determining the acceptance. Appendix D describes the measurement of the location of the experimental components. The acceptance ratio was calculated with the apparatus' positions varied over their measured errors. The error on the target location gave a 2.1% error while that on the location of the pipe at 321m was a 0.6% error. All other measurement errors contributed less than 0.2%.

The magnetic field strength of MAGA (and from this the absolute strengths of MAGH and MAGV) was determined to 0.4% using $\Lambda^o \rightarrow p\pi$ decays. The acceptance ratio was found to vary by less than 2.1% over that range. The relative strengths between MAGA and the other two magnets was measured to better than 0.3%. This was studied by analyzing Monte Carlo generated events with the strength of MAGA's field 0.3% higher and lower than that at which the events were generated. The acceptance ratio was found to vary

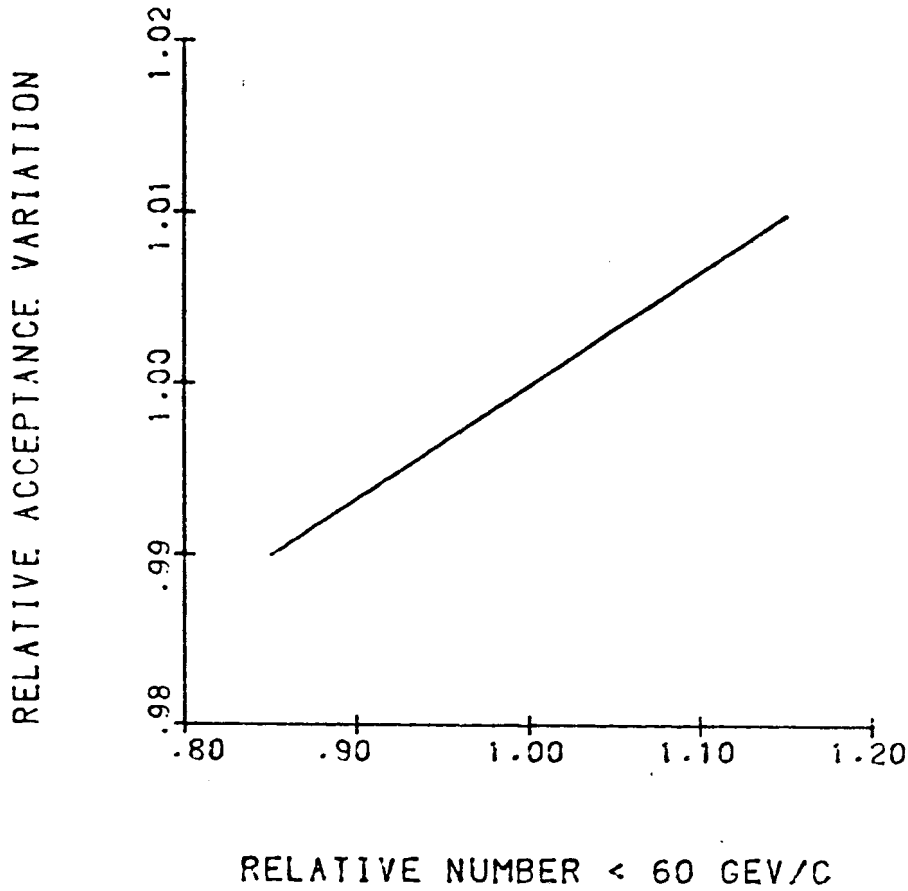


Figure 47. The variation in the relative pi-mu atom to $K_{\mu 3}$ acceptances as a function of the fraction of $K_L^o$'s produced with momentum less than 60 GeV/c.

by less than 1.8% giving an overall systematic error on the relative pi-mu atom to $K_{\mu 3}$ acceptances due to the uncertainty in the magnetic field strengths of ± 2.8%.

The $K_{\mu 3}$ acceptance had a marked dependence on the values of the $K_{\mu 3}$ form factors $\xi$ and $\lambda_+$. Larger values of $\xi$ tended to increase the number of events along the Dalitz plot border where the pion and muon have a small opening angle. Larger values of $\lambda_+$ lowered the average pion energy. Both of these effects caused more decays in the region of highest $K_{\mu 3}$ acceptance. The acceptance varied by ± 3.8% over $\lambda_+ = 0.034 \pm 0.005$ and by ± 3.0% over $\xi(0) = -0.14 \pm 0.11$. Including the correlation between the measured values of $\xi$ and $\lambda_+$, this yielded a a systematic error of 4.0%. The size of this error is comparable to the statistical error on the pi-mu atom sample (8.3%) with both of these being larger than any other errors. Further discussions of $K_{\mu 3}$ form factors can be found in Appendix A.

## X. Trigger Corrections

As described in detail in Section IV-D, the ATOM trigger, used to define pi-mu atom candidates, was a restrictive subclass of the KMU3 trigger requiring one and only one struck counter in the two horizontal counter banks (the W and H banks). In order to measure R, it was necessary to know the number of atom events which failed this trigger due to more than one hit in either of these two banks. This was measured by using $K_{\mu 3}$ events, where the trigger required one or more hits in the W and H bank, to determine the probability of an event having extra counter hits.

More than one H or W hit in a pi-mu atom event was caused either by the pion and muon projections in the side view separating due to multiple scattering or by having additional particles in the event. The multiple scattering caused 4.5% of the pi-mu atoms to fail the trigger requirement. This effect was calculated by the Monte Carlo.

There were two sources of additional particles: delta rays produced by the pion or muon and random particles from either other $K_L^o$ decays or neutron interactions. The delta ray contribution could be measured by using the single muon data sets. The number of H and W hits associated with each muon is given in Table 10. For those events in which that number is two, i.e. one extra, the

Table 10. Single Muon H and W Counter Bank Distributions

| Number counters struck | W bank | H bank |
|---|---|---|
| 1 | 98.91% | 97.36% |
| 2 | 1.07% | 2.55% |
| 3 | 0.02% | 0.09% |

separation between the two struck counters is shown in figure 48. The additional counter is clearly associated with the muon. All of these events were then assumed to be delta rays formed by the muon with the probability for such an extra track being 1.1% and 2.5% in the W and H bank respectively. The probability of an extra track and its pattern did not vary appreciably with momentum. A calculation of the expected size and shape of the delta ray contribution agreed with these measured numbers.[33] The effect of delta rays was then included in the Monte Carlo generation of pi-mu atom and $K_{\mu 3}$ events using these results from single muons.

The probability that an extra counter was struck by a random track was found by comparing the number of hits in the two banks in $K_{\mu 3}$ events to that of Monte Carlo events (which included delta rays) and assuming the excess in the data was due to randoms. There were two classes of events to consider. The first had both particles projecting to the same H or W counter while the other had the tracks project to different counters. This led to, for example, atom events having 10 (out of 11) H counters which could have an extra hit while most $K_{\mu 3}$ events only had 9. So, the probability of an extra counter was measured for both classes and corrected for the number of available counters. These separate results agreed and gave an average random probability of $(5.8 \pm 0.9)\%$. This result was determined by comparing the number of hit counters

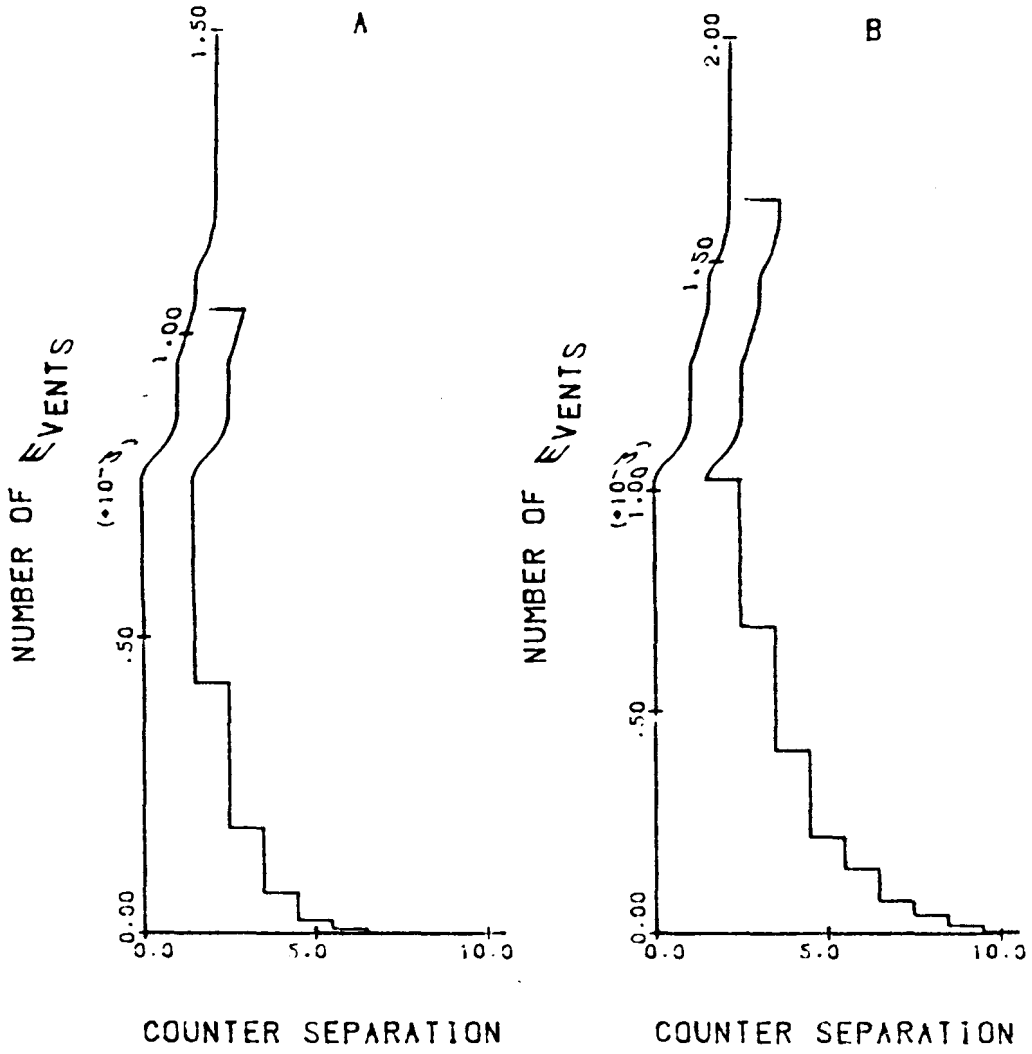


Figure 48. The distributions in the separation between the two struck counters in the W (A) and H (B) counter banks for single muons.

in data events to Monte Carlo events. As the Monte Carlo included the first two causes of extra hits, the error on this number represents the systematic uncertainty on the percent of pi-mu atom events which did not satisfy the trigger due to all causes.

Figure 49 shows the probability of an extra hit versus the single W rate. It is seen to approximate a straight line. This supports the assumption that the extra struck counters are due to delta rays (the intercept of this line) and random tracks dependent upon the rate. Therefore, summing the above three effects, pi-mu atom events which satisfied the trigger represented (82.5 ± 0.9)% of all atom events.

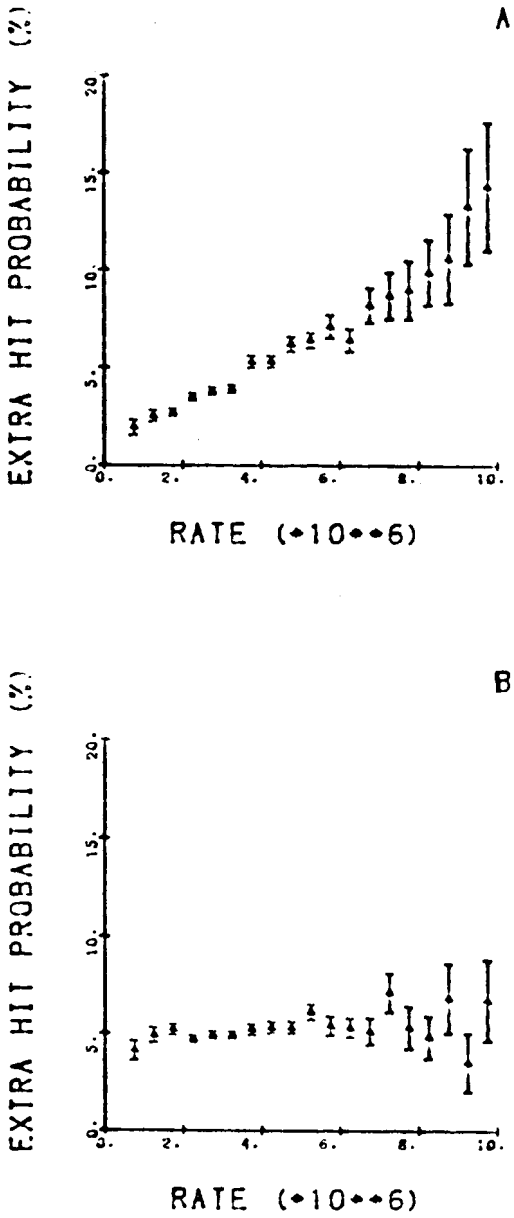


Figure 49. The probability of an extra struck counter in the W (A) and H (B) counter banks as a function of the total counting rate per pulse in the W bank for $K_{\mu 3}$ events whose tracks projected to different counters.

# XI. Results and Conclusions

## A. Determination of the Pi-Mu Atom Rate of Formation

There were 140 pi-mu atoms with 6 background events with $|\alpha - 0.14| < 0.05$ after all requirements were imposed. Of these, 75 were $\pi^+\mu^-$ atoms and 65 were $\pi^-\mu^+$ atoms. The normalizing sample contained 100,885 $K_{\mu 3}$ events with a 5.3% background which were collected prescaled by 32 relative to the atom events. The ratio of the pi-mu atom to $K_{\mu 3}$ acceptance was calculated by a Monte Carlo to be 126 (where errors on this are included in the systematic errors). This calculation included all effects except that of pi-mu atoms lost due to a random extra hit in the W or H counter banks. This was measured to be 5.1%. Combining these, R, the ratio of the rate of formation of pi-mu atoms to that of $K_{\mu 3}$'s, was measured to be

$$R = \frac{(K_L^o \rightarrow (\pi\mu)_{atom}\nu)}{(K_L^o \rightarrow \pi\mu\nu)} = (3.73 \pm 0.40) \times 10^{-7}$$

Table 11 summarizes the errors on this measurement. It is seen that the total systematic error was estimated to be 4.9% compared to a statistical error of 8.6%. Using the $K_{\mu 3}$ branching ratio of $(27.0 \pm 0.5)\%$[34], the rate of formation of pi-mu atoms in $K_L^o$ decay was determined to be $(1.00 \pm 0.11) \times 10^{-7}$.

Table 11. Sources of Errors

| Source | Contribution (%) |
|---|---|
| Systematic errors | |
| 1. Chamber efficiency | 0.6 |
| 2. Track finding algorithm | 2.6 |
| 3. $K_{\mu 3}$ background | 0.8 |
| 4. $K_{\mu 3}$ vertex requirements | 1.2 |
| 5. $K_L^o$ mometum spectrum | 1.2 |
| 6. Apparatus location | 2.2 |
| 7. Magnetic field strengths | 2.8 |
| 8. $K_{\mu 3}$ form factors | 4.0 |
| 9. Trigger corrections | 0.9 |
| Total Systematic Error | 6.3 |
| Total Statistical Error | 8.6 |
| Total Error | 10.7 |

Two different foil thicknesses were used in this experiment; 0.51 mm and 0.89 mm. R was determined for each data set and found to be:

$$R_{0.51} = (4.02 \pm 0.42) \times 10^{-7}$$
$$R_{0.89} = (3.27 \pm 0.47) \times 10^{-7}$$

where the errors are statistical only. These consistent results demonstrate that all atoms were ionized in either foil.

The predicted value for R is $(4.40 \pm 0.16) \times 10^{-7}$. In order to lessen the dependence on the value of $K_{\mu 3}$ form factors, a ratio of the measured and predicted values

$$AR \equiv \frac{R_{experiment}}{R_{theory}}$$

can be formed (see Appendix A). AR is determined to be

$$AR = 0.848 \pm 0.084$$

or 1.8 standard deviations low.

Converted gamma events, which were topologically similar to pi-mu atoms, were used to verify the measurement of R. A separate measurement of the $K_L^o \to \gamma\gamma$ branching ratio (described in Reference 15) yielded

$$\frac{(K_L^o \to \gamma\gamma)}{(K_L^o \to all)} = (4.8 \pm 0.6) \times 10^{-4}$$

in good agreement with the average of previous measurements,

$(4.9 \pm 0.5) \times 10^{-4}$.[35] In addition, the ratio of all gamma events (uncorrected for particle identification) was used to monitor the quality of the data. This ratio was found to vary by less than 4% over 33 subsets of the data. This checked the overall consistency of the data.

## B. Determination of $\xi$

*Assuming the validity of the calculation discussed in Section II*, the measurement of R can also be used to determine the value of the $K_{\mu 3}$ form factor $\xi$ (see Appendix A) *giving*

$$\xi(0) = -0.93 \pm 0.54.$$

Table 12 compares this result and its sensitivity to the value of $\lambda_+$ to the world average and some recent measurements.[36-39] Possible explanations of the discrepency seen in this table are presented in Section D. Detailed discussions concerning these values can be found in references [40-42].

## C. Determination of the Pi-Mu Atom Lifetime

Besides the rate of formation, the only other property of pi-mu atoms determined in this experiment was their lifetime $\tau_A$, expected to be that of the pion $\tau_\pi$. Figure 50 compares the proper time $\tau$ it took for an atom event to travel from the $K_L^o$ decay point to the ionizing foil. As can be inferred from this

Table 12. Determination of $\xi(0)$

| Group | $\xi(0)$ | $d\xi(0)/d\lambda_+$ |
|---|---|---|
| Stanford-Santa Cruz[37] 1974 | -0.11 ± 0.07 | -17. |
| UCLA-SLAC-Johns Hopkins[38] 1975 | -0.25 ± 0.22 | -5.9 |
| LBL[39] 1977 | 0.18 ± 0.11 | 0.68 |
| Particle Data Group [36] 1980 | -0.14 ± 0.11 | -15. |
| this experiment | -0.93 ± 0.54 | 14. |

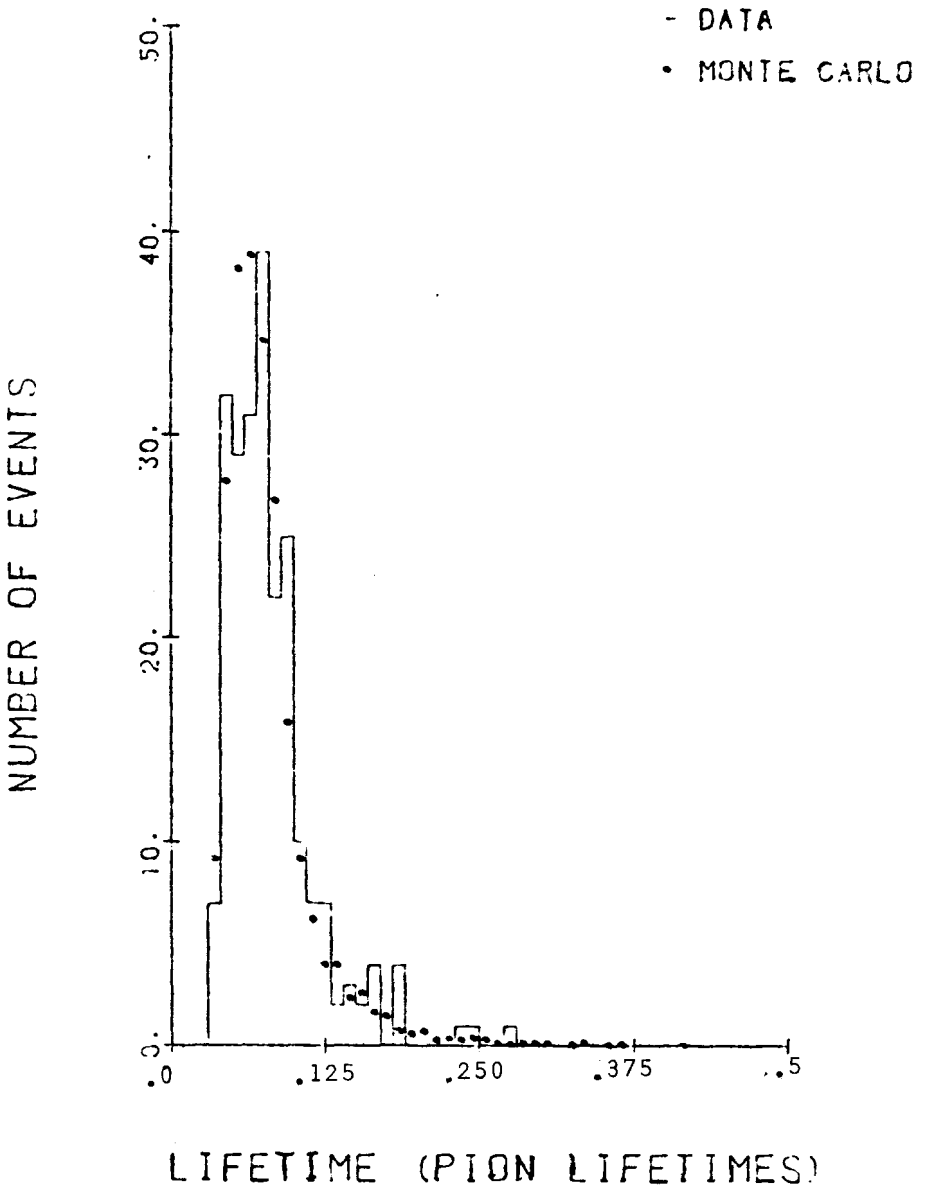


Figure 50. Comparison of data to the Monte Carlo prediction for the proper time distribution of pi-mu atom events.

figure, the sensitivity to this parameter was limited. This was due to a combination of the large atom momentum ($\gamma$ being typically 100) and that low momentum events had short path lengths while higher momentum events tended to have longer path lengths; i.e. that the average $\tau$ was independent of momentum. The average $\tau$ was about 8% of the charged pion's lifetime. Due to this and to the limited statistics of the atom sample, only a lower limit on the lifetime of pi-mu atoms could be determined. There were two ways to determine $\tau_A$. The shape of the proper time distribution was fit (using the sample of events with the relaxed requirements) to that of the Monte Carlo. At $\tau_A = \tau_\pi$ in the Monte Carlo, this fit gave a $\chi^2$ of 13 for 11 degrees of freedom. Varying $\tau_A$ gave a 90% confidence level of $\tau_A > 0.24\tau_\pi$ ($\chi^2 = 17.5$). This technique was not dependent on the value of AR but only on the shape of the proper time distribution. The value of AR could also be used to determine $\tau_A$. The expected number of pi-mu atoms decreased as $\tau_A$ decreased. If any discrepency of AR from 1 was assumed to be due to the atom's lifetime then the measured value of AR = 0.848 $\pm$ 0.084 determined that $\tau_A > 0.21\tau_\pi$ (90% confidence) and that $\tau_A = (0.32^{+0.19}_{-0.10})$ to one standard deviation errors.[43]

## D. Conclusion

This experiment has measured the rate of formation of pi-mu

atoms in $K_L^o$ decay to be $(1.00 \pm 0.11) \times 10^{-7}$. The ratio AR of the measured to the predicted rate was 0.848 ± 0.084. This discrepency could have been caused by one or more of the following (some of which are related):

1. Statistical fluctuation. There is about a 5% chance to be 1.8 standard deviations low.
2. Underestimation of the systematic errors. The techniques used to estimate the errors due to the track finding algorithm and the magnetic field strengths were circuitous
3. Values of the $K_{\mu 3}$ form factors are poorly known; i.e. current measurements are inconsistent (see Appendix A)
4. Only 1S states (which comprise 84% of produced atoms) are being detected due to an unknown mechanism
5. The current theoretical prediction is incorrect
6. The lifetime of pi-mu atoms is less then that of the pion

Other properties of pi-mu atoms such as the lifetime or the energy levels were not measured or were poorly measured independent of AR. Resolving the current discrepency or determining these properties could be the goal of future experiments and experimentalists.

## Appendix A. $K_{\mu 3}$ Form Factors

Both the theoretical prediction and the measured result for the pi-mu atom to $K_{\mu 3}$ rates of formation ratio R depend upon the values of the form factors $\lambda_+$ and $\xi$. Unfortunately, current measurements of these values are not consistent ("the ever troublesome $K \to \pi\mu\nu$"[44]); fitting them gives a $\chi^2$ of 76 for 14 degrees of freedom.[45] Also, the measurements of $\lambda_+$ and $\xi$ are coupled, with the resultant error ellipse having a slope of $d\xi(0)/d\lambda_+ = -15$.[46] This is discussed in references 14 and 41-43. The statistically best measurement (and probably systematically as well) is that of Donaldson et al. who found $\xi(0) = -0.11 \pm 0.07$ and $\lambda_+ = 0.030 \pm 0.003$ with a slope of -17. The effects of these uncertainties on this experiment will now be discussed.

The predicted value for R ($R_{TH}$) increases with larger values of both $\lambda_+$ and $\xi$ (see Section II). Quantitatively, to linear terms in $\lambda_+$ and $\xi$,

$$R_{TH} = 4.40(1.05 + 0.33\xi(0))(0.86 + 4.1\lambda_+) \times 10^{-7}.$$

However, $d\xi(0)/d\lambda_+$ is negative so that when $\lambda_+$ increases $\xi$ decreases and the error on $R_{TH}$ is reduced. Within the $(\lambda_+, \xi)$ one standard deviation error ellipse, $R_{TH} = (4.40 \pm 0.16) \times 10^{-7}$ ($(4.38 \pm 0.12) \times 10^{-7}$ using Donaldson's values).

The $K_{\mu 3}$ acceptance also varies with $\xi$ and $\lambda_+$ with

larger values of both parameters increasing the fraction of decaying $K_L^o$'s in the region of highest acceptance. The effect of this variation on the measured branching ratio ratio $R_{EX}$ can be parameterized as

$$R_{EX} = 3.73\,(1 + 0.2\xi(0))(0.79 + 7.1\lambda_+) \times 10^{-7}.$$

From this, $R_{EX}$ was found to vary by ± 4.0% over the Particle Data Group error ellipse.

As both the predicted and measured values of R have similar $\xi$ and $\lambda_+$ dependences, it is useful to form a ratio of ratio ratios

$$AR \equiv \frac{R_{EX}}{R_{TH}} = \frac{3.73(1 + 0.2\xi(0))(0.79 + 7.1\lambda_+)}{4.40(1.05 + 0.33\xi(0))(0.86 + 4.1\lambda_+)}$$

AR varies by ± 1.5% over both limits on $\xi$ and $\lambda_+$ but by less than 1.6% over the error ellipse. The use of this quantity reduces the dependence on the $K_{\mu 3}$ form factors.

The form factor $\xi$ can be determined by requiring the calculated value of R to equal $R_{EX}$. This gives

$$\xi(0) = \frac{0.8R_{EX} - 4 + \lambda_+(7.1R_{EX} - 19)}{1.25 - 0.16R_{EX} + \lambda_+(6 - 1.4R_{EX})} .$$

Using the measured value of $(3.73 \pm 0.36) \times 10^{-7}$ (where the error does not include any form factor contrbution) $\xi(0)$ is measured to be $\xi(0) = -0.93 \pm 0.54$ using $\lambda_+ = 0.034 \pm 0.005$ with $d\xi(0)/d\lambda_+ = 14$.

## Appendix B. Ionization of Pi-Mu Atoms

In order to identify the components of pi-mu atoms, the atoms were ionized by passing them through an aluminum foil. The amount of material needed to insure this has been calculated elsewhere by a Monte Carlo[47] A rough estimate is given here.

An atom is a bound state with an energy level of 1.6 keV for the 1S state. If a collision, or a series of collisions, raises this energy level to that of the continuum, then the atom is ionized. Detailed Monte Carlo work shows that the most probable mechanism is by a series of collisions in which the atom passes through a sequence of states with increasing principal quantum numbers and then into the continuum. A calculation where the transition is directly from the 1S state provides an upper limit on the amount of material.

In the rest frame of the pi-mu atoms, the Coulomb field at time t generated by a charge center Ze is (figure 51)

$$E_x = \frac{Ze\gamma b}{(b^2 + \gamma^2 v^2 t^2)^{3/2}}$$

$$E_z = \frac{-Ze\gamma tv}{(b^2 + \gamma^2 v^2 t^2)^{3/2}}$$

where b is the impact parameter. In order to ionize the atoms, the energy transferred must be greater than 1.6 keV. This corresponds

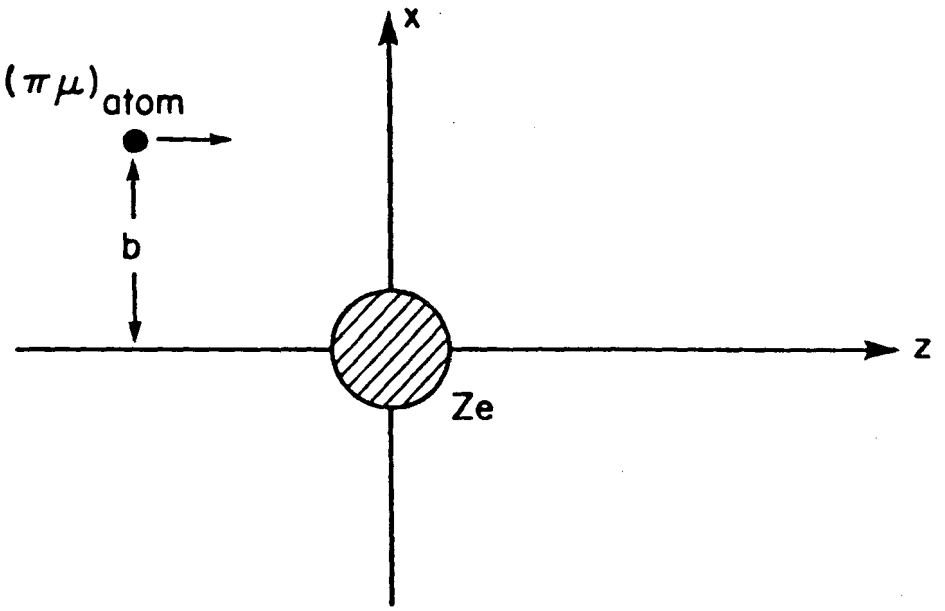


Figure 51. A pi-mu atom passing a nucleus of charge Ze.

to a momentum transferred of about 600 keV/c. This change in momentum is

$$p = \int_{-\infty}^{\infty} eEdt = \frac{2Ze^2}{bc}$$

where the effects of electron screening are ignored. For aluminum, this gives b = 75 fm. So.

$$L = \frac{1}{2\pi nb^2} = 9.1 \times 10^{-2} \text{ cm}$$

The Monte Carlo calculation indicates that all atoms should be ionized by 0.32 mm of aluminum. The actual foil thicknesses used were 0.51 and 0.89 mm with the rate of atom formation measured with each being the same (Section XI).

## Appendix C. Chamber and Counter Efficiency Measurements

It was necessary to measure the efficiency of the 10 MWPC planes in order to calculate the relative retrieval efficiency for foil and beam topology events (see Section VII-A). As the efficiencies depended upon the particle flux, they were found using the entire $K_{\mu 3}$ data sample.

The efficiencies were measured by reconstructing well identified $K_{\mu 3}$ events without using the information in a given plane and then to check to see if there was a wire hit at the correct point in that plane. The results found in this manner agreed with a similar technique using e-pairs.[48] The efficiencies of the 10 MWPC planes are given in Table 3. The 3% error shown represents a conservative estimate on the systematic error on these measurements. Figure 52, which shows the uncertainty of $(EFF_{foil})/(EFF_{beam})$ as a function of this estimated error, demonstrates that precise knowledge of the error was not needed.

The efficiency of each counter in each bank used in the experiment was measured using calibration data taken with the usual trigger requirement in that bank removed. Events where a particle was known to pass through the central half of a given counter were selected and then checked to see if there was a hit in that counter.

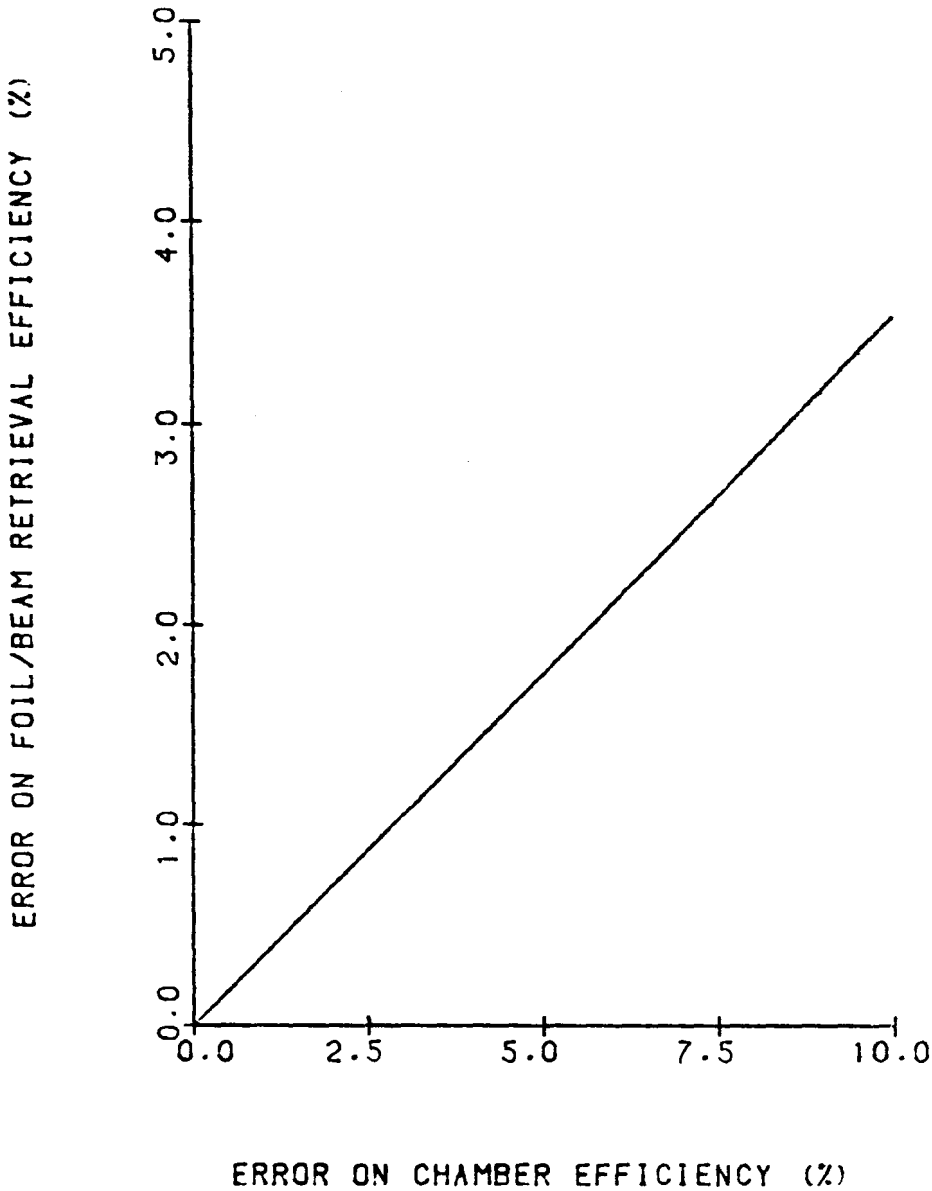


Figure 52. The error on the relative foil to beam retrieval rate as a function of an identical error on the efficiencies of all ten wire plahes.

The results for the MU bank include the losses due to interactions in the steel wall. For the two horizontal banks (W and H) the efficiencies for events which had one particle hit in a counter and those which had two were measured separately. The single-particle and two-particle efficiencies are given in Table 13. In addition, as the trigger for $K_{\mu 3}$ events required one or more hits for these banks, the W and H counter efficiencies were also measured using all $K_{\mu 3}$ events. These results did not vary over the data sample and agreed with those found in the calibration data.

Table 13. Counter Efficiencies

| Bank | A | B | H | MU | W | W | H | H |
|---|---|---|---|---|---|---|---|---|
| Counter | one | one | one | one | one | two | one | two |
| 1 | 99.8% | 90.4% | 99.3% | 77.% | 97.0% | 99.9% | 98.6% | 99.9% |
| 2 | 99.8 | 91.7 | 99.6 | 83. | 98.7 | 99.9 | 97.3 | 98.0 |
| 3 | 99.8 | 95.7 | 99.4 | 87. | 97.4 | 99.9 | 97.8 | 98.0 |
| 4 | 99.3 | 91.1 | 99.8 | 92. | 98.7 | 99.0 | 99.3 | 99.9 |
| 5 | 92.7 | 96.8 | 99.7 | 95. | 94.8 | 99.9 | 91.7 | 91.7 |
| 6 | 95.7 | 82.9 | 99.4 | 94. | 93.2 | 99.9 | 99.6 | 99.9 |
| 7 | 99.7 | 97.5 | 99.8 | 95. | 99.2 | 99.9 | 98.8 | 99.9 |
| 8 | 99.9 | 94.6 | 99.7 | 98. | | | 99.8 | 99.9 |
| 9 | 99.5 | 97.6 | 99.7 | 95. | | | 99.5 | 99.9 |
| 10 | 99.8 | 97.5 | 99.9 | 97. | | | 99.8 | 99.9 |
| 11 | 95.7 | 97.8 | 99.4 | 95. | | | 98.8 | 99.9 |
| 12 | 99.8 | 96.8 | 99.9 | 97. | | | | |
| 13 | 99.6 | 84.4 | 99.4 | 95. | | | | |
| 14 | 99.6 | 97.7 | 99.7 | 97. | | | | |
| 15 | 99.8 | 98.1 | 99.6 | 95. | | | | |
| 16 | 99.5 | 97.6 | 99.7 | 97. | | | | |
| 17 | 99.4 | 98.3 | 99.8 | 93. | | | | |
| 18 | 99.9 | 98.3 | 99.6 | 89. | | | | |
| 19 | 99.8 | 98.2 | 99.8 | 85. | | | | |
| 20 | 99.8 | 66.7 | 99.8 | 91. | | | | |
| 21 | 99.1 | 98.8 | 99.6 | 83. | | | | |
| 22 | 77.1 | 98.8 | 99.7 | | | | | |

## Appendix D. Apparatus Location Measurement

The relative positions of the experimental apparatus and beam were measured as follows. First the chambers were aligned as described below. Then the counter positions were measured relative to the chambers. The location of the chambers in relation to the M3 beam line was then determined. Finally, all other apertures and apparatus were surveyed relative to the beam line.

The chambers were aligned using single muons collected with MAGA turned off at various times during data taking. Large discrete changes occurred twice due to broken wires which necessitated removing a given chamber, replacing the wire and replacing the chamber. Small variations in position occurred throughout data collection due probably to a combination of temperature effects and small stresses in the chamber supports.

The procedure used in lining up the chambers consisted of first using the hits in MWPC 1 and 5 to form a line segment. A deviation was then defined as the separation between a hit in a given chamber and the projection of this line segment to that chamber. The size of these deviations measured the chamber locations. This procedure was used in both the side (X) and top (Y) views. It measured the relative transverse positions of the wire planes to ± 40 microns.

The rotation of a given MWPC relative to the other chambers and the non-orthogonality of the two planes comprising each MWPC were measured by calculating deviations as a function of X and Y position in a given chamber. Measurements of rotations agreed with surveying results. The planes of each chamber were found to be orthogonal to each other to less than 1 milliradian. This correction was added to hits on tracks though no effect upon the resolution of any kinematic quantity was found due to this.

A deviation in a counter was defined by using the fitted information from the chambers and measuring the distance between the projection of a track to a given counter and the center of a hit counter. This measured the center of each counter to ± 0.5 mm.

The position of the beam was measured at three different locations. The ARG distribution technique described in Section IX-B determined the position of the production target to ± 1.5 cm vertically and ± 5 cm horizontally. The data collected with an aluminum target at 400 m (Section VII-C) measured the center of the beam at that point to ± 0.2 mm in both directions. In addition, a Polaroid photograph of the beam was taken directly underneath the W counter bank. This gave the location of the beam center at the W bank to ± 1.5 mm. These three measurements were consistent with each other.

The locations of the beam pipes relative to the beam were measured using Polaroid photographs taken at 321 m and 400 m from

the production target. From these, the distance between the center of the beam and the centers of the pipes was determined to ± 5 mm. The size of the pipe settleling at 280 m (figure 3) was found by surveying the pipe. The magnets, foil and vacuum window locations were surveyed relative to the W counter bank to better than ± 2 mm.

## References


1. Zhang Zhaoxi, He Ju and He Zouxiu, Scientia Sinica 22, 1128 (1979). The production cross section for pi-mu atom formation through hadro-production and subsequent $K_L^0$ decay is $10^{-34}$ $cm^2$ and $10^{-38}$ $cm^2$ through $\mu$-p interactions.

2. L. L. Nemenov, Sov. J. Nucl. Phys. 16, 67 (1973).

3. R. Coombes *et al.*, Phys. Rev. Lett. 37, 249 (1976).

4. R. Staffin, Phys. Rev. D 16, 726 (1977). Staffin uses previous experimental results involving the $\pi\mu$ system to set limits on a possible anomaly in the pi-mu atom formation rate.

5. C. F. Cho, Il Nuovo Cimento 23A, 557 (1974).

6. U. Bar-Gadda and C. F. Cho, Phys. Lett. 46B, 95 (1973).

7. A. Kanmkhodzhaev and R. N. Faustov, Sov. J. Nucl. Phys. 29, 232 (1979).

8. J. D. Bjorken and S. D. Drell, *Relativistic Quantam Mechanics* (McGraw Hill Inc., San Francisco, 1974), p. 113.

9. Nemenov, *op. cit.*

10. Ching Cheng-rui, Ho Tso-hsiu and Chang Chao-hsi, Preprint No. ASITP-80-006 (Fermilab Preprint No. 41,296) (unpublished).

11. H. W. Fearing, E. Fischbach and J. Smith, Phys. Rev. Lett. 24, 189 (1970).

12. Ching *et al.*, *op. cit.*

13. E. S. Ginsberg, Phys. Rev. D 1, 229 (1970).

14. Particle Data Group, Rev. Mod. Phys. 52, S82 (1980).

15. D. Eartly, FNAL, Meson Internal Report (unpublished).

16. R. D. Cousins, Jr., Ph.D. Thesis, Stanford University (unpublished). Also, J. F. Greenhalgh, Ph.D. Thesis, Stanford University (unpublished).

17. These numbers are estimates based on calculations and measurements performed by J. Cronin, D. Hedin and B. Winstein.

18. F. H. Middleton, Physical Science Laboratory, University of Wisconsin, Internal Report (unpublished).

19. M. J. Shochet et al., Phys. Rev. D 19, 1965 (1979). Also, C. Grosso-Pilcher, private communication.

20. R. Piccioni et al., Phys. Rev. D 9, 2939 (1974). Also, J. K. Cobb, private communication.

21. D. I. Porat and D. A. Ouimette, IEEE Trans. Nucl. Sci. 26, 209 (1979).

22. W. R. Molzon, Ph.D. Thesis, University of Chicago, (unpublished).

23. P. Skubic et al., Phys. Rev. D. 18, 3115 (1978).

24. Ginsberg, op. cit.

25. S. W. McDowell, Il Nuovo Cimento 6, 1445 (1957).

26. C. D. Buchanan et al., Phys. Rev. D 11, 457 (1975).

27. J. B. Marion and B. A. Zimmerman, NIM 51, 93 (1967).

28. V. L. Highland, NIM 129, 497 (1975).

29. Particle Data Group, op. cit., p. S45.

30. B. Rossi, High Energy Particles (Prentice-Hall, New York, 1952), p. 71.

31. The variable $p_o'^2$, which is computed assuming a $K_{\pi 3}$ decay, is positive for $K_{\pi 3}$ events and negative for $K_{\mu 3}$ events, in the absence of measurement errors. See A. Astier, et al., Proceedings of the Aix-en-Provence Conference on Elementary Particles (Sacley, France, 1961), p. 227.

32. Molzon, op. cit.

33. R. D. Cousins, Jr., private communication.

34. Particle Data Group, op. cit., p. S18.

35. Particle Data Group, op. cit., p. S18.

36. Particle Data Group, op. cit., p. S82.

37. G. Donaldson et al., Phys. Rev. D 9, 2960 (1974).

38. Buchanan et al., op. cit.

39. A. R. Clark et al., Phys. Rev. D 15, 553 (1977)

40. M. K. Gaillard and L. M. Chounet, Phys. Lett. 32B, 505 (1970).

41. L. M. Chounet, J. M. Gaillard and M. K. Gaillard, Phys. Rep. 4C, 199 (1972).

42. L. G. Pondrom, Proc. Particles and Fields 1976, BNL, Oct. 6-8, 1976.

43. The initial pi-mu atom experiment (reference 3) indicated an atom lifetime one third that of the pion. Mel Schwartz, private communication, 1977. Also, A. L. Hall, Ph.D. Thesis, Stanford University (unpublished).

44. Pondrom, op. cit.

45. Particle Data Group, op. cit., p. S82.

46. Particle Data Group, op. cit., p. S82.

47. Hall, op. cit.

48. J. F. Greenhalgh, private communication.